ABSTRACT

Title of dissertation: Unsteady force production on a flat plate wing by large transverse gusts and plunging maneuvers

Gino M. Perrotta, Doctor of Philosophy, 2017

Dissertation directed by: Professor Anya Jones
Department of Aerospace Engineering

The transient forces produced by large-amplitude transverse gust encounters and plunge maneuvers were studied experimentally in a water-filled towing tank. Forces were measured as a flat plate wing with an aspect ratio of four was towed through a fluid gust and as the same wing performed plunge maneuvers which matched the shape of the gust velocity profile. The transient velocity in each case conformed to the sine-squared profile, and the peak transient velocities were of the same order of magnitude as the steady towing velocities. In most cases, the wing pitch angle was high enough to cause constant flow separation. Even at low wing pitch angles, the increase in flow incidence angle by the transverse gust or plunge velocity was enough to cause flow separation. Transient force magnitudes were shown to increase with increasing stream-normal velocity for both the gust encounters and plunge maneuvers. Transient forces varied with increasing wing pitch angle during gust encounters but not during plunge maneuvers. Force histories in each case were compared to predictions made by existing small-perturbation force models,

and adaptations were made to those models based on physical interpretation of the observed characteristics. Measured forces in both the gust encounters and the plunge maneuvers were found to correspond more closely to predictions made based on attached flow than on separated flow, which supports the suggestion that the presence of a leading edge vortex significantly augments the transient lift. Additionally, a large trailing edge vortex forms at the end of the gust encounter which temporarily reduces the force production below the steady-state values. This was not observed in the plunge maneuver force histories, which were much closer to quasi-steady than were the gust encounter force histories. This analysis contributes to the understanding of unsteady force production in large-amplitude events, and in particular in conditions with separated flow, the behaviors of which are not adequately captured by existing small-perturbation models.

Unsteady force production on a flat plate wing by large transverse gusts and plunging maneuvers

by

Gino M. Perrotta

Dissertation submitted to the Faculty of the Graduate School of the
University of Maryland, College Park in partial fulfillment
of the requirements for the degree of
Doctor of Philosophy
2017

Advisory Committee:
Professor Anya Jones, Chair/Advisor
Professor Ken Kiger, Dean's Representative
Professor James Baeder
Professor Stuart Laurence
Professor Imraan Faruque

© Copyright by
Gino M. Perrotta
2017

Acknowledgments

I am fortunate to have been a part of the Separated and Transient Aerodynamics Laboratory (STAL) under the mentorship of Professor Anya Jones since the lab's early days — before its clever "back-ronym" of a name, before its growth into double-digit membership, before there were even walls around the work space. By a combination of logistical necessities and Anya's generous trust, I was given greater responsibility than my (lack of) seniority warranted, which — along with Anya's patient guidance — fostered both my competence and confidence as a research engineer. Now at the end of my years with STAL, I would like to recognize what a special opportunity this was, and to thank Anya for inviting me to be a part of the team.

Gratitude is also owed to my laboratory peers. In particular, thanks to Dr. Andrew Lind, who with enthusiasm and diligence set such a high standard that all of us at STAL were improved by its pursuit. Thanks to the soon-to-be-Drs. Peter Mancini and Field Manar, who joined the lab at the same time that I did and so with whom I shared the effort and accomplishment of each academic milestone. Their assistance, insight, and friendship were central to my graduate school experience, and are greatly appreciated.

These years have not been all work, and I could not have succeeded here without the neighborly academic community I found myself a part of. Thanks to the Lees, the Myerses, the Schneiders, and the Kordells for their encouragement and inspiration.

Thanks especially to Mom and Dad, who supported me in uncountable ways both during and long before my academic years. Science fair projects and after-school engineering programs were as much a part of my education as was any class, and I am grateful to my parents for seeing the value in those early projects. Thanks also to my siblings, Robert and Michael, to my grandparents, aunts, uncles, and cousins, and more recently also to my in-laws for optimistic reassurance throughout my time in school.

Most of all, thanks to my wife, Abby, whose constant love and stubborn belief in my abilities has sustained my own perseverance. Thanks for always supporting me, for being the test audience for every practice presentation, and for being my greatest fan and best friend.

Table of Contents

List of Tables

List of Figures

Nomenclature

$Æ$	aspect ratio, $\frac{l}{c}$
c	wing chord
$C(k)$	Theodorsen's function
C_D	drag coefficient
C_L	lift coefficient
C_N	normal force coefficient
C_T	tangent force coefficient
$\mathbb{C}_1$	empirical velocity-proportional force coefficient
$\mathbb{C}_2$	empirical acceleration-proportional force coefficient
D	drag
D_{norm}	drag normalized by mean kinetic energy
F_N	normal force
$F_{N,\,\text{norm}}$	normal force normalized by mean kinetic energy
F_T	tangent force
$F_{T,\,\text{norm}}$	tangent force normalized by mean kinetic energy
f	frequency
G	gust velocity ratio, $\frac{V_g}{U_\infty}$
g	acceleration due to gravity
h	plunge maneuver height
k	reduced frequency, $\frac{fc}{2U_\infty}$
L	lift

L_{norm}	lift normalized by mean kinetic energy
l	wing span
q_∞	freestream dynamic pressure, $\frac{1}{2}\rho U_\infty^2 S$
Re	Reynolds number, $\frac{U_\infty c}{\nu}$
$\mathbb{R}$	least-squares residual
S	wing planform area, cl
s	semi-chord lengths, $\frac{2tU_\infty}{c}$
T	duration
t	clock time
t^*	convective time, $\frac{tU_\infty}{c}$
U_∞	freestream velocity
$U_{\max}$	peak total velocity, $\sqrt{U_\infty^2 + V^2}$
V_g	peak gust velocity
V_p	peak plunge velocity
w	plunge maneuver width
$w_g(x)$	gust velocity distribution
z	complex coordinates, $z = x + iy$

Greek symbols

α wing pitch angle above horizontal

Γ circulation

γ vorticity distribution

ζ complex coordinates, $\zeta = \chi + i\eta$

θ gust incidence angle, $\tan\left(\frac{w_g}{U_\infty}\right)^{-1}$

λ gust travel velocity fraction in Miles's function

ν fluid kinematic viscosity

ρ fluid density

σ integration variable to s

ϕ Wagner's function

ψ Kussner's function

List of Abbreviations

AVT Applied Vehicle Technology

CAD Computer-Aided Design

CNC Computer Numerical Control

MAV Micro Air Vehicle

PID Proportional Integral Derivative

PIV Particle Imaging Velocimetry

UDP User Datagram Protocol

Chapter 1: Introduction

Unsteady aerodynamic force production is a topic of interest in many applications. The proper control of an aircraft (and the comfort of its occupants) flying through a gusty environment, in which the local flow velocities vary over time and location, depends on the quantification of the forces produced by the varying flow conditions [1]. The efficiency of rotors in helicopters and wind turbines are significantly affected by the unsteady forces related to dynamic stall [2]. Micro air vehicles (MAVs) are particularly vulnerable to atmospheric gusts due to the relative scaling of steady and transient velocities. Additionally, flapping wing MAVs rely on unsteady aerodynamics for lift, thrust, and control and so require unsteady force quantification in their design [3]. It is these MAV applications in particular which lead the current work to study force production of large-amplitude unsteady events.

The decreasing size of practically-realizable micro air vehicles has increased interest in unsteady force models that do not assume small perturbations [3–6]. The primary difficulty of large-amplitude unsteady phenomena is that they cause flow separation, which greatly increases the complexity of the flow around the wing and leads to unsteady and non-linear forces. The current work investigates the aerodynamic force production of large-perturbation, two-dimensional, unsteady flows;

it is therefore useful to review the particular branch of analytical aerodynamic models that addresses various forms and degrees of flow unsteadiness.

1.1 Steady aerodynamics

The first quantifications of force created by lifting bodies were for various steady flow conditions. The assumption that neither the body nor the flow characteristics were changing in time allowed for the intentional neglect of several complicating features, such as vorticity in the wake of the wing and the inertial reactive force caused by accelerations.

1.1.1 Thin-airfoil theory

The simplest of lifting bodies is the idealized thin, flat, infinite span (for an effectively two-dimensional problem) plate. If the flow is further assumed to be incompressible and inviscid, then the complex effects of flow separation, often called stall, can be removed. By analytically finding the vorticity distribution over the wing that is required to prevent flow passing through the wing, the classical solution of thin-airfoil lift coefficient can be found:

$$C_L \approx 2\pi \sin(\alpha) \tag{1.1}$$

Where α is the wing pitch angle above horizontal. This solution requires that the flow is steady, inviscid, and incompressible, and that the wing is thin, flat, and very nearly aligned with the flow ($\alpha \approx 0$). The first restriction that can be loosened is

the requirement that the wing be flat. The linearizing small-angle approximation which is commonly applied to the wing chord line (through α) can also be applied to the wing camber line to extend this solution to wings that are not exactly (but still very nearly) flat. By again finding the vorticity distribution which enforces no flow through the surface of the wing, it is found that minor camber of a thin airfoil causes a shift in the zero-lift angle of attack but does not change the slope of the lift coefficient with respect to that angle [7].

1.1.2 Joukowsky airfoils

The idealized thin wings of the previous section can be made more physically representative by incorporating structural thickness. Conformal mapping is used to transform the shapes of aerodynamic bodies into shapes more readily formulated by potential flow elements. The Joukowsky (or Zhukovsky) transform is a common mapping between a circle and an airfoil shape. The surface of the airfoil is represented by a path in the coordinates $z = x + iy$, which is transformed to a circle in the corresponding coordinates $\zeta = \chi + i\eta$ by the equation:

$$z = \zeta + \frac{1}{\zeta} \tag{1.2}$$

A circle of radius a in the ζ-plane which is centered on the origin corresponds to a flat plate of chord $4a$ in the z-plane. Moving the circle center off of the origin introduces thickness and camber to the z-plane lifting body. In this way, the relatively simple potential flow solutions for a circle can be used to investigate the aerodynamic

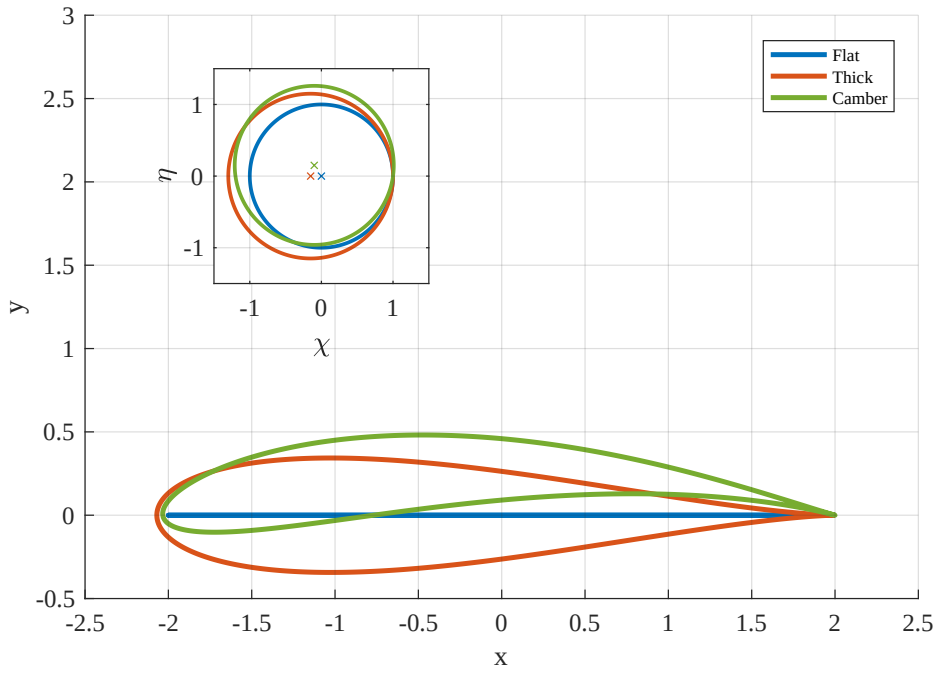

Figure 1.1: Various Joukowsky airfoils and the corresponding ζ-plane circles.

qualities of physically-realizable airfoil shapes.

It is worth emphasizing that the Joukowsky transform can create many z-plane shapes which are not airfoils; aerodynamic application of this equation requires that the ζ-plane circle intersect the point $\zeta = 1$. Several Joukowsky airfoils are demonstrated in figure 1.1.

1.1.3 Empirical extensions

A common compromise in the quantification of aerodynamic force production is the application of empirical data as an adaptation or replacement for an analytical model. Thin-airfoil theory cannot address stalled flow over a wing, but its general form of lift as a dimensionless coefficient multiplied by dynamic pressure can be extended to a semi-empirical model by substituting lift coefficient values from observations.

This system of measurement and careful interpolation allows for the quantification of forces during stall and for bodies of arbitrary shapes. Anderson [7] compares the simplified analytical solution for drag on a cylinder (potential flow predicts no pressure drag in steady flow — d'Alembert's paradox) to the measured results for a range of Reynolds numbers. The proper scaling of these empirical coefficients is perhaps the best method of predicting drag on cylinders.

1.1.4 Quasi-steady analysis

One step towards an unsteady flow solution is quasi-steady analysis. In this method, the flow and body conditions are allowed to change over time, but the force production at any time is calculated using steady-flow formulas based on the characteristics at that particular moment. Any changes in the flow are assumed to immediately develop to the steady-state condition, so no time delay is present in the force production and the events in the flow history are not accounted for.

Quasi-steady analysis introduces the ability to capture inertial force production; the instantaneous flow characteristics can include an acceleration, which accounts for forces not present in steady conditions. For a thin, flat plate [2, 8]:

$$F_{\perp} = -\frac{1}{4}\pi\rho c^2 l\dot{V}_{\perp} \tag{1.3}$$

Where $F_{\perp}$ is the force normal to the wing, $\dot{V}_{\perp}$ is the wing-normal component of the acceleration of the wing, c is the wing chord, and l is the wing span. This inertial force is not due to the mass of the wing — that force is separate and is removed from

aerodynamic force considerations — it is due to the acceleration of local fluid, which increases the apparent inertia of the wing [9]. This is called the "apparent-mass" or "added-mass" force. Only chord-normal acceleration causes this effect — any chord-wise component of acceleration causes no added-mass force, and no added-mass force is oriented chord-wise. For a wing which can accelerate horizontally or vertically (surging and plunging):

$$C_{l,\,\text{inertial}} = \frac{F_\perp}{\frac{1}{2}\rho U_\infty^2 cl}\cos(\alpha) \tag{1.4}$$

$$\dot{V}_\perp = \dot{U}\sin(\alpha) - \dot{V}\cos(\alpha) \tag{1.5}$$

Equation 1.3 can be expanded and normalized by equations 1.4 and 1.5:

$$\therefore \quad C_{l,\,\text{inertial}} = \frac{\pi c}{2U_\infty^2}\Big(\dot{U}\sin(\alpha) - \dot{V}\cos(\alpha)\Big)\cos(\alpha) \tag{1.6}$$

This expresses the inertial contribution to lift, $C_{l,\,\text{inertial}}$, as a linear scaling of the chord-normal projections of the surge and plunge accelerations, $\dot{U}\sin(\alpha) - \dot{V}\cos(\alpha)$. Since the added-mass force is chord-normal, the lift component requires an additional $\cos(\alpha)$ projection.

1.2 Unsteady solutions

In practice, changes in the flow take time to develop into a new steady state. By Kelvin's Circulation Theorem, any change in circulation around the wing must be matched by opposing circulation shed into the wake [7]. The presence of this vorticity in the wake affects the forces on the wing. As the wake departs farther from

the wing, this effect is decreased and eventually becomes negligible. This gradual change in force production in response to instantaneous changes in flow conditions is the core concept for modeling of unsteady aerodynamic force production.

1.2.1 Impulse response

A foundational work on unsteady force production is the analytical solution to small-perturbation impulsive (as in a Heaviside "step" function) lift changes by Wagner [10][1]. Wagner's solution describes the temporary lift deficiency caused by vorticity introduced in the wake of the wing by the change in circulation. The influence of the wake vorticity decreases as the wake is left behind the translating wing, and so the lift asymptotically approaches the steady-state condition. As in steady thin-airfoil theory, Wagner's solution requires the assumption that the wing and wake are very nearly aligned with the flow. It also retains the assumptions of inviscid, incompressible, and two-dimensional flow.

Wagner's function is typically represented by $\phi(s)$, where $s = \frac{2tU_\infty}{c}$ is a normalized time, equivalent to twice the number of chord-lengths traveled by the wing. The function cannot be written in a regular algebraic form, so it is either tabulated or approximated by the following equation [8]:

$$\phi(s) \approx 1 - 0.165e^{-0.0455s} - 0.35e^{-0.3s} \tag{1.7}$$

Wagner's function is plotted in figure 1.2.

[1] Wagner's and Küssner's original papers are in German; their results are described in English in a later aeroelasticity textbook by Blisplinghoff et al. [8].

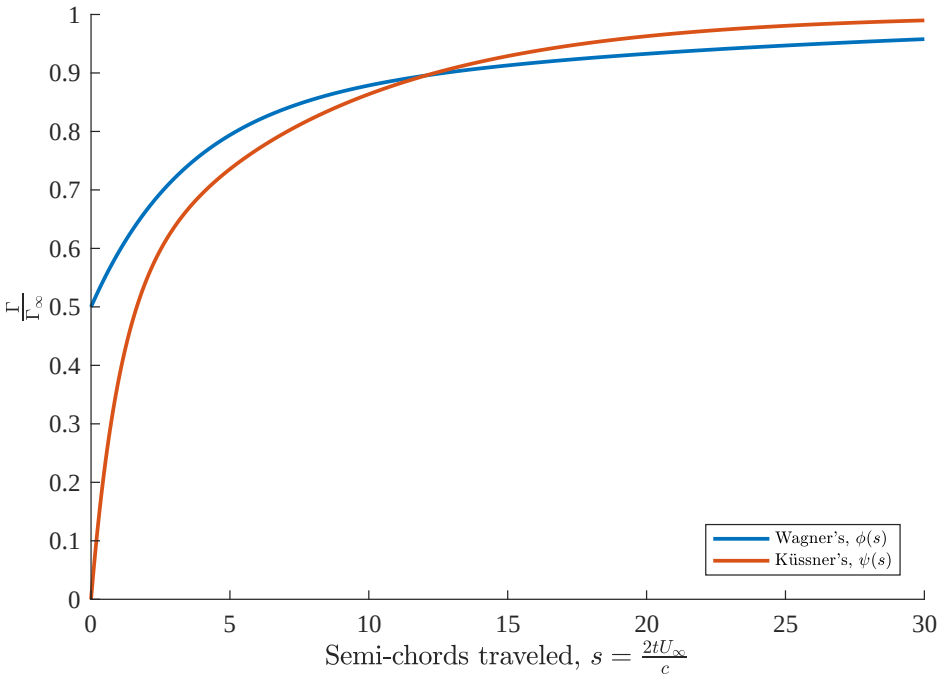

Figure 1.2: Wagner's and Küssner's unsteady lift solutions.

Jones [11] extended Wagner's work by adding tip vortex effects. Jones's solution varies with respect to wing aspect ratio, and suggests that the transient force production is less affected by the tip vortices than is the steady-state lift.

1.2.2 Sharp-edged gust

Küssner [12] produced an analytical solution for the unsteady lift on a wing entering a sharp-edged transverse gust. While Wagner's "gust" reaches the whole wing simultaneously, Küssner's gust progresses from the leading edge to trailing edge of the wing.

As with previous results, Küssner's solution relied on the assumption that the gust velocity was much smaller than the steady forward velocity of the wing so that the effect of the gust was only a small perturbation to the steady conditions. It was

also assumed that the flow is always attached to the suction surface of the wing, which is mainly dependent on the same small perturbation limit. Küssner's function is (as is Wagner's) an equation that describes the temporary deficiency in lift caused by the circulation in the wake of the wing. Küssner's function is typically represented by $\psi(s)$, which can be approximated by [8]:

$$\psi(s) \approx 1 - 0.500e^{-0.130s} - 0.500e^{-s} \tag{1.8}$$

Küssner's function is plotted in figure 1.2.

As an extension of Küssner's solution, Miles [13] solved for the forces caused by a sharp-edged gust that is traveling through the fluid (in addition to the wing moving through the fluid). Miles's function falls somewhere between the solutions of Wagner and Küssner (see figure 1.2), depending on a velocity factor describing the rate of travel of the gust relative to the wing, $\lambda^{-1} = 1 - \frac{U_{\text{gust}}}{U_{\text{wing}}}$. When the gust is stationary, $\lambda = 1$ and the solution converges to Küssner's function. When the gust moves so rapidly that it appears nearly instantaneously, $\lambda \to 0$ and the solution converges instead to Wagner's function.

1.2.3 Harmonically oscillating wings

Theodorsen [14] developed a solution for the unsteady lift produced by a wing which harmonically oscillates. Theodorsen's work allowed for wing plunge and pitch and for the deflection of a trailing edge flap. Theodorsen's solution divides the force production into circulatory and non-circulatory (intertial) and expresses the

unsteady circulatory lift as an amplitude and phase variation of the quasi-steady circulatory lift. The complex "Theodorsen function," $C(k)$, presents the gain and lag of unsteady force production as a function of reduced frequency, $k = \frac{fc}{2U_\infty}$.

As with preceding work, Theodorsen's analysis required that the flow was two-dimensional, inviscid, incompressible, and that the motions of the wing were only small perturbations compared to the mean flow. Garrick [15] extended Theodorsen's work by solving for the thrust generated by the same conditions. Isaacs [16] and Greenberg [17] each extended Theodorsen's work to include oscillating longitudinal velocity.

1.2.4 Arbitrary wing motion

von Kármán and Sears [18] produced an analytical solution for the unsteady lift caused by arbitrary small-perturbation motion of a two-dimensional thin wing in a spatially varying gust. The quantification of force production was approached differently than in previous works; the force production was related to the growth and movement of vorticity rather than directly to surface pressure. This work combined and extended the solutions of Wagner, Küssner, and Theodorsen, and emphasized the physical significance of the resulting equation. The lift production was separated into three physically-distinct terms (for each of these terms, the wing chord is 2 units long and the lift is expressed per unit span):

Quasi-steady lift: The lift corresponding to the enforcement of the Kutta condition. This quasi-steady thin airfoil theory term is unaffected by the vorticity in the wake

of the wing.

$$L_0 = \rho U \Gamma_0 \tag{1.9}$$

where ρ is the fluid density, U is the horizontal velocity of the wing, and Γ_0 is the bound circulation required to achieve tangential velocity at the trailing edge.

Inertial lift: The lift produced as an inertial response to the acceleration of the surrounding fluid. This is called "apparent mass" or "added mass" and is presented as:

$$L_1 = \rho \frac{\mathrm{d}}{\mathrm{d}t} \int_{-1}^{1} \gamma_0(x)\, x \mathrm{d}x \tag{1.10}$$

where x is the spatial coordinate along the chord of the wing and $\gamma(x)$ is the chordwise distribution of vorticity on the wing. As is typical, x is measured in semi-chords away from the mid-chord of the wing.

Unsteady lift: The vorticity in the wake of the wing influences the vorticity distribution on the wing and so alters the lift. This is presented as:

$$L_2 = \rho U \int_{1}^{\infty} \frac{\gamma(\xi)}{\sqrt{\xi^2 - 1}} \mathrm{d}\xi \tag{1.11}$$

where ξ is the spatial coordinate extending horizontally into the wake and $\gamma(\xi)$ is the vorticity distribution in the wake. ξ is also measured as semi-chords behind mid-chord.

This analytical solution is limited to conditions in which the flow around the airfoil is two-dimensional, the vertical wing movement and fluid velocity is small

enough that the wing and wake can be considered to lie on the x-axis everywhere, the flow remains attached to the wing, and the Kutta condition is enforced. In addition to these limitations, the model by von Kármán and Sears requires knowledge of the vorticity distribution over the wing and in the wake, or some quantified relation between wing kinematics and that vorticity. von Kármán and Sears used this to recreate the solutions of Wagner, Küssner, and Theodorsen, for which the vorticity distributions were solvable; such solutions are not available for separated flow phenomena. It is the physical interpretations of lift production that will be useful in the current work rather than the vorticity-impulse equations themselves.

Unsteady force production in cases of separated flow has been addressed more recently by applying potential flow analysis to shear layers shed from both the leading and trailing edges. A blade-element model was developed for insect-like wings in flapping hover by Ansari et al. [4, 19, 20]. A similar model was developed by Eldredge and Darakananda [21, 22] which applies to general wing motion but requires empirical tuning. Each of these models lacks a closed-form solution, and was designed to be implemented by numerical integration.

1.2.5 Indicial theory

Wagner's function and Küssner's function represent indicial responses, which can be used to find the response of the system to arbitrary forcing using Duhamel's integral [23]. This technique approximates arbitrary forcing (wing kinematics or gust velocity distributions) as a series of independent step changes. The resulting lift

from each step gust can be superimposed as long as the system response is a linear function of the forcing; the small perturbation and small angle assumptions used in Wagner's and Küssner's theories have already linearized the aerodynamic response.

When taken to the limit of infinite step changes of infinitesimal magnitude, this approximation becomes the integral of the indicial response and the rate of change of the forcing conditions. Using Küssner's function as an example, the lift coefficient, C_l, caused by a wing translating at constant velocity, U_∞, through an arbitrary gust field, $w_g(x)$, using convective time, s, as above and σ as a bound variable for integrating to s, is [2]:

$$C_l(t) = \frac{2\pi}{U_\infty}\left(w_g(0)\,\psi(s) + \int_0^s \frac{\mathrm{d}w_g(\sigma)}{\mathrm{d}\sigma}\psi(s-\sigma)\,\mathrm{d}\sigma\right) \tag{1.12}$$

Here 2π is the normalized lift curve slope, $\frac{w_g(\sigma)}{U_\infty}$ is the linearized flow incidence angle, and $\psi(s)$ is Küssner's function. The first term captures the initial condition, and the second term integrates the cumulative effects of flow velocity changes for $0 \leq \sigma \leq s$.

1.3 Empirical adaptation

More recently, contributors to AVT-202 [24–27] developed a simplified model for force production by flat plate wings surging from rest at a fixed, high angle of attack. By significantly limiting the allowable wing kinematics, they were able to substitute empirical trends for some of the more complex components of analytical models like that by von Kármán and Sears.

Pitt Ford and Babinsky [28] suggested that flow separation for a thin flat plate at high incidence results in negligible bound circulation. Instead of creating attached flow with vorticity contained in a boundary layer, the sharp edges of the plate cause flow separation which causes the vorticity to collect in leading and trailing edge vortices. In Babinsky et al. [26], the observed influence of leading edge separation on transient lift production led the new model to replace the "bound" circulation (from the Kutta condition in attached flow) with a modeled leading edge vortex. The wake is further simplified into two point vortices of strength Γ instead of wake sheets with vorticity distributions. This eliminates the need to solve integrals when determining the force using the vorticity impulse method. To better represent the observed wake behavior with only two vortices, these vortices convect relative to the background fluid — unlike the stationary wake of von Kármán and Sears. The influence of these vortices on the unsteady lift is:

$$C_{l,\,\text{circ.}} = -\frac{2}{U_\infty^2 c}\left[\left(u_{\text{LEV}} - u_{\text{TEV}}\right)\Gamma + \left(x_{\text{LEV}} - x_{\text{TEV}}\right)\dot{\Gamma}\right] \tag{1.13}$$

The terms inside the brackets are vortex strength, Γ, scaled by the vortices' relative velocity, $(u_{\text{LEV}} - u_{\text{TEV}})$, and vortex growth, $\dot{\Gamma}$, scaled by the vortices' separation distance, $(x_{\text{LEV}} - x_{\text{TEV}})$.

Estimates of the vortex sizes and trajectories, which were needed to calculate lift production, were made based on experiments [25]. The relative vortex velocity

was approximated as half of the free-stream velocity:

$$u_{\text{LEV}} - u_{\text{TEV}} \approx \frac{U_\infty}{2} \tag{1.14}$$

This approximation only holds in the immediate transient for a surging wing; the relative vortex velocity will approach zero as each vortex becomes stationary relative to the background flow. The horizontal separation of the vortices was approximated as the horizontal projection of the wing chord:

$$x_{\text{LEV}} - x_{\text{TEV}} \approx c\cos(\alpha) \tag{1.15}$$

This separation is constant, which conflicts with the inclusion of non-zero relative vortex velocity but does not significantly affect the results [26]. The vortex circulation is then approximated by a scaled modification of Wagner's function, $\phi(s)$. Typically, a varying velocity profile would be incorporated using indicial theory (see section 1.2.5). This was rejected in favor of a simpler approximation; the gradual nature of the surging acceleration is reconciled with the impulsive start of Wagner's function by scaling the result by the ratio of instantaneous to final velocity:

$$\Gamma \approx \Gamma_\infty \frac{U(t)}{U_\infty} \phi(t) \tag{1.16}$$

The steady-state value of circulation was approximated using linearized thin-airfoil

theory:

$$\rho U_\infty \Gamma_\infty \approx (2\pi\alpha)\ \frac{1}{2}\rho U_\infty^2 c \tag{1.17}$$

$$\therefore \quad \Gamma_\infty \approx \pi\alpha c U_\infty \tag{1.18}$$

The non-circulatory added-mass lift was approximated using potential flow for an accelerating flat plate, equation 1.6. All of these approximations together form a simplified quasi-steady model for lift produced by a surging-from-rest flat plate:

$$C_l = \frac{-2\pi\alpha U(t)}{U_\infty^2}\left[\frac{U_\infty}{2}\phi(t) + c\cos(\alpha)\,\dot{\phi}(t)\right] + \frac{\pi c}{2U_\infty^2}\dot{U}\sin(\alpha)\cos(\alpha) \tag{1.19}$$

The left half of equation 1.19 represents the circulatory force production by vorticity in the wake of the wing. The right half of the equation represents the non-circulatory force production by the acceleration of the wing. The simplifications made in the derivation of this model have made it easy to implement, but have restricted its applicability to surging-from-rest flat plates at high wing pitch angles.

1.4 Experiments

Unsteady aerodynamic force production from translational acceleration (surge and pitch) has also been investigated experimentally. Force measurements in cases with flow separation are particularly interesting, as those results have allowed the direct comparison to results of predictive models. Measurements (and qualitative visualizations) of the associated flow velocities have allowed the testing of the validity of each model's assumptions, such as verifying attached or separated flow. Existing

literature has measured forces and tested models for a range of conditions, including harmonic oscillations in surge, plunge, and pitch, and surge-from-rest maneuvers. The current work adds to this by investigating non-oscillating transverse events for both moving-fluid and moving-wing cases.

1.4.1 Streamwise perturbations

Dickinson and Götz [29] measured unsteady force production for rapid surge-from-rest maneuvers. Inertial force production was intentionally neglected, but it was concluded that even post-acceleration the transient lift and drag were higher than steady-state. Both the transient and steady-state forces were predominantly chord-normal. Mancini et al. [30] further studied the force production and vortex characteristics for a surging flat plate during a variety of start-from-rest maneuvers. The unsteady force production was compared to the sum of two terms, added-mass inertial forces and a quasi-steady simplification of Wagner's function. It was concluded that the leading edge vortex caused the observed transient lift to exceed the prediction made by the two quasi-steady terms. It was also noted for high-incidence cases that the recovery time was greater than expected; the unsteady forces did not return to steady-state values within the measured duration of 14 chord-lengths traveled. Stevens et al. [25] continued to study surging flat plates. Results were compared from different facilities (and computational methods) to confirm the presence and influence of shed vortices at high incidence. The vortex dynamics observed in this work allowed for the simplifications in the semi-empirical

model by Babinsky et al. [26].

Much of the experimental literature on gust encounters focuses on longitudinal gusts, which can be created by varying wind tunnel speed [31–33]. The alignment of the steady and transient velocities in the longitudinal cases makes them quasi-one-dimensional, and so they are experimentally and analytically simpler than the transverse cases. Granlund et al. [33] presented a comparison of oscillating longitudinal gust experiments using two facilities. One facility was fitted with rotating vanes in the tunnel to create an oscillating free stream velocity around a stationary model. The other facility oscillated the model within a steady free stream flow. It was concluded in that work that the analytical estimation of added-mass forces was accurate and that subtracting the inertial forces in the moving model case allowed for the direct comparison of moving-model and moving-fluid results.

1.4.2 Transverse perturbations

More literature exists for transverse unsteadiness caused by plunge maneuvers rather than fluid gusts. This is particularly common in the context of flapping-wing MAVs, and so most of the work on this subject has focused on frequency-based models for wings which harmonically oscillate in plunge (and often also in pitch). Unsteady force measurements were shown to exceed quasi-steady predictions [34, 35]. The measured forces matched predictions by Theodorsen's model (at least as closely as did predictions by quasi-steady or computational models) despite flow separation [36–38]. Flow visualizations and flow velocity measurements indicated that the

unsteady force was strongly affected by the wing-vortex interactions [39–41].

Non-harmonic plunge maneuvers are not covered so thoroughly. Kriegseis et al. [42] studied both surging and plunging maneuvers in an investigation of the influence of flow history. The transient velocities in each case were ramp-up maneuvers, which are commonly studied for surge but not for plunge. Each maneuver was designed to reach the same steady-state condition from different initial conditions, and it was concluded that the pre-maneuver presence of a developed boundary layer in the plunge case had little effect on the unsteady force production.

Transverse gusts are more difficult to experimentally recreate than longitudinal gusts, and are less commonly addressed in the literature. Kuethe [43, 44] created a gust encounter by moving a wing over a vertically-oriented open-section wind tunnel. The test article was mounted at the end of a whirling arm as it would have been for steady aerodynamics tests. At one location around the circular path of the wing, the wing passed over a gust generator which allowed for the measurement of transient forces. The lift produced during the gust encounter was found to be in agreement with predictions made by the theory of von Kármán and Sears [18]. Holmes [45] created an extraordinary wind tunnel with cam-actuated, sinusoidally-waving walls. The phasing of the cams determined the shape of the wind tunnel interior which could be configured to create an oscillating longitudinal or transverse gust at the wing. It was concluded that analytical models were valid for low-amplitude gusts, but that flow separation at higher amplitudes caused significant disagreement between predictions and observations. The highest ratio of the gust velocity to the steady velocity, the "gust ratio," among these tests was $G = 0.24$.

Wong et al. [46] compared experimental moving model results and computational moving fluid results for harmonic transverse gusts to investigate their possible equivalence. Unlike the longitudinal case by Granlund et al. [33], Wong et al. concluded that inertial effects were not the only difference between the two arrangements. This was highlighted by observing that the forces in each case were different even at the moment that each transverse acceleration was zero.

1.5 Present work

Preceding work has incrementally advanced the understanding of unsteady aerodynamic force production in various related aspects, but none have yet thoroughly addressed the force production by non-harmonic transverse unsteady events which are too large to be simplified by small-perturbation assumptions. This document describes an experimental investigation of transverse gusts and plunging maneuvers which works towards a closed-form analytical model of force production with flow separation. This is similar to the approach of Babinsky et al. [26]; the physical understanding granted by the analytical solution of von Kármán and Sears will be adapted based on empirical findings so that the resulting model better represents the high-amplitude unsteadiness of fluid gusts and plunging wing maneuvers for limited kinematics. Some time will also be taken to expand on the moving-model to moving-fluid comparisons of Granlund et al. [33] and Wong et al. [46].

Chapter 2 describes the experimental facility and methods which enabled this work. The test apparatus, tools for data collection, and methods of data processing

are presented to aid in understanding the following results. Chapter 3 presents and discusses the unsteady force production for transverse gust encounters. Chapter 4 presents the measured forces from various plunging wing maneuvers designed to be geometrically similar to the gust encounters. It also directly compares the force production of the moving-model and moving-fluid cases. Finally, chapter 5 summarizes the present work and its significant conclusions, and presents several suggestions for future work.

Chapter 2: Methods

The current work is primarily experimental; its foundation is the measurement of forces and fluid velocities resulting from deliberately controlled gust encounters and plunging maneuvers of a flat plate wing. This chapter discusses the towing tank facility in which these experiments took place, the gust generator added to that tank for these experiments, the flat plate wing used as the test article, the techniques used for collecting the data, the parameters defining the tested conditions, and some general treatment of the collected data.

2.1 Towing tank

Experiments were conducted in the University of Maryland's water-filled towing tank, shown in figure 2.1. The tank is 7 m long, 1.5 m wide, and the water in it is 1 m deep. Using water as the working fluid instead of air allowed for higher forces at the achievable towing speeds and greatly improved the ability to conduct particle imaging velocimetry (PIV) on highly unsteady and separated flows.

The tank had a steel frame holding glass walls and a glass floor which allowed optical access for PIV. The frame also carried a four degree-of-freedom motion control system for maneuvering the test article. The motors were controlled by PID feedback

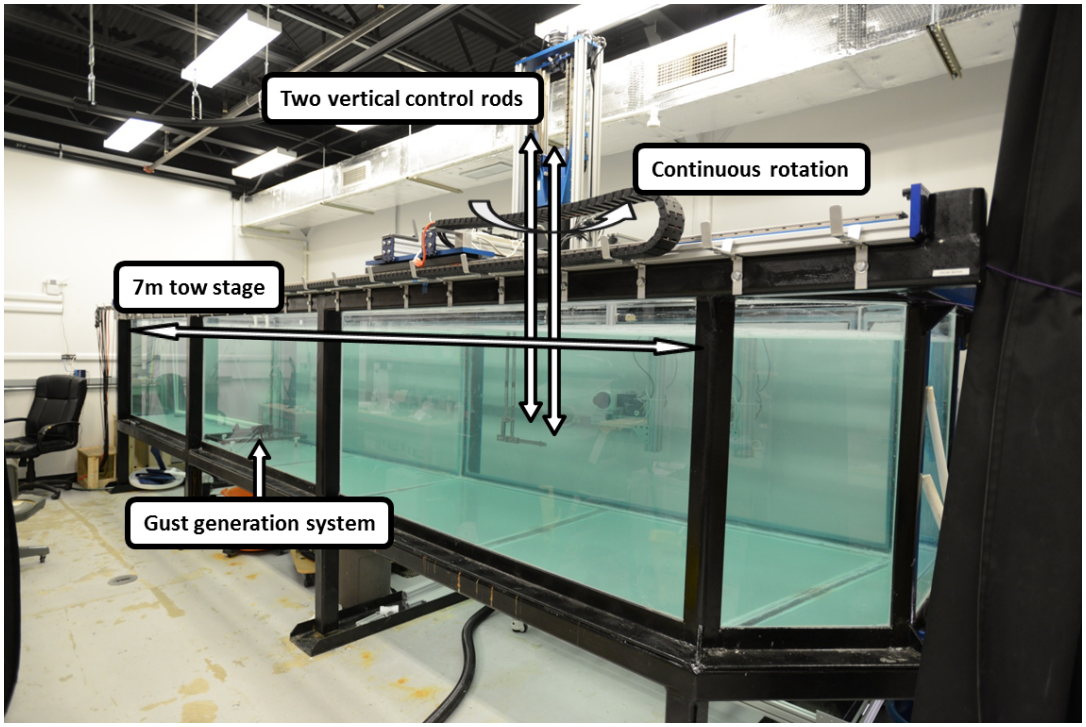

Figure 2.1: The experimental facility, a water tow tank with four degree-of-freedom motion control.

based on encoder position readings. Three degrees of freedom were used in the current experiments: streamwise towing and two parallel vertical control rods. The parallel inputs were converted by a slide-crank mechanism to stream-normal motion and angle of attack.

2.2 Test article

The test article was the simplest form of lifting surface, a flat plate wing. In these experiments the flat plate had a 5 cm chord, 20 cm span, and 1.6 mm thickness. This makes the aspect ratio 4 and the thickness-to-chord-ratio 3%. This wing was designed to match that of previous experiments by AVT-149 [6].

Two wings of this design were created using different materials. The first of

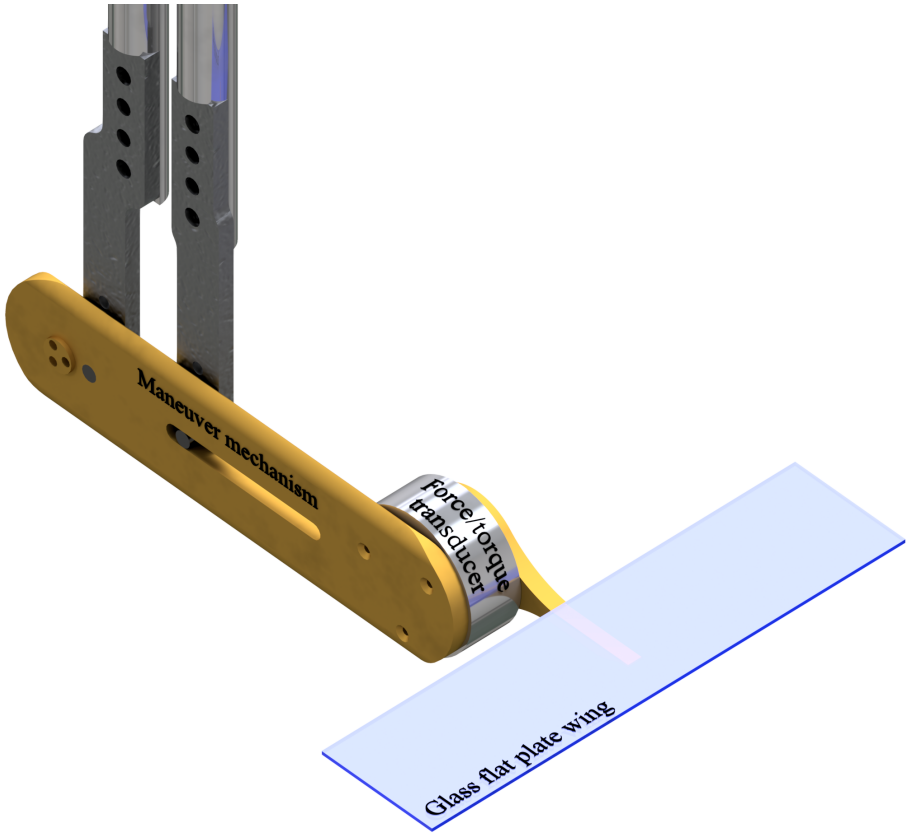

Figure 2.2: CAD rendering of the glass flat plate wing attached to the force balance and the maneuvering apparatus.

these was made of brass. This metal wing was machined using a computer numerical control (CNC) mill to ensure accurate sizing and edge characteristics. Brass was selected because it is more corrosion resistant in water than aluminum and lighter than stainless steel. The second wing was made of glass to allow for PIV illumination without a shadowed region. Glass was selected over transparent plastics for high bending stiffness. The manufacturing process for the glass wing did not allow the same precision (for square edges in particular), but no difference in results was observed between the two wings. The wing and the apparatus for maneuvering it are shown in figures 2.2 and 2.3.

The static force coefficients of the flat plate wing are shown in figure 2.4. The

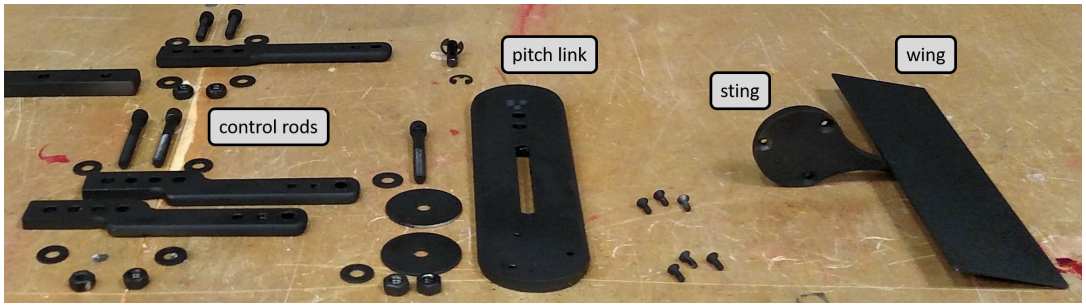

Figure 2.3: The brass flat plate wing and the maneuvering apparatus prepared for installation. Black paint reduces PIV laser reflections.

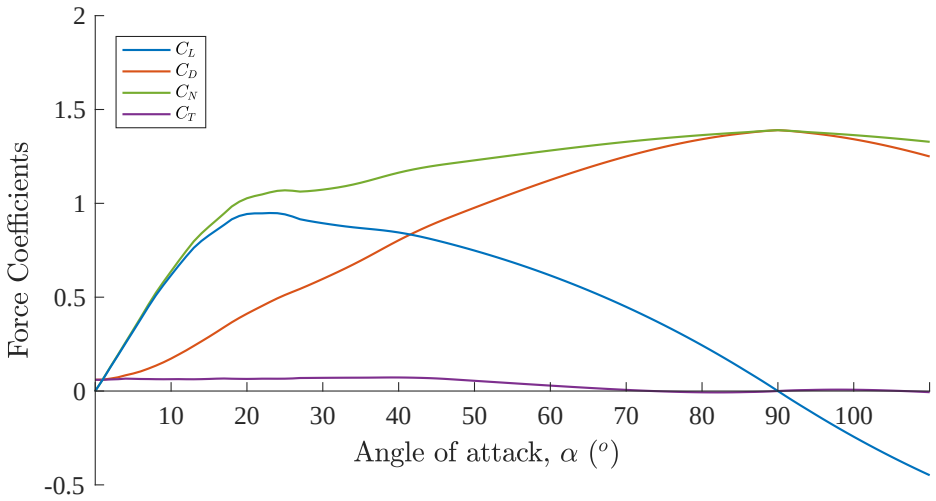

Figure 2.4: Static force coefficients measured for the flat plate wing at $Re = 20{,}000$.

forces are predominantly plate-normal, although a small plate-tangent force is present even at $\alpha = 0°$. The peak lift coefficient is $C_L = 0.95$, produced at $\alpha = 23°$. The plate-normal force coefficient has a local maximum at $\alpha = 25°$ of $C_N = 1.1$, and a peak value of $C_N = 1.39$ at $\alpha = 90°$. This is also the peak drag value and angle. These measurements agree with those published by Ortiz et al. [47] if the difference in wing aspect ratio is properly accounted for.

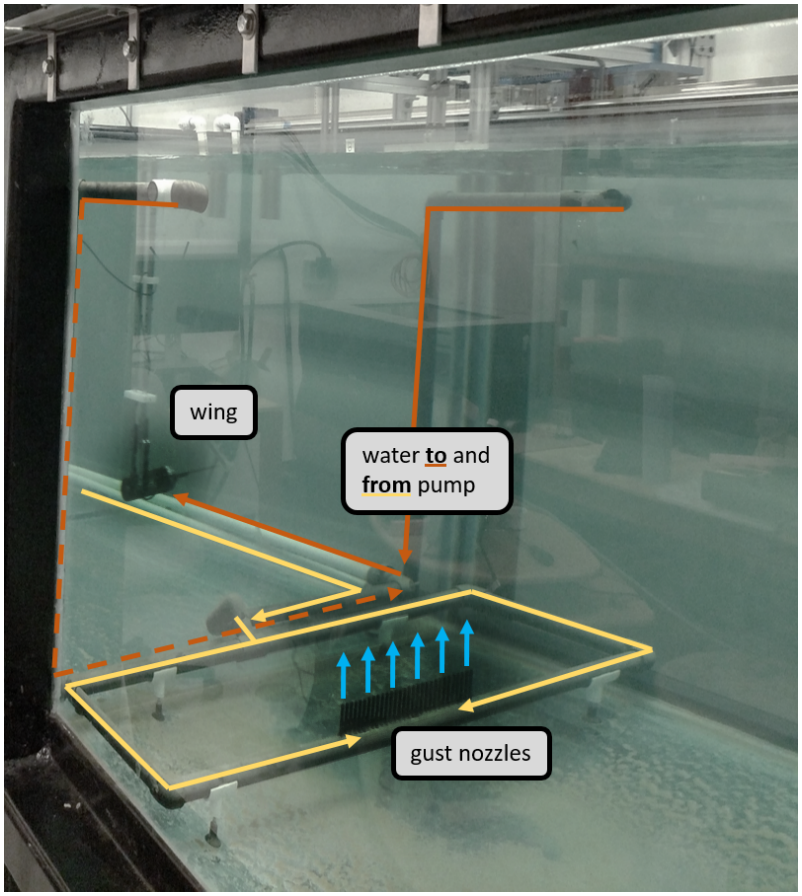

Figure 2.5: The plumbing and nozzle array of the gust generation system. The arrows indicate the flow direction.

2.3 Gust generator

The fluid gust created for these experiments was a vertically-oriented, approximately planar water jet. A pool circulation pump moved 60 gallons of water per minute through a recirculating system with an outlet manifold made of 30 cylindrical nozzles, shown in figure 2.5. The nozzles had $\frac{1}{4}$ in. inner diameter and were spaced $\frac{1}{2}$ in. center-to-center. The conical jets that form from each nozzle merge into one planar jet above the nozzle array. This jet passes through a size 28 steel mesh (0.7 mm wire spacing, 52% open area) which was used as a low-profile flow

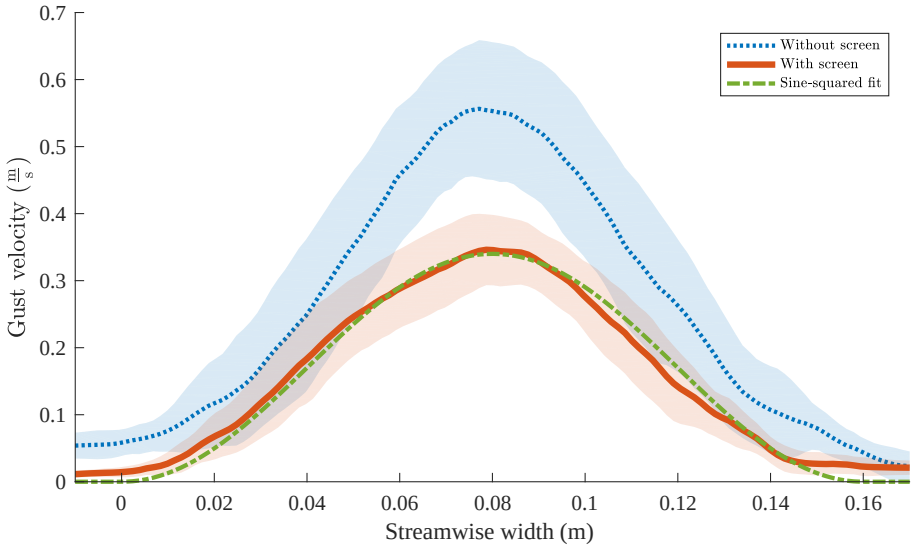

Figure 2.6: Streamwise gust velocity distribution extracted from PIV with and without the flow-straightening screen. The shaded region around each curve shows the standard deviation of the velocity over time. The gust profile was approximated as $V(x) = 0.34 \sin\left(\frac{\pi x}{0.16}\right)^2$ for $0 \leq x \leq 0.16$.

straightener to remove the streamwise waving of the planar jet. Figure 2.6 shows the velocity profile of the gust with and without the screen. The screen reduces the variations over time (the shaded region in figure 2.6 shows one standard deviation in gust velocity measurements) but also reduces the time-averaged peak velocity of the gust. The jet continues vertically through the water tank to inlet pipes at the top surface, which draw in the water for the pump. This forms a closed loop system with a "free jet" (conceptually similar to Kuethe's design in section 1.4). Away from the spanwise ends of the nozzle array, the gust can be considered approximately two-dimensional and can be characterized by a streamwise distribution of transverse velocity. The gust system manifold is 37 cm wide, which covers 1.85 times the wingspan. This leaves 1.7 chord-lengths between each wingtip and the spanwise ends of the manifold, so the wing is within the two-dimensional flow region of the gust.

The uniformity of the spanwise velocity distribution was confirmed qualitatively with dye flow visualization. At the height above the nozzles used for all tests, 15 cm, this gust formed a canonical sine-squared velocity profile with a span of 16 cm and a peak velocity of 0.34 $\frac{\text{m}}{\text{s}}$. This best-fit profile can be compared to the mean measured gust velocity profile in figure 2.6.

2.4 Gust encounter kinematics and parameter matrix

Force data was collected as the flat plate wing was towed at constant velocity and constant pitch angle through the transverse gust. The size of the tow tank limits the total towing distance to approximately 6 m. Figure 2.7 shows the tested kinematics, which in detail were: 6 chord-lengths of constant acceleration from rest to full towing speed, 25.9 chord-lengths of constant velocity before reaching the gust, 3.2 chord-lengths in the gust, 60.9 chord-lengths of constant velocity after the gust (90 total chord-lengths, 4.5 m, of constant velocity towing), and finally 6 chord-lengths of constant acceleration to return to rest.

Those kinematics were repeated for several values of towing velocity and angle of attack. The tested gust encounter cases were limited by the force measurement sensitivity for low speeds and by the motor capabilities for high speeds. Tests were conducted at freestream Reynolds numbers of $\text{Re} \equiv \frac{U_\infty c}{\nu} =$ 10,000, 20,000, and 40,000. These three cases can be described by their corresponding wing velocities of $U_\infty = 0.2$, 0.4, and 0.8 $\frac{\text{m}}{\text{s}}$, or by the associated peak gust ratios of $G = 1.68$, 0.84, and 0.42. The pitch angle of the wing was also varied from $-4°$ to $45°$. The primary

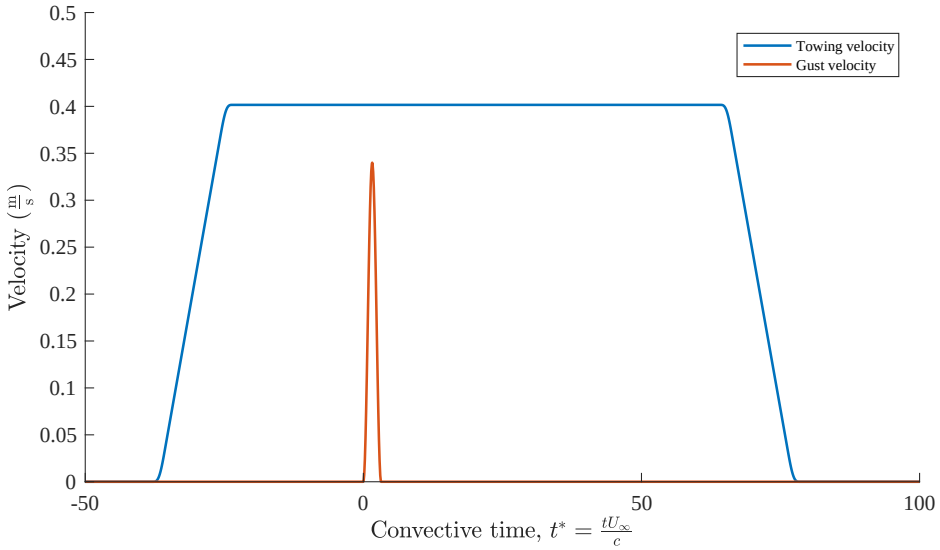

Figure 2.7: The horizontal towing velocity of the wing and the vertical gust velocity at the leading edge of the wing over the course of a $Re = 20{,}000$ case.

cases tested at each Reynolds number were 5°, 10°, 15°, 20°, and 45°; these cases are emphasized with bold pitch angles in table 2.1, and were repeated between 4 and 10 times. A distribution of additional low angle cases were tested; these cases were measured only once or twice. 140 total measurements were made between the 30 cases.

The irregular cases in the test matrix were caused by hardware limitations of the motion control system. The system was able to set a specified wing pitch angle by feedback control, but this could allow the wing to change angle of attack briefly during the gust encounter (as it was perturbed by the gust forcing). This was avoided by increasing the input threshold for motion of the slide-crank mechanism which was controlled by torque on the pivoting and sliding pins. This also worked against the motion control system, which occasionally became fixed at an angle other

Table 2.1: Cases tested transverse gust encounters characterized by gust ratio and pitch angle.

Reynolds number	Gust ratio, G	Pitch angles, α (^{o})
10,000	1.68	2, 3, 4, **5**, 6, 7, **10**, **15**, **20**, **45**
20,000	0.84	2, 4, **5**, 6, **10**, **15**, **20**, **45**
40,000	0.42	-4, -1, 0, 1, 3, **5**, 6, 7, **10**, **15**, **20**, **45**

than the prescribed angle. Instead of discarding the collected force data in those cases, the achieved angles were recorded and new repetitions were measured until the prescribed angles were accurately reached for enough measurements. This issue was resolved by further PID tuning before the more recent tests described below.

2.5 Plunge maneuver kinematics and parameter matrix

The maneuver for all cases in this study was the sine-squared gust, also known as the one-minus-cosine gust due to the identity $2\sin(\theta)^2 = 1 - \cos(2\theta)$. This profile was chosen to match the canonical approximation of fluid gust encounters [1] to facilitate comparison of this data to transverse gust encounter data. The plunge velocity of the wing during the maneuver was:

$$V(t) = V_p \sin\left(\frac{\pi t}{T}\right)^2 \quad \text{for} \quad 0 \leq t \leq T \tag{2.1}$$

where V_p is the peak plunge velocity and T is the maneuver duration. This is shown in figure 2.8. By integration, the vertical distance traveled during the gust is $h = \frac{1}{2}V_pT$. The wing traveled at constant horizontal velocity, U_∞, therefore

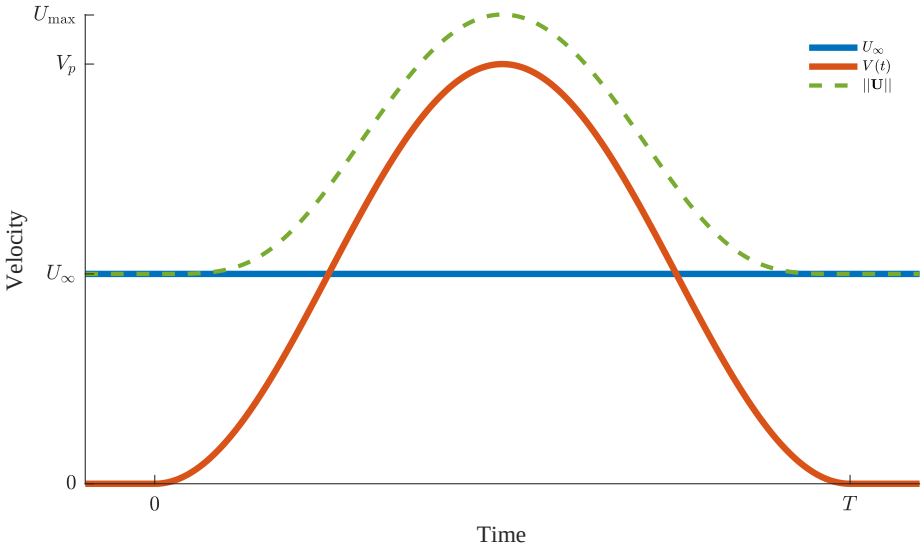

Figure 2.8: Plunge velocity profile for $\frac{h}{w} = 1$.

the horizontal distance covered during the gust was $w = U_\infty T$. The duration and chord-normalized size of the maneuver (T, $\frac{w}{c}$, and $\frac{h}{c}$) are the controlled variables for this experiment.

This study measured forces for 135 different plunge maneuvers, which primarily varied in height and width traveled by the wing during the maneuver. There were 72 unique combinations of height and width, each ranging from 2.5 cm to 30 cm, or $0.5c$ to $6c$. The path of the wing during three of these plunge maneuvers and the endpoints of each maneuver are plotted in figure 2.9. The plunge begins at the top left corner of the plot and ends at the associated endpoint marker for each case.

Two plunge speeds were tested. Each of these 72 maneuver sizes was tested at a duration set so that the peak total velocity was $U_{\max} = 0.75\,\frac{\text{m}}{\text{s}}$ by:

$$T = \frac{\sqrt{(2h)^2 + (w)^2}}{U_{\max}} \tag{2.2}$$

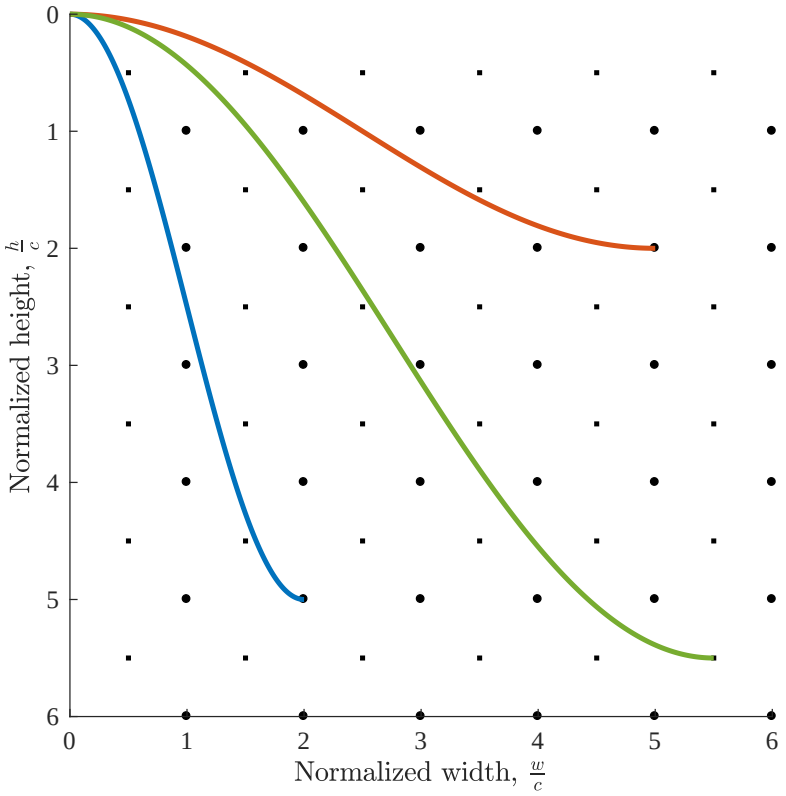

Figure 2.9: Plunge profile for 3 of the 72 maneuver sizes in the test matrix. The marked grid of points represent the end location of each tested maneuver.

Cases with integer-valued sizes, plotted as circles in figure 2.9, were tested again at $U_{\max} = 0.25\,\frac{\text{m}}{\text{s}}$. Nine of the original cases were repeated at angles of attack above zero: 10°, 20°, and 45°. The full test matrix is presented in table 2.2.

The Reynolds numbers based on the peak total velocity, $U_{\max}$, are 37,500 and 12,500. The Reynolds numbers based only on the horizontal velocity, U_∞, vary between 1,038 ($w = 1c$, $h = 6c$, $U_{\max} = 0.25\,\frac{\text{m}}{\text{s}}$) and 36,895 ($w = 5.5c$, $h = 0.5c$, $U_{\max} = 0.75\,\frac{\text{m}}{\text{s}}$).

The positions of the motors were recorded during each test at 32 Hz. Figure 2.10 shows the plunge kinematics as prescribed and performed over three repetitions

Table 2.2: Experimental test matrix characterized by size and speed of the plunge maneuver. Colors correspond to cases in figure 2.9

$\frac{w}{c}$	$\frac{h}{c}$	$U_{\max}\left(\frac{\text{m}}{\text{s}}\right)$	α
0.5	0.5, 1.5, 2.5, 3.5, 4.5, 5.5	0.75	0°
1	1, 2, 3, 4, 5, 6	0.25, 0.75	0°
1.5	0.5, 1.5, 2.5, 3.5, 4.5, 5.5	0.75	0°
2	1, 2, 3, 4, **5**, 6	0.25, 0.75	0°
2.5	0.5, 1.5, 2.5, 3.5, 4.5, 5.5	0.75	0°
3	1, 2, 3, 4, 5, 6	0.25, 0.75	0°
3.5	0.5, 1.5, 2.5, 3.5, 4.5, 5.5	0.75	0°
4	1, 2, 3, 4, 5, 6	0.25, 0.75	0°
4.5	0.5, 1.5, 2.5, 3.5, 4.5, 5.5	0.75	0°
5	1, **2**, 3, 4, 5, 6	0.25, 0.75	0°
5.5	0.5, 1.5, 2.5, 3.5, 4.5, **5.5**	0.75	0°
6	1, 2, 3, 4, 5, 6	0.25, 0.75	0°
1	1, 3, 6	0.75	10°, 20°, 45°
3	1, 3, 6	0.75	10°, 20°, 45°
6	1, 3, 6	0.75	10°, 20°, 45°

for one of the most aggressive plunge maneuvers, $w = 1c$, $h = 1c$. Minor overshoot of 0.04 $\frac{\text{m}}{\text{s}}$ (6% of the peak velocity) was recorded at the end of the maneuver. The motors follow the prescribed kinematics even more closely in most cases — the average overshoot is 0.6% of the plunge velocity.

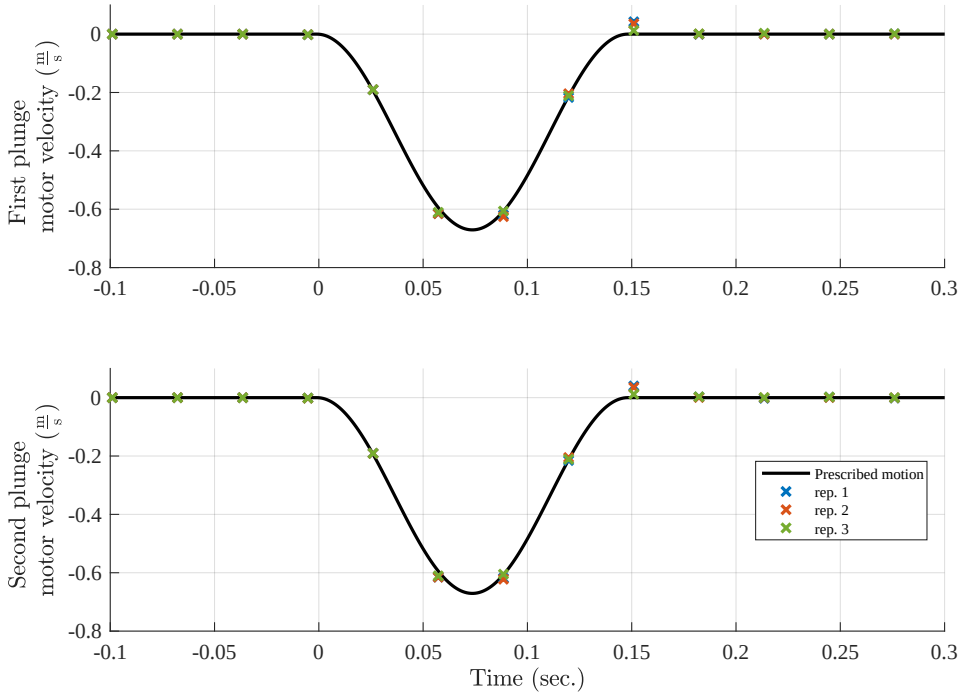

Figure 2.10: Plunge motor velocities as prescribed compared to the performed motor motions over three repetitions of an aggressive plunge maneuver ($w = 1c$, $h = 1c$).

2.6 Force measurements

The forces produced by the gust encounters and plunging maneuvers were measured using a six degree-of-freedom force and torque balance (ATI Mini-40) sampled at 1 kHz. The force balance was located between the slide-crank pitch mechanism and the sting, as is visible in figure 2.2. Internal strain readings were converted to wing-fixed forces and moments using the manufacturer's calibration. Figure 2.11 shows lift coefficient measurements for eight repetitions of an example gust encounter case. The gust encounter takes place during the shaded portion of the x-axis.

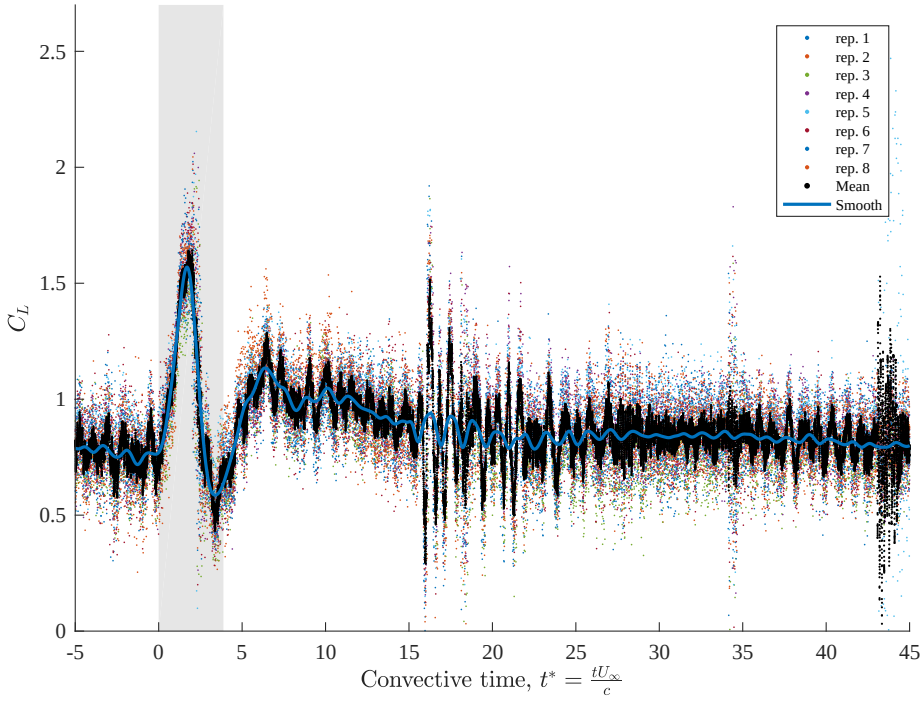

Figure 2.11: Lift measurements from individual repetitions, ensemble average, and post-processing for one gust encounter case. $\alpha = 45°$ and $G = 0.84$ ($Re = 20{,}000$).

The data packets were transmitted from the moving tow tank carriage to the stationary control computer by a dedicated wireless network. The data transfer took place real-time and was limited to User Datagram Protocol (UDP) to achieve that speed. That protocol is simple and efficient, but is unconfirmed, so any individual data packets which were transmitted incorrectly or incompletely were unrecoverable. Data was recorded at a high rate to ensure that enough temporal measurement resolution was achieved even when some data points were lost. If a single run of data collection (one repetition of one case) lost more than 5% of the data packets, it was discarded and restarted.

Mechanical vibrations created measurement noise that limited the lowest viable

Reynolds number. The standard deviation of repeated measurements was 0.1 N, which corresponds to a measurement uncertainty of ±2% of the mean forces measured for cases at Re = 40,000, ±7% for cases at Re = 20,000, and ±30% for cases at Re = 10,000.

The guide rails and magnetic propulsion of the towing carriage were not perfectly smooth and sometimes introduced substantial transient vibrations to the measured forces, as is visible in figure 2.11 at t^* = 16. For all plunge maneuver force data the starting location of the test is shifted by a random movement of up to ±100 mm so that the fixed location of the track bumps appear as varying locations in the experiment. This minimizes the effects of the track unevenness on the ensemble-averaged data. However, the location of the gust system in the tank was not variable, so the starting location of the gust encounter tests could not be varied.

2.6.1 Post-processing

Force measurements for this experiment were repeated and the results were ensemble-averaged. However, the force data collection device and wing kinematics control computer operated on separate internal clocks, so the measurements had to be synchronized to the kinematics timeline before averaging or further analysis was possible. The kinematics and force measurements were triggered to begin simultaneously, so each could be simply considered relative to the start time. This was found to introduce an error of up to 0.1 s, which significantly affected the averaged

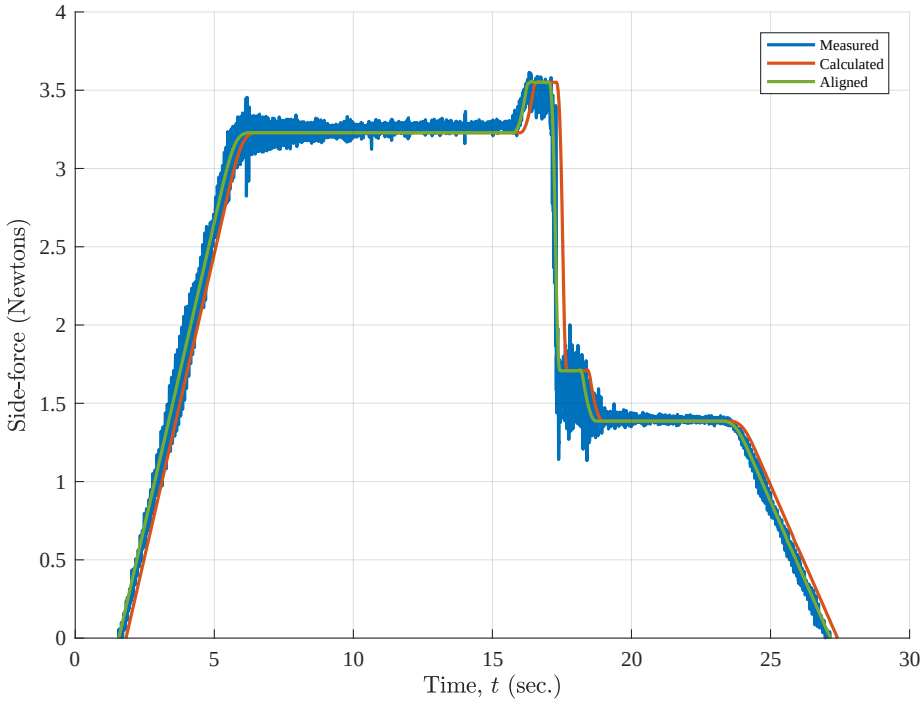

Figure 2.12: Force measurements were aligned to kinematics by correlation of water pressure and transducer depth.

results. Instead, the measured side-force was cross-correlated with the expected side-force — based on the transducer's depth in the water and the total velocity — to find the best alignment. This alignment can be seen in figure 2.12, which shows the side-force for one of the plunge maneuver repetitions (for which $h = 1$ and $w = 1$). The experimental hardware is symmetric, so the measured side-force is only affected by the water pressure at the transducer's measurement face. The changes in pressure can be approximated as a function of transducer depth and speed, $\Delta P = \rho g \Delta h + \frac{1}{2}\rho \left(\Delta U_{\text{total}}\right)^2$. The initialization of the test article to the starting position ($t < 6$ in figure 2.12), the plunge maneuver ($t \approx 17.5$), and the return of the test article to rest ($t > 23$) each provide significant pressure changes with which the kinematics and force measurements can be synchronized. In this example, the

force measurements timing (in blue) began 0.26 seconds after the kinematics timing began (from which the red line was estimated). This separation was identified by normalized cross-correlation of these quantities; the appropriately aligned results are shown in green.

The data alignment process identified the true time-stamp for each measurement but each repetition had a slightly de-synchronized sample timing, so the ensemble-averaged data had to be created based on linearly-interpolated points. This was acceptable because of the high sample rate; the maximum interpolation "distance" was 0.5 ms and the unsteady events being studied lasted at minimum 8 ms and on average 500 ms. Measurement points which were lost by the UDP transfer were not used in the ensemble average; individual data points for which this occurred were therefore averaged over one or two fewer repetitions than the overall force history.

Measurement noise and mechanical vibrations created visible noise in the measured force data. For the remainder of this document, presented force data has been filtered using weighted quadratic local regression ("loess" in Matlab). This particular filter reduces noise effectively but also preserves the peaks measured during these unsteady events. Basic low-pass frequency filters were considered as an alternative, but were found to either have too little effect or to truncate the peak forces depending on the cut-off frequency. The span of the loess filter was set based on convective time so that the filter covered $t^* = 2$ in the gust encounter cases and $t^* = 0.2w$ in the plunge maneuver cases. It can be seen in figure 2.11 that this did not truncate the peak force or otherwise distort the force history.

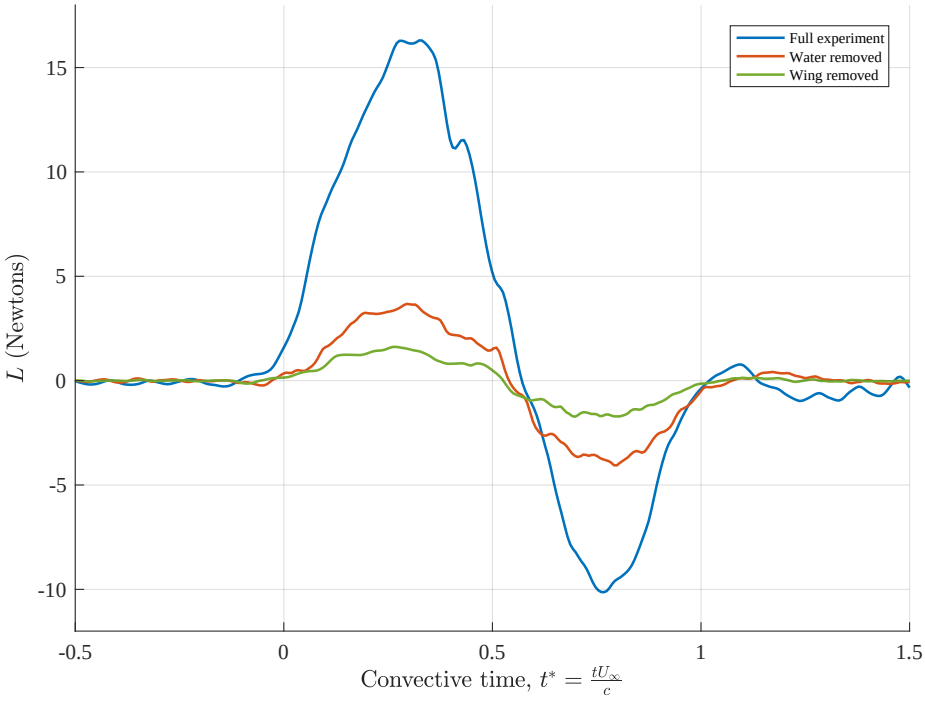

Figure 2.13: Measured lift during a plunge maneuver repeated after draining the tow tank water and again after removing the test article.

2.6.2 Dynamic calibration

The mass of the wing, sting, and parts of the force balance contribute to the measured inertial loads during the plunge maneuver cases. To isolate the aerodynamic contributions to those forces, a dynamic calibration procedure was performed on 13 of the plunge test cases by repeating those measurements in air instead of water, and then repeating each of those cases again with the wing and sting removed. By comparing the forces measured under those three conditions, the mass of each component could be verified and the inertial load of the force transducer itself could be identified. An example of these force results is shown in figure 2.13.

The mass of the glass wing was 38 g, the brass wing was 126 g, the sting was

88 g, and the part of the force balance on the measurement side of the strain gages was determined to be 120 g. The calibration tests in air do experience added-mass forces, but they are proportional to the fluid density, and so are only 1.2% of the force experienced in water. For the remainder of this document, the inertial forces caused by the mass of the test hardware have been removed from the presented measurements (this is only relevant in the plunge maneuver cases).

Dynamic calibration is often also used to identify the dynamic response of the measurement equipment. However, in this experiment the effective frequency of the plunge maneuver was at most 0.5% of the force balance's resonant frequency of 3.2 kHz. Therefore, the harmonic response of the force balance did not affect the measurements and was not further quantified here.

2.6.3 Lift normalization

In cases of high gust ratio, G, or high plunge aspect ratio, $\frac{h}{w}$, the majority of the total relative fluid velocity mid-event is contributed by the unsteady vertical velocity component. In these cases the typical force normalization by freestream dynamic pressure leads to unreasonably high force coefficients. The gust ratios in this experiment did not reach high enough values to cause difficulty in comparisons, but several of the plunge cases did. The left axis of figure 2.14 shows lift coefficients for six plunge maneuvers, but most of the data is indiscernible because of the excessive magnitude of the normalized lift in the $w = 1c$, $h = 6c$ case. Because of this, the measured lift in each plunge case is also presented as normalized by the mean kinetic

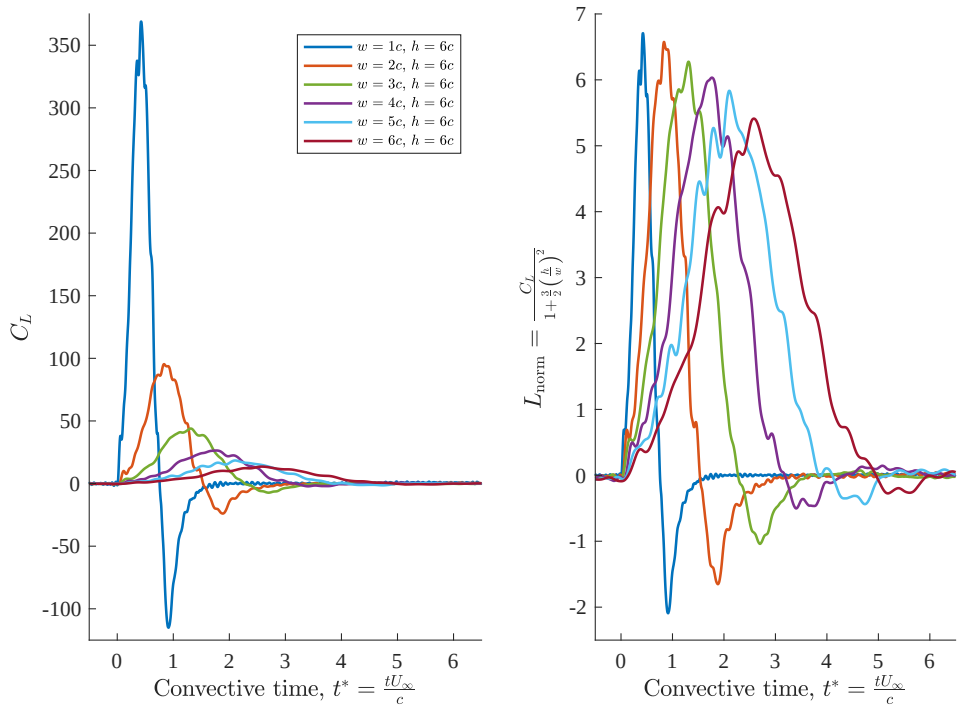

Figure 2.14: Lift normalization by freestream dynamic pressure (left) and by mean specific kinetic energy (right). The exaggerated magnitude of forces for the high plunge aspect ratio case on the left diminishes the differences between the lower aspect ratio cases. The alternate normalization removes this effect, making all cases visibly comparable.

energy per unit mass during the maneuver [48]. To see the difference, take the typical definition of lift coefficient,

$$C_L = \frac{L}{\frac{1}{2}U_\infty^2 \rho S}, \tag{2.3}$$

which exaggerates the lift produced by maneuvers with high velocity ratios since the normalizing factor, U_∞, is only a small component of the total velocity. If the dynamic pressure part of the equation is replaced by a term which incorporates the unsteady vertical velocity magnitude then the normalizing factor better reflects the

total velocity of the maneuver. The mean specific kinetic energy is defined as:

$$\frac{\bar{KE}}{m} = \frac{1}{T}\int_0^T \frac{1}{2}\left(U_\infty^2 + V(t)^2\right) \mathrm{d}t \tag{2.4}$$

For the sine-squared plunge profile studied here (equation 2.1), the new normalization of lift coefficient becomes:

$$L_{\text{norm}} = \frac{L}{\frac{1}{2}\left(U_\infty^2 + \frac{3}{8}V_p^2\right)\rho S} \tag{2.5}$$

$$\therefore \quad L_{\text{norm}} = \frac{C_L}{1 + \frac{3}{2}\left(\frac{h}{w}\right)^2} \tag{2.6}$$

This new normalization allows for the direct comparison of the varying plunge maneuvers, as seen in the right axis of figure 2.14. This scaling reduces the magnitude of the normalized lift for the most aggressive plunge in the current data ($w = 0.5c$, $h = 5.5c$) by a factor of nearly 200, which greatly improves the quantitative and visual comparisons of the aggressive and gentle plunging force data. In chapter 4 the forces will be presented using both normalizations for comparison.

2.7 Flow velocity measurements

Particle imaging velocimetry (PIV) was used to measure the flow around the wing. A Phantom v641 camera recorded 4 MP images (2560 × 1600 pixels) at 1 kHz as it was towed along with the wing. The water was seeded with hollow glass spheres of 37 µm diameter which were illuminated by a Litron LDY300 pulsed Nd:YLF laser.

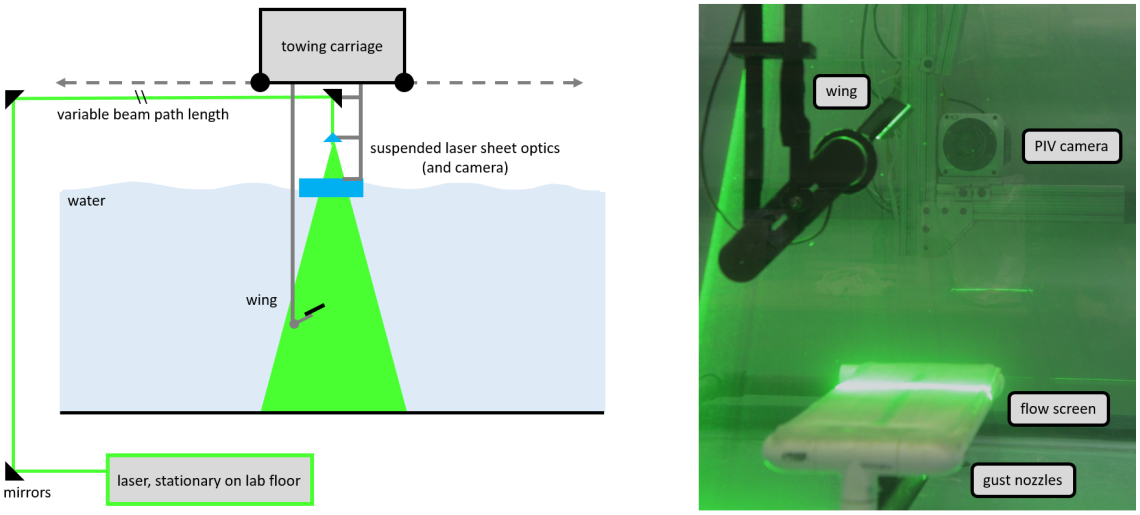

Figure 2.15: Diagram of PIV measurement setup. The camera and laser optics are suspended from the towing carriage outside of the tank so that each travels along with the wing.

The beam was spread into a thin sheet by a Powell lens. The measurement plane was aligned with the towing velocity and the gust velocity, and intersected the wing one chord-length from the centerline — and, due to the aspect ratio of four, also one chord-length from the near-camera wing tip. The laser sheet optics were also towed on the carriage so that the illuminated region traveled with the wing. This arrangement is shown in figure 2.15. The laser sheet passed through the free water surface inside of an acrylic carrier block to avoid distortion of the laser sheet by refraction. The field of view, shown in figure 2.16, was $25 \times 15\,\text{cm}$. This resulted in a spatial resolution of 0.1 mm per pixel or 500 pixels per chord-length. The normalized temporal resolution was 150 images per convective time.

Only one PIV case is discussed in the current work[1]. This case was recorded using a towing velocity set equal to the characterized gust velocity, $U_\infty = 0.34\,\frac{\text{m}}{\text{s}}$.

[1]During subsequent PIV measurements, it was observed that the generated gust velocity declined over several days. The water pump system failed and was found to be unrepairable.

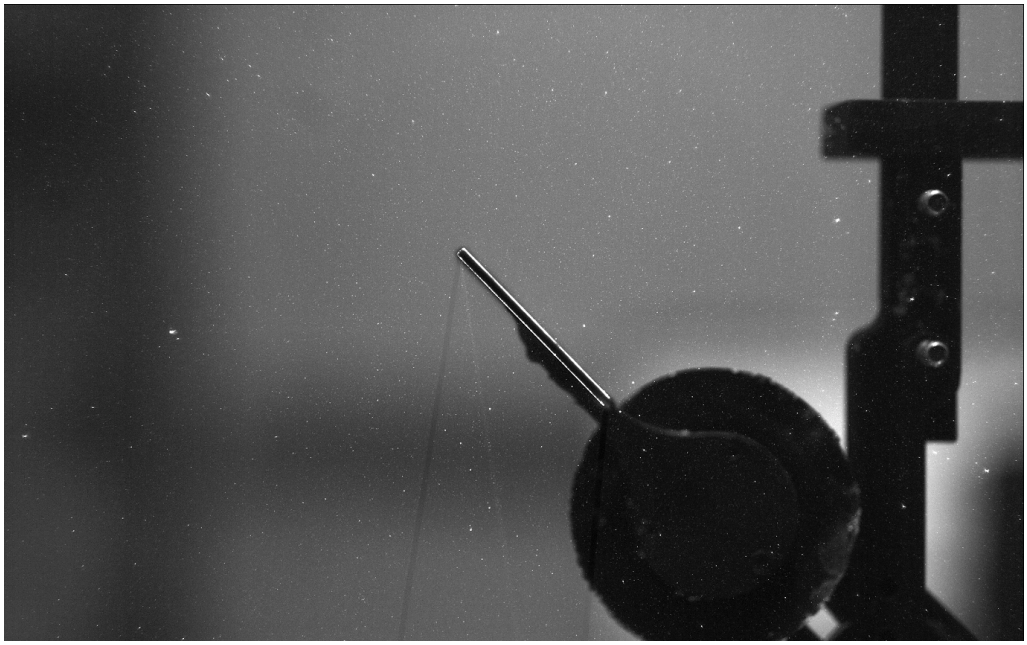

Figure 2.16: The field of view for PIV measurements. In this case, $\alpha = 45^{\circ}$. The wing is centered in the image and is visible by the laser illumination at its surface (even glass reflects a little of the laser). The force transducer is hidden behind the black foil disc between the sting and pitch mechanism, which are visible in the lower right of the image.

The wing was set at $\alpha = 45^{\circ}$ and was centered in the field of view.

The captured images were analyzed in sequence using DaVis software, which ran multi-pass cross-correlation to measure the seed particle displacements. The interrogation regions were 32×32 pixel windows for the first coarse pass and 16×16 pixels for the second pass. The second pass used a circular weighting to remove diagonal bias. Each pass used 50% interrogation region overlap to maximize vector resolution without overly sacrificing measurement independence. The final vector spacing was 0.75 mm, or 67 vectors per chord-length. The resulting vector fields were post-processed using local-median outlier removal (7% of vectors were replaced) and no smoothing.

The velocity fields were used first as flow visualization to observe the vortex

dynamics during the transverse gust encounters. Flow vorticity was then calculated to aid in identifying vortices and to investigate quantitative correlation between near-wing vorticity and transient force production.

2.8 Chapter summary

A water-filled towing tank was outfitted with a recirculating gust generation system to experimentally investigate unsteady force production by transverse gust encounters and plunge maneuvers. Forces were measured using a six degree-of-freedom force and torque balance and flow velocities were measured using PIV towed along in the wing reference frame. Gust encounters were recorded for various towing velocities for which $10{,}000 \leq Re \leq 40{,}000$ and wing pitch angles of $-4^\circ \leq \alpha \leq 45^\circ$. Forces and flow velocities from gust encounters are presented in chapter 3. Plunge maneuvers which followed the canonical sine-squared gust velocity profile were also investigated. Plunge maneuvers were varied in the distance traveled in the streamwise and stream-normal directions during the maneuver, the duration of the maneuver, and wing pitch angles between $0^\circ \leq \alpha \leq 45^\circ$. Freestream Reynolds numbers for plunge maneuvers were $1{,}038 \leq Re \leq 37{,}500$. Forces from plunge maneuvers are presented in chapter 4.

Chapter 3: Force production in transverse gust encounters

This chapter will present the force and flow measurements made during sine-squared profile transverse gust encounters of a flat plate wing. These observations aid in identifying and quantifying mechanisms of unsteady aerodynamic force production. Transverse gust encounters are investigated for gust velocity ratios between $G = \frac{V_g}{U_\infty} = 0.42$ and 1.86, and for wing pitch angles between $\alpha = -4^\circ$ and 45°. The details of the tested parameter space are presented in section 2.4. The analysis begins with a qualitative description of the recorded force histories and a connection between those forces and the flow structures observed in the measured velocity fields. Several force prediction models are compared to the measured force histories. Force predictions made by these models are further compared to measured forces by extracting peak forces from each gust encounter as characteristic values.

3.1 Gust encounter force history features

The effects of the gust encounter on the force coefficients of the flat plate wing are visible in figure 3.1. The x-axis of this figure is convective time, $t^* = \frac{tU_\infty}{c}$, the number of chord-lengths traveled by the wing since its leading edge entered the gust. In the case displayed in figure 3.1, the angle of attack is 45° and the gust ratio is

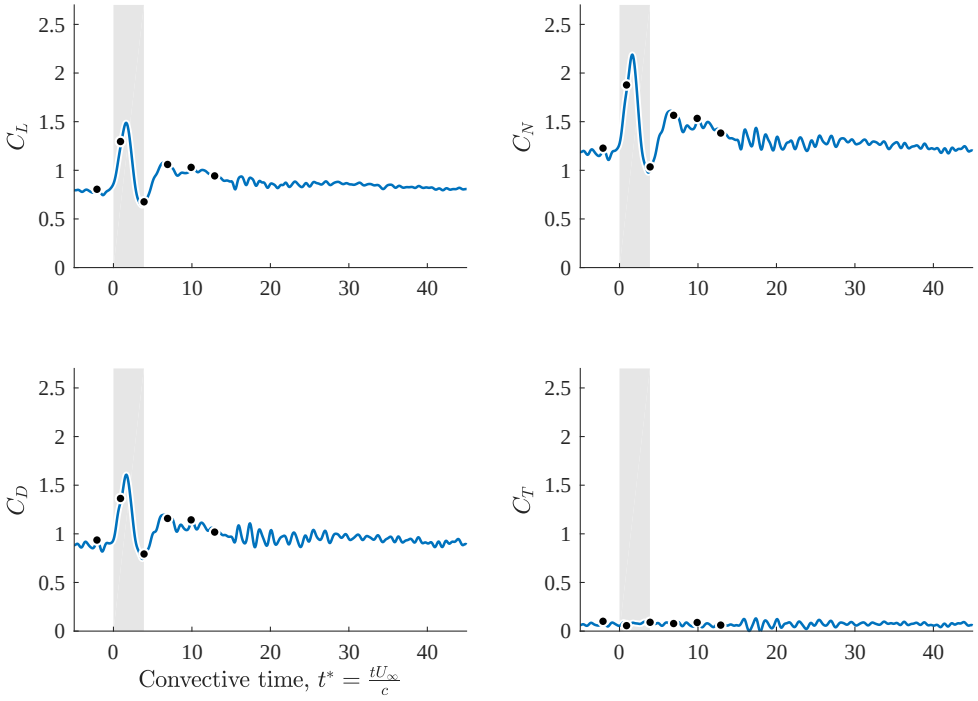

Figure 3.1: Force coefficient history for gust encounter of flat plate at 45° and a gust velocity ratio of 0.84. The wing and gust overlap during the shaded portion of the x-axis; the leading edge of the wing enters the gust at the left edge of this region, $t^* = 0$, and the trailing edge of the wing exits the gust at the right edge of the region, in this case $t^* = 3.88$. The forces are oriented and normalized relative to the towing velocity of the wing. The circles are for reference in figure 3.2.

0.84. The forces are normalized by the towing dynamic pressure. The lift and drag decomposition is performed relative to the constant horizontal towing velocity. There are significant plate-normal forces, but the tangential forces are nearly constantly zero as is expected for this thin, flat wing at the tested Reynolds numbers. Because the wing is thin and flat, the forces at the narrow edges can be neglected. This means that the forces are approximated as acting only on the top and bottom wing surfaces, so the pressure forces on the wing are entirely plate-normal and skin-friction forces are entirely plate-tangent. The magnitude of the measured plate-normal forces

as compared to the plate-tangent forces indicates that pressure is the dominant mechanism of force production here rather than skin friction.

As the wing enters the gust, the total local velocity increases and the relative angle of incidence between the wing and the total fluid velocity increases. Both of these effects tend to increase the force production on the flat plate (until the incidence angle increases beyond 90°). In the example in figure 3.1, the normal-force coefficient increases from 1.2 before the gust is reached to a peak of 2.2 during the gust encounter. The relative increase in peak force production, 83%, was slightly greater than the relative increase in peak dynamic pressure, 71%.

As the wing exits the gust, the force production drops below the steady value momentarily. This event is not adequately explained by the variations of total velocity and incidence angle, each of which return to the steady towing values without overshoot. The local minimum in forces observed here is the first clear indication that the force production by this gust is significantly affected by flow unsteadiness.

After the wing exits the gust, the force production rises again above the steady values, although not as high as was observed while the wing was in the gust. The nominal flow conditions at this time are the same as at all other points outside of the gust, but the forces are temporarily still affected by the gust encounter. Because the effects of the gust on force production last longer than the gust encounter itself, only a force model which incorporates the flow history can properly capture the gust recovery behavior.

3.1.1 PIV flow velocity measurements

Figure 3.2 shows sequential velocity and vorticity fields captured by particle imaging velocimetry (PIV) during a similar gust encounter to the example case described above. For the PIV data collection, the wing was slowed to the measured gust velocity, so the gust ratio is changed slightly to $G = 1.0$. The flow features associated with the force history displayed in figure 3.1, for which $G = 0.84$, are expected to be qualitatively the same as observed in the PIV results. The circles in figure 3.1 highlight the associated times of each of the frames in figure 3.2.

Figure 3.2a shows the wake of the wing during steady towing before the wing reaches the gust. The flow is fully separated and the wake extends horizontally. Periodic vortex shedding occurs during the steady towing, but compared to the transient effects of the gust the forces at this moment can be considered steady.

Figure 3.2b shows the flow around the wing one chord-length after entering the gust. The rapid change in flow magnitude and direction causes vortices to form and shed from the leading edge of the wing. The nominal gust velocity at the location of the leading edge is $0.23\,\frac{\mathrm{m}}{\mathrm{s}}$, 69% of the peak velocity. At the same time the velocity at the trailing edge of the wing is only $0.03\,\frac{\mathrm{m}}{\mathrm{s}}$, 8% of the peak velocity. At this moment, the forces on the wing are approaching their peak. The peak measured force is reached at $t^* = 1.6$ — exactly when the leading edge reaches the peak gust velocity. This suggests that the force production is closely tied to the flow conditions at the leading edge of the wing rather than another chord-wise location or a chord-averaged characterization.

The local minimum in forces occurs during the time captured by figure 3.2c, $t^* = 4$. The gust encounter has passed, so the nominal gust velocities at both the leading and trailing edge of the wing are $0\,\frac{\mathrm{m}}{\mathrm{s}}$. A large trailing edge vortex, which is visible in this frame, forms as the gust recovery process begins. Over the previous two chord-lengths traveled, the velocity gradient across the trailing edge of the wing caused exceptionally high positive vorticity production. This concentration of positive vorticity at the suction surface of the wing causes the concurrent lift deficiency.

Similarly, figure 3.2d shows a leading edge vortex over the wing which causes the lift to increase to the secondary peak seen at $t^* \approx 7$ in figure 3.1. This moment is even further removed from the gust encounter, and yet significant unsteady force production still occurs. The large trailing edge vortex in figure 3.2c causes the leading edge shear layer, the line of negative vorticity visible in figures 3.2a and 3.2b, to move downward; its gradual return to horizontal begins with the formation of the large leading edge vortex seen here.

Figures 3.2e and 3.2f look increasingly similar to the steady condition seen in figure 3.2a, but only after 20 more chord-lengths traveled do the forces return to their steady values. It appears that the alternating vortex shedding from the leading and trailing edges gradually decreases in vortex strength from the maximum seen in figures 3.2c and 3.2d to the steady shedding present in figure 3.2a.

The influence of near-wing vorticity can also be evaluated quantitatively. Figure 3.3 compares the lift history from figure 3.1 to the positive, negative, and net local vorticity contained in the PIV data of figure 3.2. The quantification of vorticity used

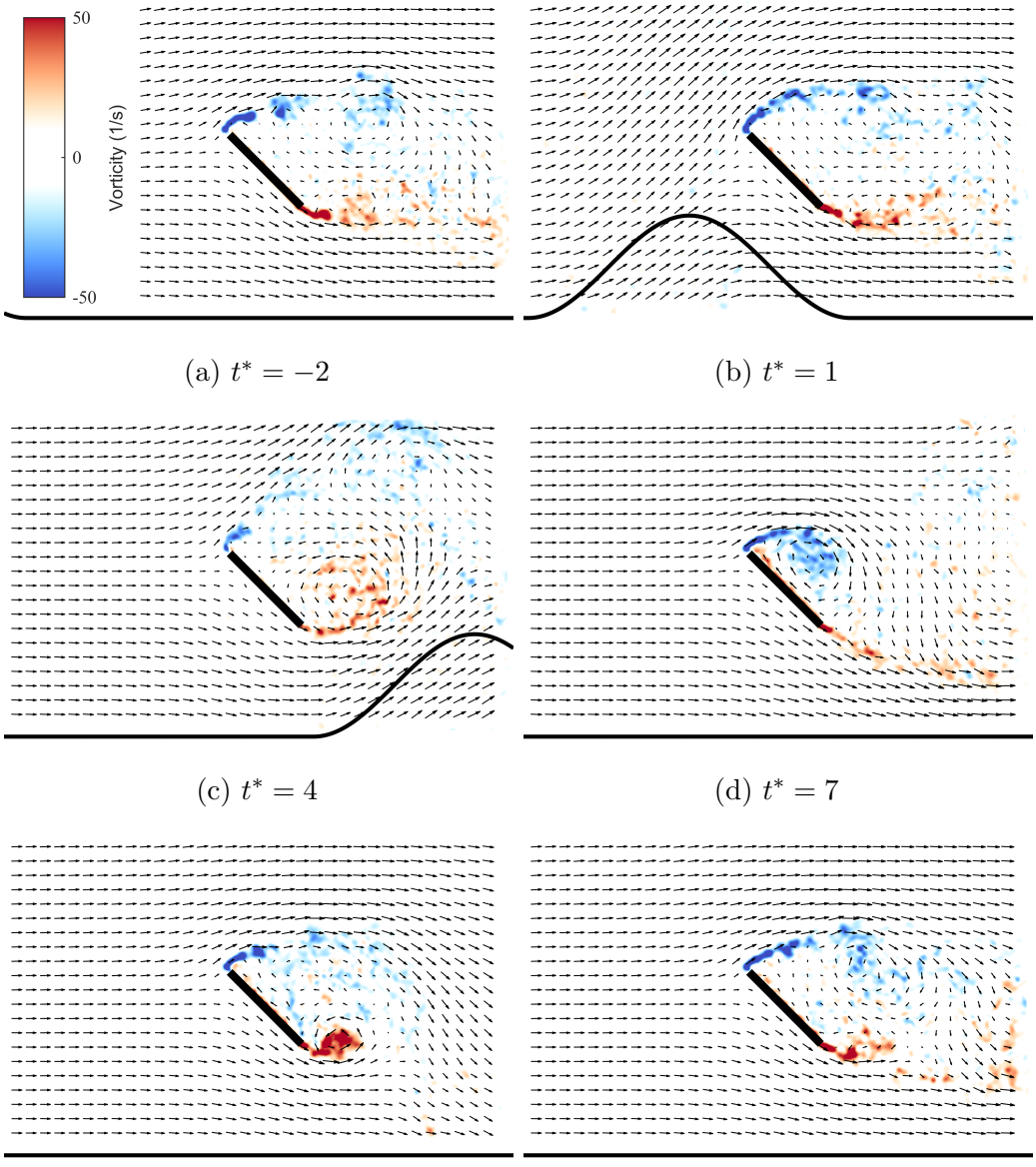

(a) $t^* = -2$ (b) $t^* = 1$

(c) $t^* = 4$ (d) $t^* = 7$

(e) $t^* = 10$ (f) $t^* = 13$

Figure 3.2: PIV results of the gust encounter at $\alpha = 45°$ and $G = 1.0$. The central rectangle indicates the wing position, the background color indicates vorticity, and the curve along the bottom indicates the vertical velocity profile of the gust. Most vectors were omitted for visual clarity; only 1.2% are shown here (one in nine vectors were plotted in each direction).

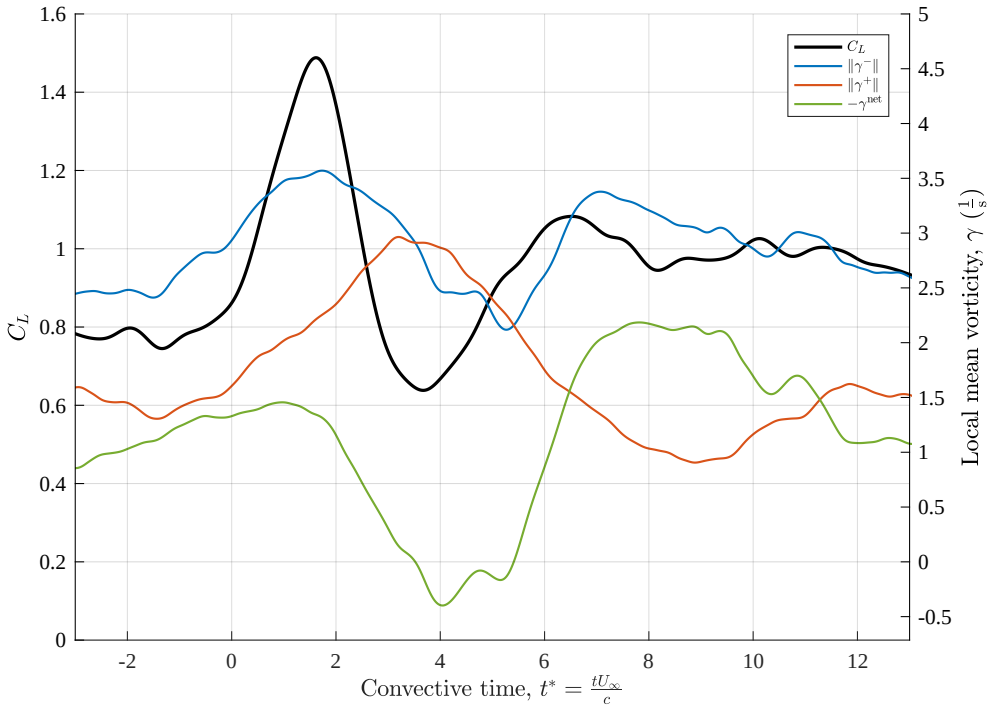

Figure 3.3: Comparison of force history from figure 3.1 to local vorticity for a gust encounter at $\alpha = 45°$ and $G = 1.0$.

in this comparison is an inverse-distance weighted average, which emphasizes the vorticity in the area close to the wing. This is accomplished by scaling each vorticity measurement by the radial distance from the mid-chord of the wing:

$$\bar{\gamma} = \frac{\sum \frac{\gamma}{\sqrt{(x-x_0)^2+(y-y_0)^2}}}{\sum \frac{1}{\sqrt{(x-x_0)^2+(y-y_0)^2}}} \tag{3.1}$$

This weighted average diverges as the radial distance approaches zero. That does not effect the results in the current work because the PIV data is masked at the wing surface.

The near-wing vorticity corresponds closely with the simultaneous force production. The negative circulation is associated with the leading edge vortex

and lift augmentation, while the positive circulation is associated with the trailing edge vortex and lift reduction. Both the lift and the negative local vorticity increase from $t^* \approx 0$ to $t^* \approx 2$, and then decrease to $t^* \approx 4$. The positive local vorticity increases and decreases similarly, but with a delay of $t^* \approx 2$. The peak in positive local vorticity occurs at the same time as the minimum in force production. The net local vorticity at this moment is positive (note that $-\gamma_{\text{net}}$ is displayed in figure 3.3) and the lift is below the steady-state value. After this, a leading edge vortex forms which causes the secondary lift peak. These events correspond to the flow fields in frames 3.2c and 3.2d.

3.1.2 Trends with respect to gust parameters

In order to better understand the effects of gust encounter characteristics on the resulting force production, measured forces were compared for cases which vary in only one gust parameter at a time. Figure 3.4 shows force coefficient histories for three example cases with varied pitch angles of $\alpha = 5°$, $20°$, and $45°$ at the same gust ratio, $G = 0.84$. Note that the wing pitch angle, α, is the constant angle of the wing chord relative to horizontal. The relative fluid velocity is $\theta = \tan\left(\frac{V(t^*)}{U_\infty}\right)^{-1}$, which varies over the gust encounter and in this case peaks at $40°$. The total incidence angle of the fluid on the wing is the sum of these components, $\alpha + \theta$. The peak normal force coefficient increases with pitch angle to $\alpha = 20°$, but then decreases as the pitch angle increases from $20°$ to $45°$. The variation in peak normal force coefficient between these three cases, $C_N \approx 2$ to 2.5, is notably smaller than the

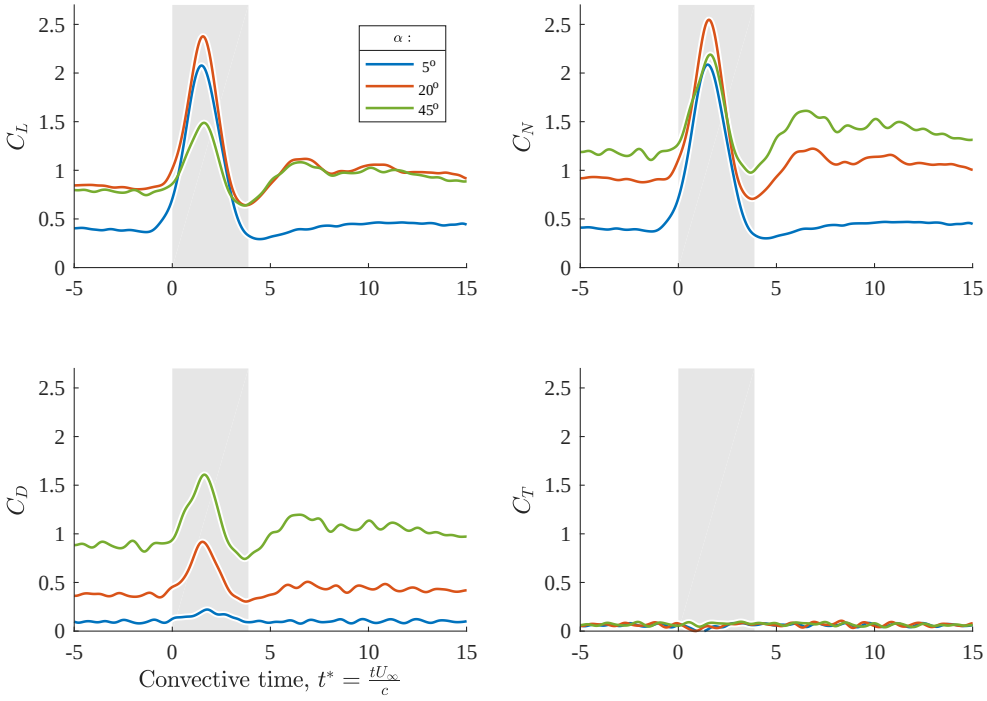

Figure 3.4: Force coefficient history for gust encounters at varied pitch angles. The gust ratio was 0.84 in each case. The wing is in the gust during the shaded portion of the x-axis. The forces are oriented and normalized relative to the towing velocity of the wing.

variation in steady normal force coefficients, $C_N \approx 0.4$ to 1.2. The magnitudes of the force oscillations during the gust recovery — the local minimum and following secondary maximum in force production as the wing exits the gust — are reduced at lower wing pitch angles.

Figure 3.5 shows force histories for example cases with varied gust ratios of $G = 0.42$, 0.84, and 1.68, but the same pitch angle, $\alpha = 45°$. The peak force coefficients during the gust encounter increase with gust ratio (for all other tested pitch angles as well), which was expected since the forces are normalized by the steady flow velocity so higher gust ratios experience higher normalized dynamic

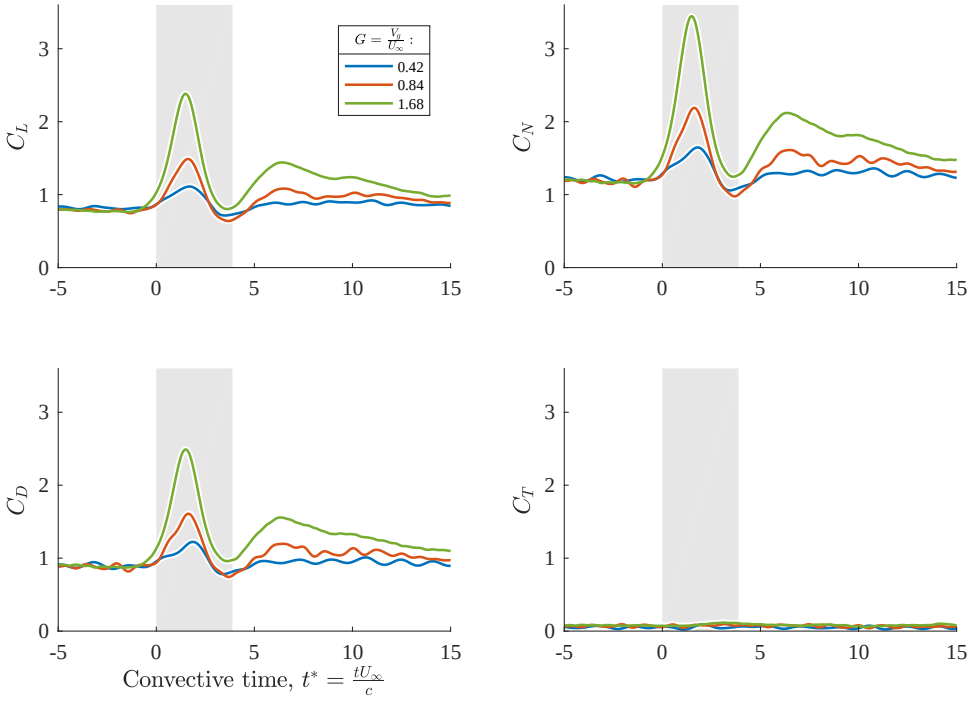

Figure 3.5: Force coefficient history for gust encounters at varied gust ratio. The plate was set at 45° in each case. The wing is in the gust during the shaded portion of the x-axis. The forces are oriented and normalized relative to the towing velocity of the wing.

pressures:

$$\frac{q_{\text{peak}}}{q_\infty} = \frac{\frac{1}{2}\rho\left(U_\infty^2 + V_g^2\right)}{\frac{1}{2}\rho U_\infty^2} = 1 + G^2 \tag{3.2}$$

The unaccounted-for additional dynamic pressure causes the force coefficients to increase with gust ratio. The magnitudes of the force oscillations during the gust recovery also increase with increasing gust ratio.

The timing of the force oscillations as the wing exits the gust were consistently correlated with the trailing edge position. The slight misalignment of those oscillations in figure 3.4 (most visible at the force minimum) is an effect of the reduced projected chord of the wing due to the pitch angle. The leading edge of the wing exits the

gust at the same convective time in each case ($t^* = 3.18$). The time at which the trailing edge exits the gust depends on the pitch angle: $t^* = 4.18$ at $\alpha = 0°$, $t^* = 4.17$ at $\alpha = 5°$, $t^* = 4.12$ at $\alpha = 20°$, and $t^* = 3.88$ at $\alpha = 45°$. The primary example case is $\alpha = 45°$, so the boundary of the shaded area in each figure is $t^* = 3.88$. The connection between trailing edge location and force oscillation timing reinforces the notion that the trailing edge vortex dynamics are the cause of the lift deficiency.

3.2 Force history predictions

The preceding results were used to guide the adaptation of existing models of aerodynamic force production to the current problem of large-amplitude transverse gust encounters. The measured force histories were compared to several theoretical models in order to identify which models accurately predict the force production for segments of the studied parameter space. The captured or missing elements of each model also helped to identify the dominant mechanisms of force production during the gust encounters. The models considered here were a quasi-steady empirical look-up table and three adaptations of Duhamel's convolution integral applied to Küssner's function. One adaptation was based on the empirical data, and two were based on thin-airfoil theory.

The simplest tool for predicting unsteady forces is an empirical quasi-steady model. A quasi-steady model bases instantaneous force predictions on instantaneous conditions, and does not incorporate the flow history in any way. This limits the model to predictions of forces during the gust encounter; the nominal instantaneous

conditions after the gust are unchanging so the forces predicted by this method do not change outside of the gust either. This model is empirical because the force coefficients at any time are based on the associated force coefficients measured during matching steady conditions. This is represented by the following equations, in which a tilde is used to indicate static data from matching flow incidence angles. The relative flow angle in the case of the gust encounter varies across the wing chord, so the static data is matched to a single location, the leading edge:

$$C_N(t) = \widetilde{C_N}(\alpha+\theta(t)) \left(1+\frac{V(t)^2}{U_\infty^2}\right) \tag{3.3}$$

$$C_T(t) = \widetilde{C_T}(\alpha+\theta(t)) \left(1+\frac{V(t)^2}{U_\infty^2}\right) \tag{3.4}$$

The wing-fixed forces are simply scaled by the instantaneous velocity increase, since the force production is proportional to the total velocity but the force normalization is based only on the freestream velocity. The flow-fixed forces need to be scaled and rotated, since $\widetilde{C_L}$ is normal to the total velocity but C_L is normal to the freestream velocity.

$$C_L(t) = \left(\widetilde{C_L}(\alpha+\theta(t))\cos(\theta(t)) + \widetilde{C_D}(\alpha+\theta(t))\sin(\theta(t))\right) \left(1+\frac{V(t)^2}{U_\infty^2}\right) \tag{3.5}$$

$$C_D(t) = \left(\widetilde{C_D}(\alpha+\theta(t))\cos(\theta(t)) - \widetilde{C_L}(\alpha+\theta(t))\sin(\theta(t))\right) \left(1+\frac{V(t)^2}{U_\infty^2}\right) \tag{3.6}$$

The static force measurements were obtained from a gust-off angle-of-attack sweep at $Re = 20{,}000$. The results of this model can be compared to measured forces for

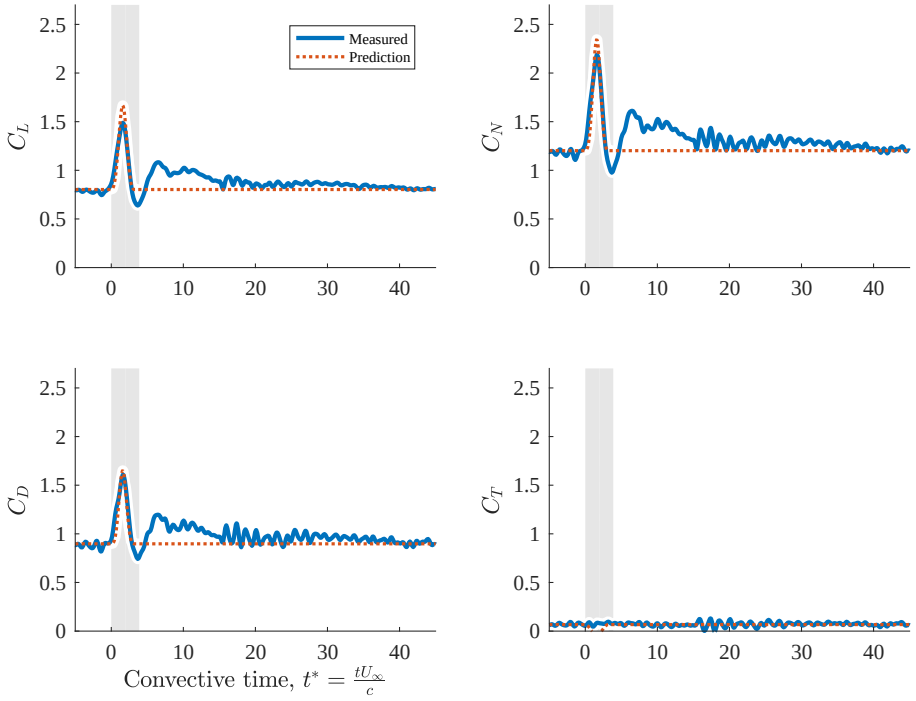

Figure 3.6: Quasi-steady gust force prediction based on static force data.

$\alpha = 45°$ and $G = 0.84$ in figure 3.6. The steady and peak forces are closely matched, but the gradual gust recovery is completely missed — as was anticipated due to the inherent limits of the quasi-steady model.

3.2.1 Adaptations of indicial theory

The transverse gust encounters studied here were intentionally significantly unsteady events. The lingering effects of the gust encounter over the roughly 30 chord-lengths after the wing has exited the gust indicates that the force production is (as expected) impacted by the flow history rather than just the instantaneous conditions. Because of this, unsteady aerodynamic models may better capture the gust encounter force production.

Indicial theory allows the impulse response of a system to be extended to model the response to arbitrary forcing by approximating that forcing as many small impulse changes. Küssner's function is the impulse response of a two-dimensional flat plate wing to an encounter with a small-perturbation sharp-edged gust. By using Duhamel's integral, the convolution of the impulse response with the slope of the arbitrary forcing, Küssner's function can be extended to spatially distributed gusts.

The typical application of Duhamel's integral and Küssner's function is based on thin-airfoil theory. The validity of this method for transient force production during high-amplitude gust encounters will be discussed below, but it is at least clear that thin-airfoil theory is not applicable during the steady-state conditions preceding the gust encounter. To proceed with this method, the steady-state force production must be made to match the separated flow conditions by substituting empirical results for the initial condition, $C_{N,\,\mathrm{static}}(t^* = 0)$. All three adaptations tested in the current work include this change. Note that in the small-perturbation scenarios for which thin-airfoil theory was derived, lift and plate-normal force are approximately equivalent, and the results are typically presented as lift. In the current work, normal force was chosen for these large-perturbation adaptations so that the thin-airfoil theory results approach the more reasonable solution $C_N(90^\circ) = 2\pi \sin(90^\circ) = 2\pi$ rather than $C_L(90^\circ) = 2\pi$ when the measured $C_L(90^\circ) = 0$.

The variations in the three present adaptations are contained in the unsteady term, in which the arbitrary forcing in Duhamel's integral is expressed in a manner that captures the aerodynamic response of the system, $C_{N,\,\mathrm{response}}$. This general form

of the indicial method using Küssner's function adapted for large gusts is therefore:

$$C_N(s) = C_{N,\,\text{static}}(0) + \int_0^s \left[\frac{\mathrm{d}}{\mathrm{d}\sigma} C_{N,\,\text{response}}(\sigma)\right] \psi(s-\sigma)\,\mathrm{d}\sigma \tag{3.7}$$

In this equation, $C_N(s)$ is the resulting unsteady normal force coefficient. As stated above, $C_{N,\,\text{static}}(0)$ is the empirical normal force coefficient measured at the same wing pitch angle, which is used here as the initial condition so that the models agree with the measured force histories before and after the gust encounter. $\psi(s-\sigma)$ is Küssner's function, which was derived for small-perturbation sharp-edged gusts, but is the closest available indicial response for the large-amplitude gusts of interest in the current work. $C_{N,\,\text{response}}(\sigma)$ is a placeholder which will be replaced by some function of the quasi-steady aerodynamic response of the wing. The independent variable here is $s = \frac{2tU_\infty}{c}$, the semi-convective time. The final variable, σ, is a bound variable for integration over all values of s in the flow history.

In the usual small-angle application of the indicial method for a gust response (see equation 1.12), the forcing, $C_{N,\,\text{response}}$, is expressed as in linearized thin airfoil theory, $C_N \approx C_L = 2\pi \sin(\theta)$ where $\theta = \alpha + \tan\left(\frac{V(t)}{U_\infty}\right)^{-1}$. This can be linearized by $\sin(\theta) \approx \theta$ and $\tan\left(\frac{V(t)}{U_\infty}\right)^{-1} \approx \frac{V(t)}{U_\infty}$. In the current work, a correction is incorporated for the finite aspect ratio of the test article: $\frac{\mathrm{d}C_L}{\mathrm{d}\alpha} = \frac{2\pi}{1+\frac{2}{\mathcal{AR}}} = \frac{4\pi}{3}$ [7]. This unsteady force production model will be referred to here as the linearized unsteady thin-airfoil model, or in figure legends as "linearized."

$$C_N(s) = C_{N,\,\text{static}}(0) + \frac{2\pi}{U_\infty\left(1+\frac{2}{\mathcal{AR}}\right)} \int_0^s \left[\frac{\mathrm{d}}{\mathrm{d}\sigma} V(\sigma)\right] \psi(s-\sigma)\,\mathrm{d}\sigma \tag{3.8}$$

Only one term of linearized thin-airfoil theory is not constant, so much of this model, $\frac{2\pi}{U_\infty\left(1+\frac{2}{\mathcal{AR}}\right)}$, can be moved outside of the integration. The unsteady aerodynamics here are expressed directly as a function of the gust velocity profile, $V(\sigma)$.

The use of linearized thin-airfoil theory is typical because the flat-wake assumption necessary for Küssner's function means that small-angle approximations are valid. However, the simplification of the general form which converted equation 3.7 into equation 3.8 does not need to be taken so far. By using thin airfoil theory without the linearizing small-angle approximations, the model can be applied to higher incidence angles (caused by higher gust ratios) without the additional error introduced by linearizing. Those same high incidence cases violate the flat-wake and attached flow assumptions built into Küssner's function, but this is true of each model described here. If the quasi-steady aerodynamic response of the system is modeled using thin-airfoil theory without the small-angle approximations, the resulting equation is:

$$C_N(s) = C_{N,\,\text{static}}(0) + \frac{2\pi}{1+\frac{2}{\mathcal{AR}}} \int_0^s \left[\frac{\mathrm{d}}{\mathrm{d}\sigma} \sin\left(\alpha + \tan\left(\frac{V(\sigma)}{U_\infty} \right)^{-1} \right) \right] \psi(s-\sigma)\,\mathrm{d}\sigma \quad (3.9)$$

As with equation 3.8, the constant parts of the lift-curve slope, $\frac{2\pi}{1+\frac{2}{\mathcal{AR}}}$, can be removed from the integration. In equation 3.9, however, much more remains in the unsteady term. The forcing function of Duhamel's integral in this case is not the gust velocity profile as before; the forcing is the sine of the effective flow incidence angle, $\sin\left(\alpha + \tan\left(\frac{V(\sigma)}{U_\infty} \right)^{-1} \right)$. While both the linear and non-linear versions of this model incorporate the initial conditions into $C_{N,\,\text{static}}(0)$, only the non-linear model

incorporates those conditions into the unsteady portion by depending on α. This unsteady force production model will be referred to here as the non-linear unsteady thin-airfoil model, or in figure legends as "non-linear."

The theoretical aerodynamics of thin-airfoil theory are not a required component of this indicial convolution method. The static force curve, $C_N \approx C_L = 2\pi \sin(\theta)$, can be replaced entirely by the empirical quasi-steady response. This adaptation incorporates the features of the static flow into the unsteady model, such as flow separation and the static force curve, $C_N(\theta)$. However, those features do not remain unchanged between the static and unsteady cases, so this model is still only an approximation of the unsteady behavior.

$$C_N(s) = C_{N,\,\text{static}}(0) + \int_0^s \left[\frac{\mathrm{d}}{\mathrm{d}\sigma} C_{N,\,\text{static}}(\sigma) \left(1 + \left(\frac{V(\sigma)}{U_\infty} \right)^2 \right) \right] \psi(s-\sigma)\,\mathrm{d}\sigma \qquad (3.10)$$

In equation 3.10, the quasi-steady aerodynamic response is represented by an empirical look-up table of force coefficients, $C_{N,\,\text{static}}(\sigma)$, and a relative variation in total dynamic pressure, $\left(1 + \left(\frac{V(\sigma)}{U_\infty} \right)^2 \right)$. This third unsteady force production model will be referred to here as the semi-empirical unsteady model, or in figure legends as "semi-empirical."

The force history predictions made by these models can be compared to measurements in figure 3.7. Each plot shows the force history for one gust encounter, which are grouped into columns by wing pitch angle, and into rows by gust ratio. Four models are compared to each measured force history: first the quasi-steady semi-empirical model, then the three adaptations of the indicial method. All of the

models predict force histories which are vaguely correct in magnitude and shape, although the quasi-steady model does not capture the gust recovery behavior, and each model is up to 50% off of the peak force magnitude in some of the cases.

The use of small-angle approximations causes the linearized and non-linear unsteady thin-airfoil models to predict similar results for low angles and gust ratios, and different results for higher angles and gust ratios. The non-linear unsteady thin-airfoil model most closely matches the results except for the highest gust ratio. In that case, the effective incidence angle passed plate-normal and peaked at $\alpha + \theta = 104^\circ$. The behavior of the non-linear unsteady model did not remotely match the measured results in that case. However, the unsteady semi-empirical model matched the measured results for the high gust-ratio case quite well. The quasi-steady semi-empirical model predicts the peak force production at the correct time in each case, while all of the indicial methods lag behind the measured behavior. The local minimum in force production as the wing exits the gust poses an interesting challenge for future work as it is not captured by any of the current models. In fact, each of the present models is inherently incapable of predicting that particular feature, since the unsteady models are all based on the indicial response given by Küssner's function which does not predict overshoot under any circumstances.

In the various gust encounters presented in figure 3.7, different models match most closely to the measured forces depending on the parameters. None of the models accurately capture the peak force for all of the six cases. Also, none of the models fully capture the gust recovery process, although the indicial methods mirror the overall behavior over a shorter time span.

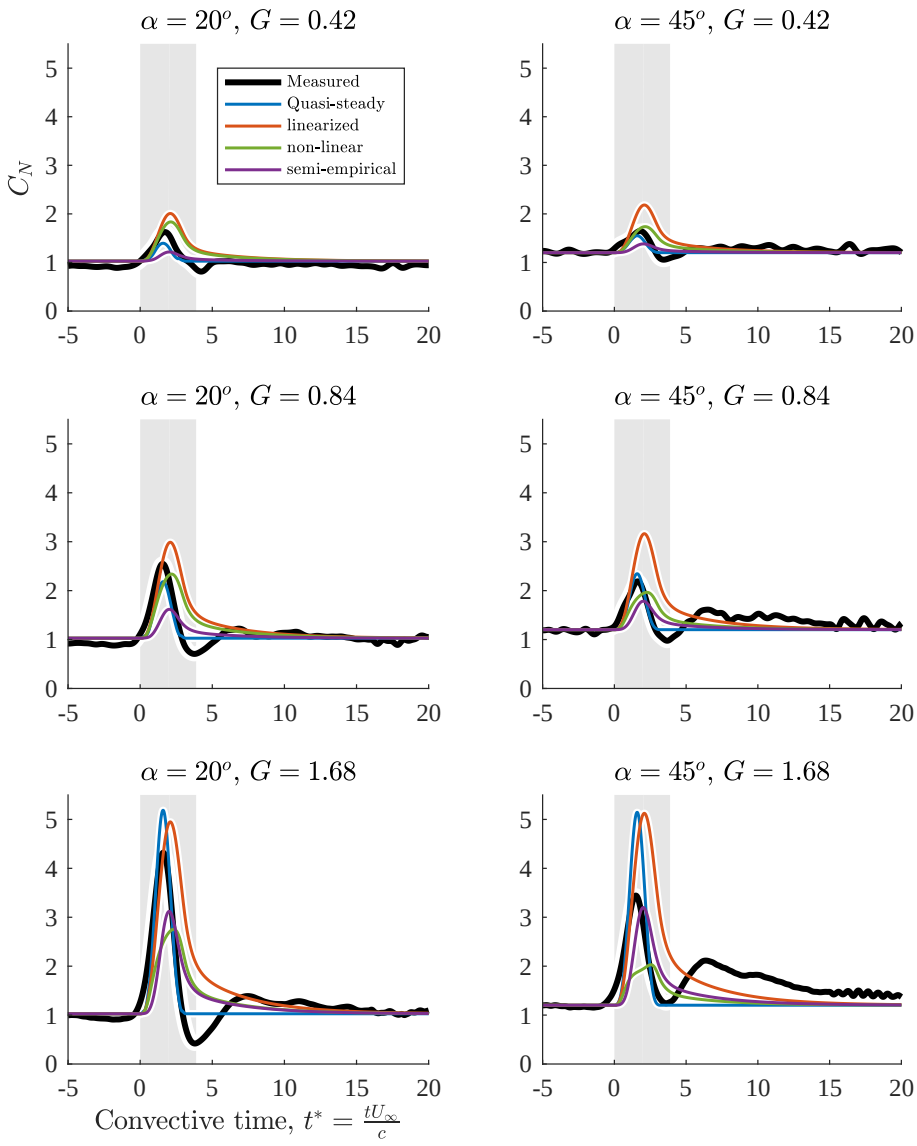

Figure 3.7: Comparison of measured to predicted normal force coefficients for six measurements and four models.

3.3 Variations in peak force production

The variations in force histories and predictions across the measured parameter space can be analyzed in a more quantitative manner if the data is reduced to a set of characteristic scalar quantities. Each of the 140 measured force histories was characterized by the peak values and steady values of lift and drag coefficients — or equivalently and interdependently: plate-normal and plate-tangent force coefficients. The steady forces in each case were taken as the mean force produced over the final 25 chord-lengths of constant towing velocity, $36 < t^* < 61$. The peak force in each case was taken as the maximum force measured during the gust encounter. To avoid exaggeration of maximum forces due to measurement noise, the force histories were smoothed using weighted quadratic local regression ("loess" in Matlab) with a span equal to half of the gust width before finding the peak value. The characteristic values of force coefficients are demonstrated in figure 3.8.

The steady forces after gust recovery are plotted in figure 3.9 as black circles. As expected, all of these measurements agree with the static angle-of-attack sweep data represented by the black line. These points have been plotted with some transparency so that the varying saturation of color can qualitatively indicate the overlap of repeated measurements.

The peak gust forces can be compared similarly by accounting for the increased total velocity and relative angle due to the gust. For a pitch angle, α, freestream velocity, U_∞, and gust velocity, V_g, the peak effective angle of attack and total

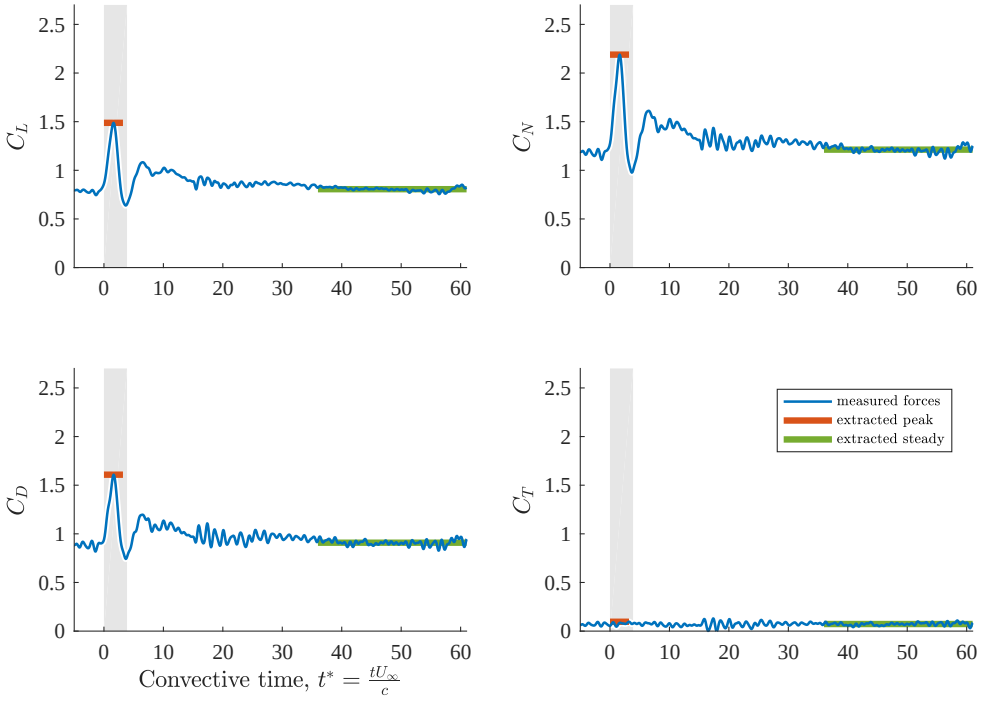

Figure 3.8: Each force history was reduced to a set of characteristic steady and peak forces.

velocity are:

$$\alpha_{\text{peak}} = \alpha + \tan\left(\frac{V_g}{U_\infty}\right)^{-1} \tag{3.11}$$

$$V_{\text{total}} = \sqrt{U_\infty^2 + V_g^2} \tag{3.12}$$

The peak forces are plotted at α_{peak} on the x-axis and normalized by V_{total}. The lift and drag coefficients are decomposed relative to α_{peak}. This is the reverse of the process used for the empirical quasi-steady model described in section 3.2. These re-normalized peak forces are plotted as diamonds colored by the associated gust ratio. Despite the rapid change of conditions around the wing during the gust encounter, the measured peak force coefficients were found to be close to the static measurements for a wide range of conditions.

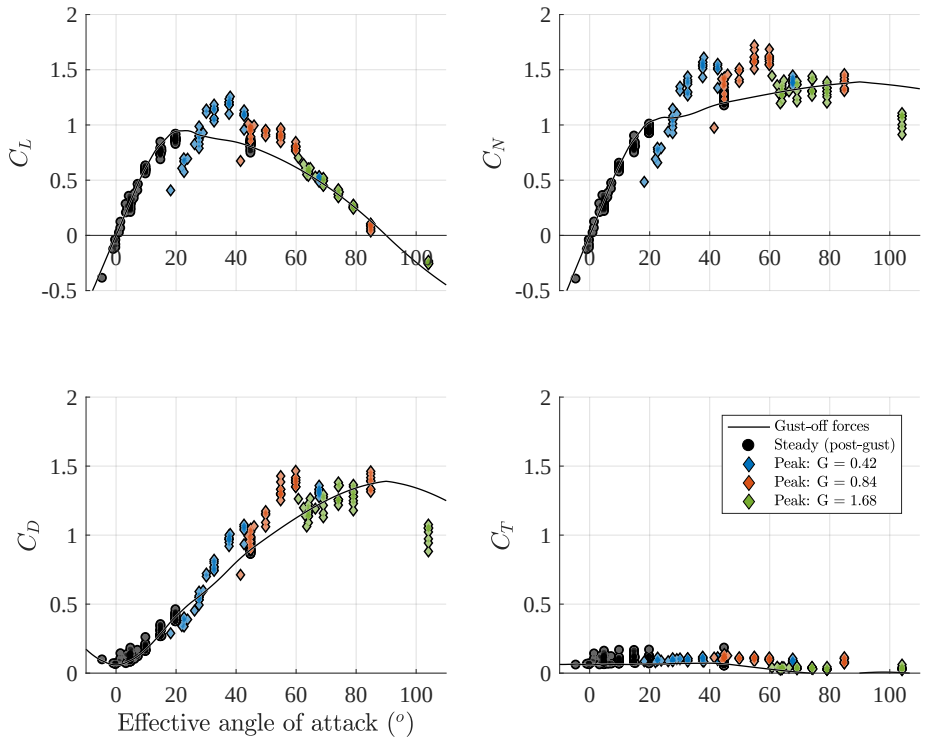

Figure 3.9: Quasi-steady analysis of peak unsteady gust forces.

It is apparent based on deviations between the steady and unsteady data (particularly in normal-force coefficient) that some unsteady effect is present that is not accounted for by the empirical quasi-steady analysis. The influence of unsteady effects is further observed by recalling the trend in peak forces in figure 3.4, which in disagreement with static data showed decreasing peak normal force coefficients with increasing angles of attack between 20° and 45°. This is visible in the C_N axis of figure 3.9 by noting that the right-most points of each color descend as the angle increases, but the black line that shows static force coefficient increases (if unevenly) for all angles up to $\alpha = 90°$.

The difference between the geometric pitch angle of the wing and the peak effective angle-of-attack during the gust is (non-linearly) proportional to the gust

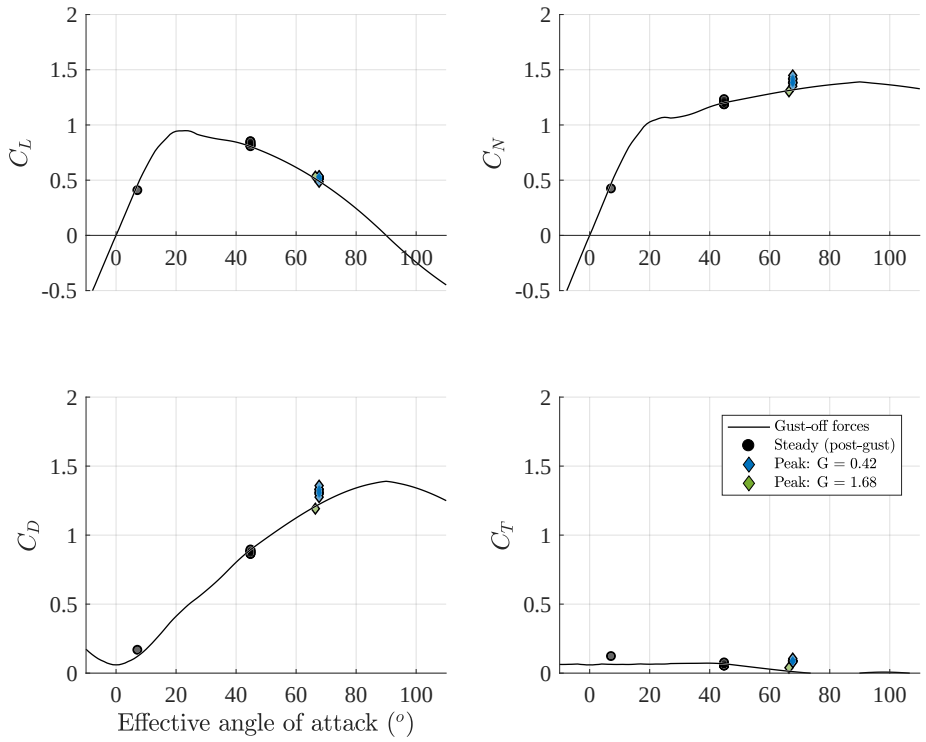

Figure 3.10: Convergence of peak forces for gust encounters with different initial conditions (a subset of the data from figure 3.9).

ratio. Cases with identical pitch angles, represented by overlapping black circles in figure 3.9, but different gust ratios result in different peak relative angles, represented by colored diamonds spread out across the x-axis. Several cases are particularly interesting; these cases have different pitch angles and gust ratios that cause the peak relative angles to coincide. Specifically, cases at $\alpha = 45^\circ$ with a gust ratio of 0.42 and $\alpha = 7^\circ$ with a gust ratio of 1.68 both result in a peak effective angle-of-attack within 1° of $\alpha_{\text{peak}} = 67^\circ$. It can be seen in figure 3.10 that the re-normalized peak lift and drag in these cases agree, suggesting that these forces depend on the peak quasi-steady conditions and not the pitch angle or gust ratio independently.

3.3.1 Unsteady analysis of peak force

The influence of unsteady aerodynamics on the peak forces can be investigated using the indicial models given by equations 3.8, 3.9, and 3.10. The peak normal forces predicted by the adaptations of Küssner's function were characterized and compared to the measurements using the same procedure shown in figure 3.8. Figure 3.11 shows these peak predicted values, although they are plotted differently than the measurements. The peak value for each indicial model is a function of only the initial pitch angle, the gust ratio, and the gust width. In the current work only one gust width was tested, so the remaining two-dimensional variation in peak force predictions was plotted as one line for each gust ratio (colored to match the measured results for each tested gust ratio).

The linearized unsteady thin-airfoil model (dotted lines) matches the magnitude of the forces well for each gust ratio, but does not capture the proper trends with respect to pitch angle. This is particularly visible for the highest gust-ratio cases (green), for which the measured peak forces decrease with increasing pitch angle but the predicted peak forces increase with increasing pitch angle.

The non-linear unsteady thin-airfoil model (solid lines) under-predicts the force magnitudes as the gust ratio increases, but matches the trend with respect to pitch angle very closely. If the results for the middle and higher gust ratio cases (red and green) were transposed upward by the appropriate amount, this model could fit very closely to the measured peak force for every case in the current work. This seems to indicate that the effect of flow incidence angle on peak force production is recreated

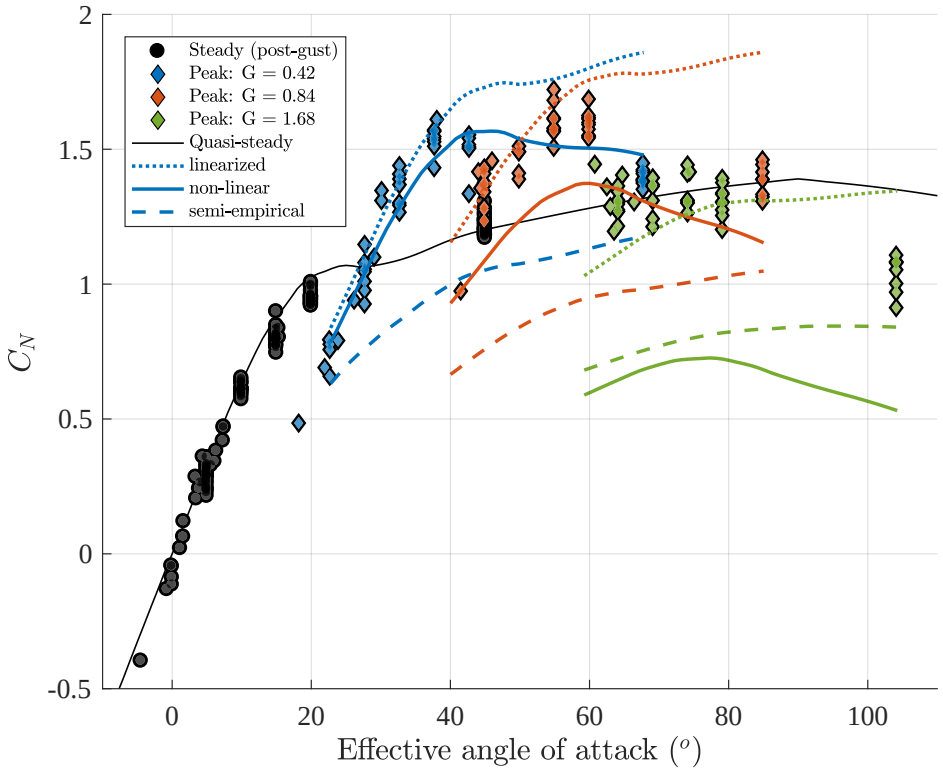

Figure 3.11: Adaptations of Kussner's function compared to measured peak normal force coefficients.

accurately by the non-linear unsteady thin-airfoil model, but that the effect of local dynamic pressure — which changes with gust ratio — is mis-characterized.

The unsteady semi-empirical model (dashed lines) does not match the magnitudes or the trends of the measured peak forces. This model seems to under-predict the increase in lift due to both the flow incidence angle and the local dynamic pressure. The under-prediction with respect to flow incidence angle in particular supports the interpretation that the unsteady force production is better modeled by the attached flow of theoretical aerodynamics rather than the separated flow of the static data.

3.4 Chapter summary

In this chapter, measured forces were presented and analyzed for sine-squared transverse gust encounters of width $w = 3.2c$, gust ratios $G = [0.42, 0.84, 1.68]$, and wing pitch angles between $-4^\circ \leq \alpha \leq 45^\circ$. These gust encounters created large transient forces which were observed to coincide with vortex formation at the leading edge during augmented lift and at the trailing edge during reduced lift.

The magnitudes of the peak forces were compared to predictions made using a quasi-steady empirical model and large-perturbation adaptations of indicial theory using Küssner's function. The peak predicted forces did not perfectly agree with measurements for any of the available models, but the general magnitude was matched by the quasi-steady empirical model and the linearized unsteady thin-airfoil model. The shape of the force trend with respect to pitch angle within each gust ratio was matched very closely by the predictions of indicial theory using the non-linear unsteady thin-airfoil model.

Chapter 4: Plunging wing force production

This chapter presents the measured force production by a thin, flat, rectangular wing performing single plunging maneuvers. These results serve to test aerodynamic models which do not rely on the harmonic nature of those in previous studies. The maneuvers vary in horizontal and vertical extent, duration, and wing pitch angle. The details of the tested parameter matrix are presented in section 2.5.

The force production during these plunge maneuvers was measured and qualitative trends with respect to each of the independent parameters are discussed. A data reduction procedure was then used to identify quantitative trends in force production across multiple axes of the parameter space. Additionally, force production was compared between the plunge maneuvers and the transverse gust encounters.

4.1 Plunging wing force history features

Figure 4.1 shows the force coefficient histories for four differently-shaped plunge maneuvers. The forces produced in each case are presented as lift and drag coefficient normalized first by the freestream dynamic pressure and then by the mean plunge

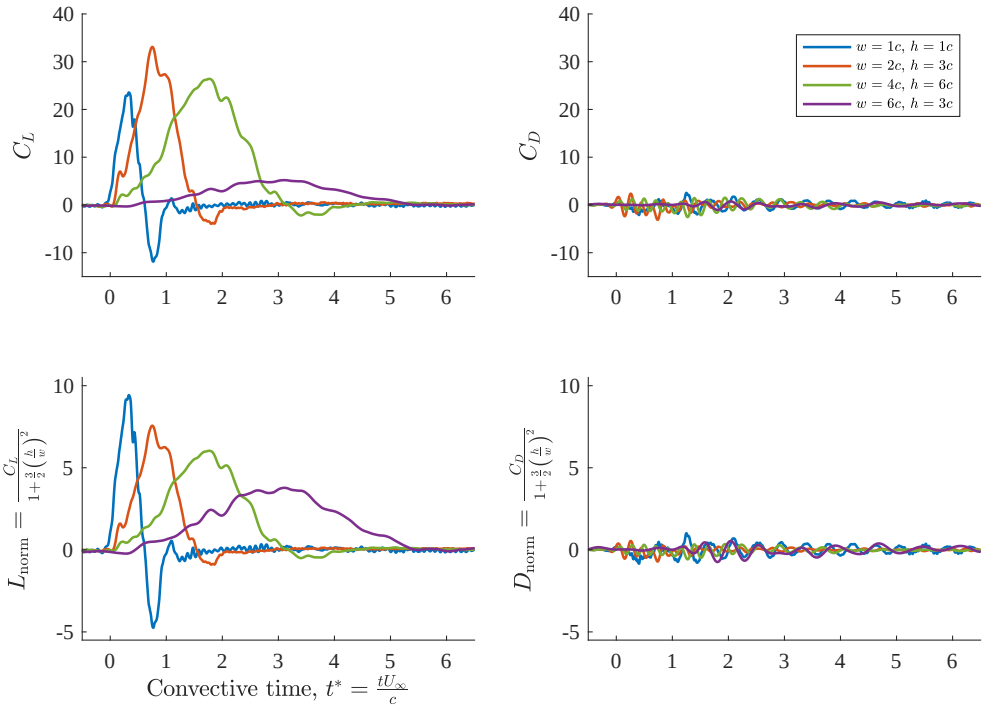

Figure 4.1: Example measurements of lift coefficient during the plunge maneuvers. In each case, $\alpha = 0°$.

kinetic energy (see section 2.6.3):

$$C_L = \frac{L}{\frac{1}{2}U_\infty^2 \rho S} \tag{4.1}$$

$$L_{\text{norm}} = \frac{L}{\frac{1}{2}\left(U_\infty^2 + \frac{3}{8}V_p^2\right)\rho S} = \frac{C_L}{1 + \frac{3}{2}\left(\frac{h}{w}\right)^2} \tag{4.2}$$

There are several striking features of these force histories. First, the magnitude of the lift coefficients is unreasonably high; it is important to keep in mind that this is an artifact of the freestream-dynamic-pressure method of normalization rather than a true indication of lift efficiency. The mean-kinetic-energy normalization attempts

to correct this, although the magnitudes of the coefficients are still high. Second, the force histories vary substantially in shape, even though the wing kinematics are all variations of the same shape. This supports the expectation that multiple physical sources of force production are involved. Third, as was also observed for this flat plate wing in the gust, force production is dominated by plate-normal pressure forces. Plate-tangent skin friction forces are negligible. The wing pitch angle in each case shown here is 0°, so the lift is equivalent to the plate-normal force and the drag is equivalent to the tangent force. Those components will be discussed separately for cases with pitch angles above zero. Finally — and most surprisingly — there is very little unsteady force production after the plunge maneuver has ended. Unlike the extremely long recovery process from the gust encounters, the wing appears to return to steady force production within one chord-length traveled. This suggests that quasi-steady analysis may be a reasonable approach despite the large unsteadiness of the plunge maneuver itself.

The plunge maneuver kinematics associated with the cases displayed in figure 4.1 vary in both width and height, and no clear trend in force production with respect to kinematics is visible from this data. Of these four cases, the largest peak lift coefficient is observed during different kinematics depending on the normalization method: the highest C_L in figure 4.1 is 33 in the $w = 2c$, $h = 3c$ case, but the highest L_{norm} is 9.4 in the $w = 1c$, $h = 1c$ case. This is because the mean-kinetic-energy normalization incorporates the plunge velocity component, which suitably reduces the normalized forces for cases which have high a plunge velocity ratio. The lowest lift coefficient is observed for the same kinematics in each normalization, $w = 6c$ and

$h = 3c$.

4.2 Trends with respect to plunge kinematics

To understand how the variations in force production are related to variations in each of the plunge maneuver parameters, comparisons will be made between force histories measured for cases which vary in only one of these parameters at a time. It is also useful to identify how these maneuver parameters affect the primary physical quantities associated with force production: acceleration and dynamic pressure. The plunge maneuver kinematic used in all cases of the current study was the sine-squared gust profile:

$$V(t) = V_p \sin\left(\frac{\pi t}{T}\right)^2 \quad \text{for} \quad 0 \leq t \leq T \tag{4.3}$$

This can be rewritten based on the distances traveled during the maneuver, $h = \frac{1}{2}V_p T$ and $w = U_\infty T$, as:

$$V(t) = \frac{2hU_\infty}{w} \sin\left(\frac{\pi t U_\infty}{w}\right)^2 \tag{4.4}$$

The plunge acceleration during the maneuver can then be written as:

$$\dot{V}(t) = \frac{4hU_\infty^2}{w^2} \sin\left(\frac{\pi t U_\infty}{w}\right) \cos\left(\frac{\pi t U_\infty}{w}\right) \tag{4.5}$$

The horizontal velocity, U_∞, is constant, so it does not contribute to the acceleration. The freestream velocity does contribute to the peak dynamic pressure, though:

$$\frac{1}{2}\rho U_{\max}^2 = \frac{1}{2}\rho \left[U_\infty^2 + \left(\frac{2hU_\infty}{w}\right)^2\right] = \frac{1}{2}\rho U_\infty^2 \left[1 + \left(\frac{2h}{w}\right)^2\right] \tag{4.6}$$

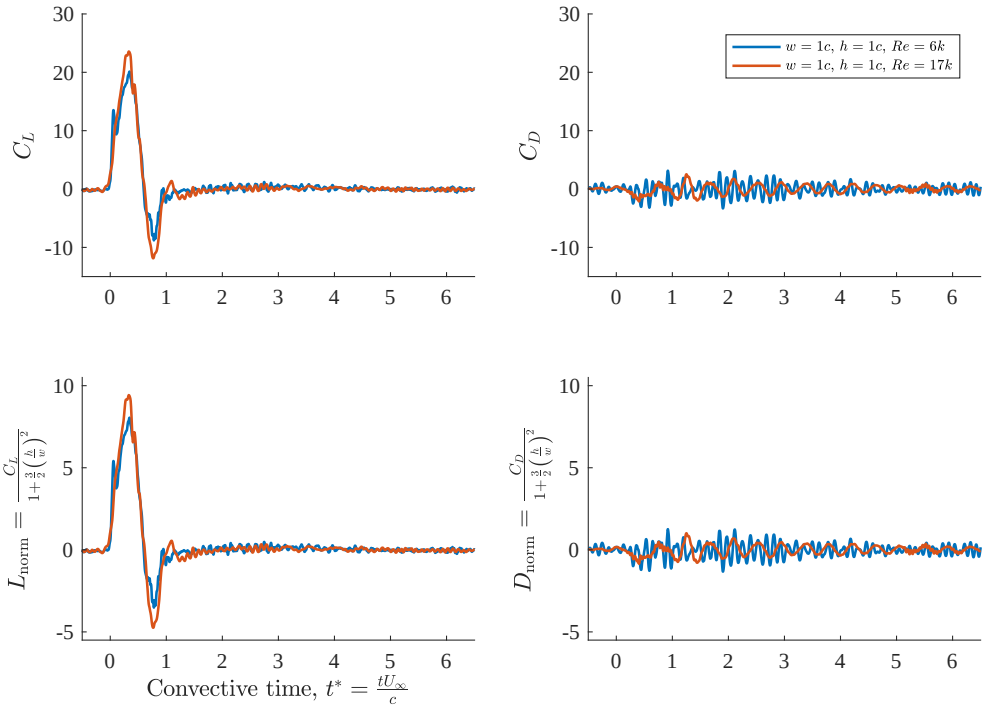

Figure 4.2: Measurements of forces during plunge maneuvers which vary only in freestream Reynolds number.

The proportional variations of acceleration and dynamic pressure with respect to each of the maneuver parameters, h, w, and U_∞, will help to decipher the observed effects that each of these parameters has on the measured force production.

4.2.1 Effects of varying Reynolds number

Figure 4.2 shows lift coefficient histories for cases which vary only in Reynolds number, which determines the freestream velocity and thus also the maneuver duration. Both the peak acceleration experienced by the wing and the peak dynamic pressure increase proportionally with the square of the freestream velocity. This proportionality is precisely why lift coefficient is typically normalized by freestream

dynamic pressure, and as seen here the normalized forces are not changed by the varied Reynolds number.

Figure 4.2 only shows the comparison for the $w = 1c$, $h = 1c$ case, but each other set of cases which only varied by Reynolds number also resulted in matching force coefficients. This is true for both C_L and L_{norm}, since the difference between these normalizations does not vary with Reynolds number. These results agree with previous conclusions that force production by thin flat plates is insensitive to Reynolds number [27]. This result is useful primarily in reducing the parameter space to the more manageable size of three independent parameters, and for allowing comparisons of maneuvers with different Reynolds numbers.

4.2.2 Effects of varying plunge height

The peak acceleration of the wing increases linearly proportionally with the maneuver height. The variation in peak dynamic pressure with respect to maneuver height is more complex since it depends on both the horizontal and vertical velocities. This is displayed in figure 4.3. The peak dynamic pressure normalized by the freestream dynamic pressure is shown in blue on a logarithmic plot. The contribution to peak dynamic pressure by the vertical velocity, shown in red, increases proportionally with the square of the maneuver height. The contribution by the horizontal velocity, shown in green, does not increase at all. This causes the variation in peak dynamic pressure with respect to plunge height, $\frac{\mathrm{d}}{\mathrm{d}h}(q_{\max})$, to approach quadratic for high velocity ratios, but to fall below the quadratic variation for lower

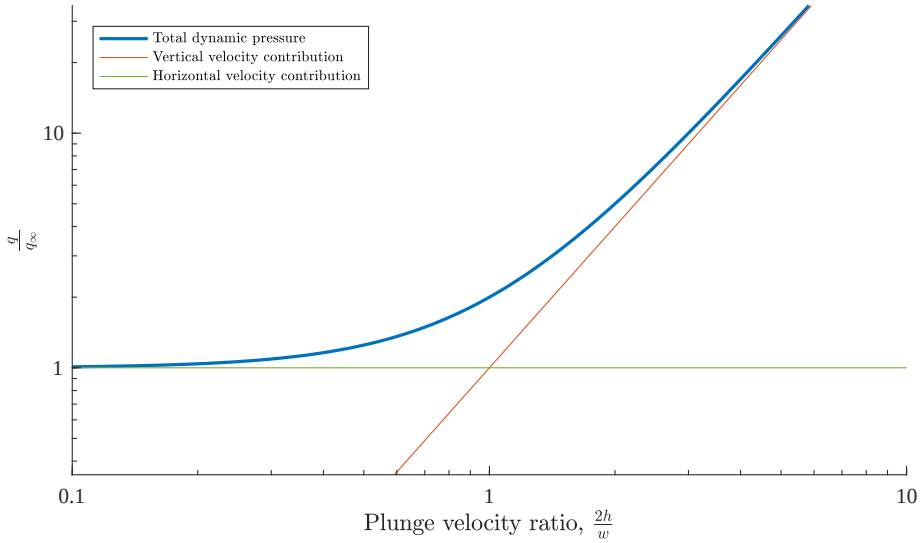

Figure 4.3: Variations in dynamic pressure contributions by U_∞ and V_p with respect to plunge velocity ratio.

velocity ratios.

Figure 4.4 shows force coefficient histories for cases which vary in plunge maneuver height. These cases also vary in freestream Reynolds number (they were defined so that the peak velocity matched instead), but it was shown in the previous section that variations in Reynolds number did not change the normalized force histories. The lift coefficient axis (top left) of figure 4.4 clearly shows that increasing the plunge height increases the normalized force production. The increased plunge height (when the width is fixed) corresponds to an increase in the relative contribution of the vertical velocity component compared to the horizontal velocity. The normalization of forces by freestream dynamic pressure does not account for this, so the normalized force is bound to increase. Interestingly, the mean-kinetic-energy lift normalization collapses four of the six curves, which means that the variation in force production with respect to plunge depth is proportional to the variation in

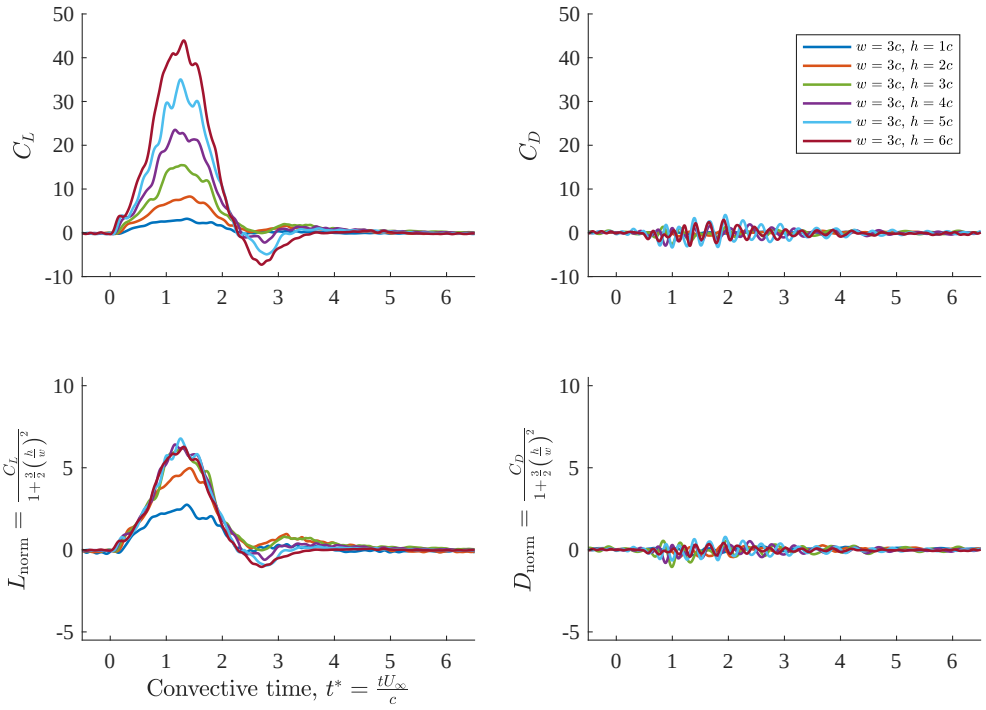

Figure 4.4: Measurements of forces during plunge maneuvers which vary in height but not width.

mean kinetic energy for these cases. The two lowest-amplitude cases fall below the trend. This is related to the discussion of variations in peak dynamic pressure with respect to plunge height, since the freestream dynamic pressure and the mean kinetic energy are related by a similar nearly-quadratic term (see section 2.6.3): $1 + \frac{3}{2}\left(\frac{h}{w}\right)^2$. For the four higher velocity ratio cases here, $\frac{V_p}{U_\infty} = \frac{2h}{w} >= 2$, and so the variations in both the peak dynamic pressure and the mean kinetic energy begin to converge to the same quadratic trend.

4.2.3 Effects of varying plunge width

The peak acceleration of the wing increases proportionally with the inverse square of the maneuver width: $\propto \frac{1}{w^2}$. A wing in a wider plunge maneuver experiences less acceleration — as long as the height is fixed. The peak dynamic pressure has a similar (but inverse) behavior with respect to plunge width to that which it had with respect to plunge height. The relative contribution of peak dynamic pressure by the horizontal velocity increases proportionally with the square of the maneuver width, but the contribution by the vertical velocity does not increase at all. In terms of equation 4.6, the peak dynamic pressure approaches the freestream dynamic pressure for very wide maneuvers, and is higher than the freestream dynamic pressure for narrower maneuvers.

Figure 4.5 shows force coefficient histories for cases which vary in plunge maneuver width (and Reynolds number, but as previously discussed, this did not affect the force coefficients). This figure is a good demonstration of the weakness of the typical lift coefficient normalization by freestream dynamic pressure. The first case plotted here peaks at $C_L \approx 120$ and so had to be truncated so that the other five cases would be visually discernible. This amplitude difference is primarily caused by the relative magnitudes of the vertical and horizontal velocity components, and so that difference is minimized by the mean-kinetic-energy lift normalization. In both plots, it is clear that the peak normalized lift decreases with increasing maneuver width, as do both the peak acceleration and dynamic pressures experienced by the wing during the maneuver. As is particularly apparent in figure 4.5, it is difficult to

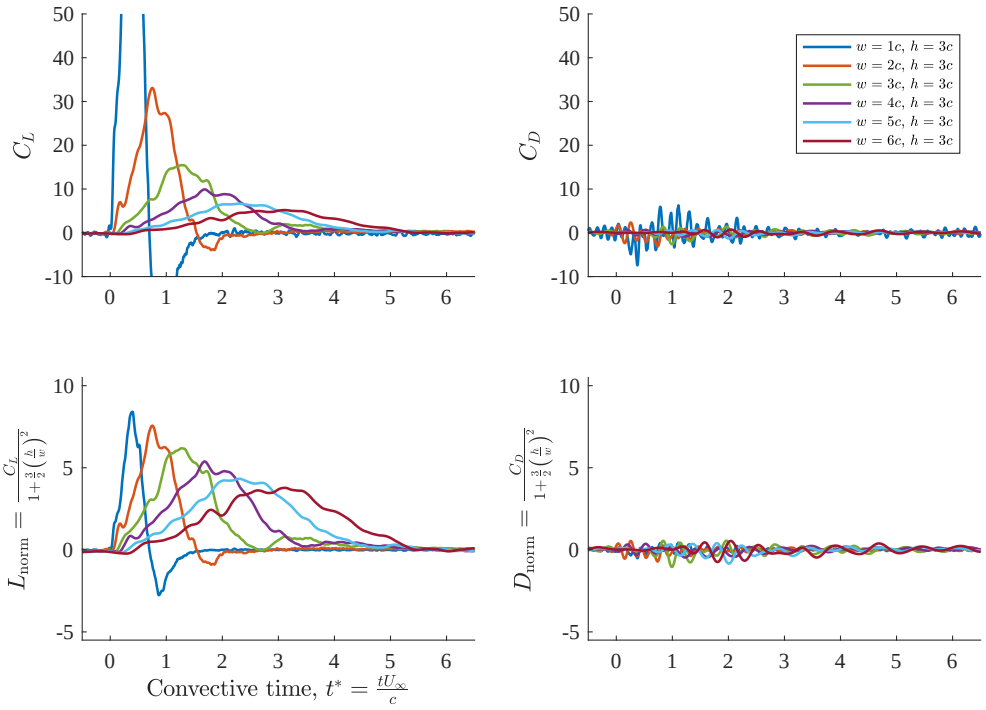

Figure 4.5: Measurements of forces during plunge maneuvers which vary in width but not height.

say quantitatively how the magnitudes of these force histories vary because they also vary significantly in overall shape. This is addressed below in section 4.3.1 in order to better quantify the trends in force production with respect to plunge maneuver height and width.

4.2.4 Effects of varying wing pitch angle

The geometric pitch angle of the wing does not appear in the kinematic equations for either acceleration (equation 4.5) or dynamic pressure (equation 4.6), which were suggested to be the key contributors to force production. However, the variation in force production with respect to acceleration and dynamic pressure are

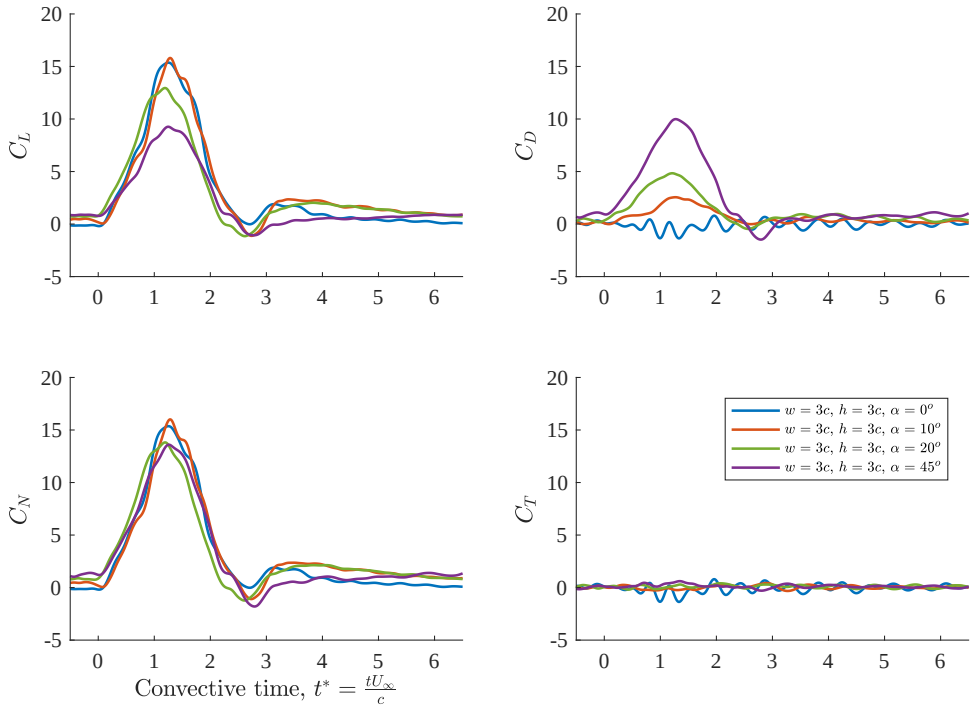

Figure 4.6: Measurements of forces during plunge maneuvers which vary in wing pitch angle but not width or height.

dependent on other quantities as well. Some of these, such as fluid density, ρ, and wing planform area, S, were not varied in the current work. The wing pitch angle, α, was varied here in order to inspect its effects on unsteady force production. During the plunge maneuver, the relative incidence angle of the fluid is the sum of the wing pitch angle and the angle of the velocity vector of the wing, $\alpha + \tan\left(\frac{V(t)}{U_\infty}\right)^{-1}$.

Figure 4.6 shows force coefficient histories for cases which vary in wing pitch angle, but are otherwise the same maneuver kinematics. These $\alpha \neq 0°$ cases separate the lift from the normal force, and so further verify that the force production is primarily plate-normal. Somewhat surprisingly, each of the four plotted cases produced nearly the same normal force histories. The lift and drag projections of normal force change with pitch angle, but the plate-normal forces are not significantly

affected by the wing pitch angle for the tested range, $0^\circ \leq \alpha \leq 45^\circ$.

In these example cases, the plunge maneuver increases the flow incidence angle by $\tan\left(\frac{2h}{w}\right)^{-1} = 63^\circ$ at the peak. It should be expected then that the case which began at $\alpha = 0^\circ$ and increased to $\alpha + \theta = 63^\circ$ would produce different transient forces than that which began at $\alpha = 45^\circ$ and increased to $\alpha + \theta = 108^\circ$. The change in quasi-steady force production, $\frac{\mathrm{d}C_N}{\mathrm{d}\alpha}$, certainly varies between these two ranges (as shown in figure 2.4). Instead, it was observed that these cases — and those for wing pitch angles in between — resulted in similar force histories. This suggests that the initial pitch angle has very little impact on the overall transient force slope, $\frac{\mathrm{d}C_N}{\mathrm{d}\theta}$, although the mechanism behind that behavior is unknown.

The initial pitch angle does impact the steady state normal force before and after the plunge, but this effect is negligible in figure 4.6 due to the relative magnitude of the steady and unsteady force contributions. Even in these moderate plunge cases ($w = 3c$, $h = 3c$) the peak force coefficients during the maneuver reach $C_N \approx 15$, which is much greater than any normal force coefficient measured outside of the maneuver. The steady-state normal force coefficient at the highest angle tested here, $\alpha = 45^\circ$, was $C_N = 1.2$, only 8% of the peak observed value in figure 4.6.

It can be seen from equation 1.6 that the inertial component of unsteady forces should also vary with respect to wing pitch angle. That equation can be simplified for the current maneuver to show inertial normal force due to plunge acceleration:

$$C_{N,\,\mathrm{inertial}} = -\frac{\pi c}{2U_\infty^2}\dot{V}\cos(\alpha) \tag{4.7}$$

This potential flow model indicates that the normal force production is proportional to the chord-normal projection of the acceleration, $\dot{V}\cos(\alpha)$, which depends on wing pitch angle. This can be reconciled with the observed force histories by recognizing that both the relative change in $\cos(\alpha)$ and the magnitude of inertial forces are small compared to the peak observed forces. The chord-normal component of plunge acceleration is 100% at $\alpha = 0°$, 98% at $\alpha = 10°$, 94% at $\alpha = 20°$, and 71% at $\alpha = 45°$. Therefore, in figure 4.6, only the case at $\alpha = 45°$ experiences a significantly different chord-normal acceleration from the others, although even in this case there is no clear difference in observed force production. Equation 4.7 predicts that the peak added-mass force for $w = 3c$, $h = 3c$, $\alpha = 0°$ is $C_{N,\,\text{inertial}} = 3.3$, which is only 22% of the observed peak force. Assuming for the moment that this model accurately represents the inertial force production of the plunging wing, the non-inertial forces are far greater than the inertial forces in figure 4.6. This can be qualitatively corroborated by observing the high force production at $t^* = 1.5$, since at that moment the plunge acceleration is $\dot{V} = 0$ and so no inertial force is expected. Since the magnitudes of the steady and inertial forces are small compared to the total unsteady force, their known variations with respect to wing pitch angle does not necessarily contradict the observed lack of variation in total force.

Figure 4.6 only shows cases for which $w = 3c$, $h = 3c$, but these results held for other plunge kinematics as long as the steady-state forces were small compared to the unsteady forces. The normal force histories of each tested maneuver size (for which α was varied) are shown in figure 4.7.

The variations in steady-state force production are only easily apparent in the

Table 4.1: Peak steady normal force coefficient (1.2) as a percent of peak observed force coefficient for plunge maneuvers in figure 4.7.

$\frac{C_{N,\,\text{steady}}}{C_{N,\,\text{peak}}}$	$w = 1c$	$3c$	$6c$
$h = 1c$	5.7%	30%	60%
$3c$	0.92%	8.0%	22%
$6c$	0.32%	2.9%	9.2%

Table 4.2: Added-mass normal force coefficient as a percent of peak observed force coefficient for plunge maneuvers in figure 4.7.

$\frac{C_{N,\,\text{inertial}}}{C_{N,\,\text{peak}}}$	$w = 1c$	$3c$	$6c$
$h = 1c$	47%	27%	14%
$3c$	23%	22%	15%
$6c$	16%	16%	13%

three lowest velocity ratio cases (the top-right and adjacent plots). This observation is in agreement with the relative magnitudes of the steady and unsteady forces for these cases, shown in table 4.1. Only in those three cases were the unsteady forces low enough that the differences in steady-state force production due to wing pitch angles were not negligible. In all of the other five cases, the normal force histories were not significantly affected by changes in wing pitch angle.

Similarly, table 4.2 shows the relative magnitudes of the added-mass and total unsteady forces for these cases. Most of these cases are only slightly influenced by inertial forces. The top-left axis of figure 4.7 shows forces for the case of $w = 1c$, $h = 1c$, for which the potential flow model predicts that the added-mass force — which, according the model, ought to vary with respect to wing pitch angle — is the highest of these cases at 47% of the peak observed force. Despite this greater inertial contribution than in the $w = 3c$, $h = 3c$ case from figure 4.6, no obvious force variation with respect to wing pitch angle is visible.

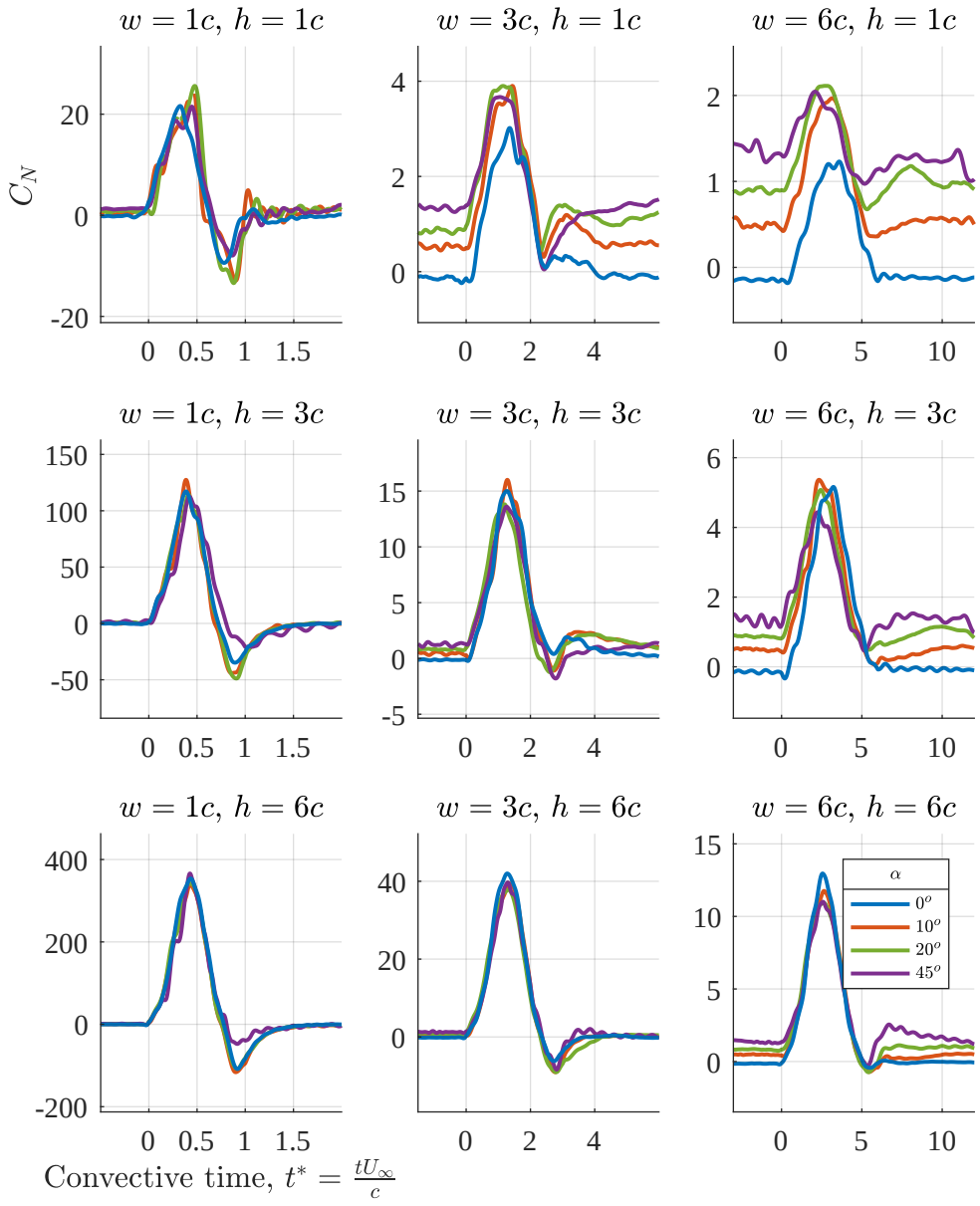

Figure 4.7: Measurements of normal force coefficient during several plunge maneuvers. Each axis shows a group which varies in wing pitch angle but not width or height. Note that the axes of each are scaled differently.

4.3 Force history characterization

As was done for the gust encounter data, plunge maneuver force production can be more usefully quantitatively analyzed if the force histories are reduced to a few characteristic scalars. This could be accomplished by extracting peak unsteady force production, but as is particularly evident in the L_{norm} axis of figure 4.5, the force production during the plunge maneuver has two constituent shapes which blend between the cases. In order to capture the behavior of these two separate components, the unsteady force production will be characterized by two scalars instead of one.

4.3.1 Two-term decomposition

As was noted above, force histories for these sine-squared plunge maneuvers seem to contain two distinct constituent shapes. Force histories for plunge maneuvers which are much taller than they are wide, $\frac{h}{w} \gg 1$, are mainly the shape of a sine wave. The shallower plunge cases, $\frac{h}{w} \ll 1$, result in force histories which are mainly a one-minus-cosine shape. Each force history can be modeled as the sum of these two shapes scaled by some coefficients, $\mathbb{C}_1$ and $\mathbb{C}_2$, and some residual, $\mathbb{R}$. While the wing is plunging ($0 \leq t^* \leq w$):

$$F_N(t^*) \approx \mathbb{C}_1 \left[1 - \cos\left(\frac{2\pi t^*}{w}\right)\right] + \mathbb{C}_2 \sin\left(\frac{2\pi t^*}{w}\right) + \mathbb{R} \tag{4.8}$$

The functions can be related back to the two primary sources of force production: acceleration and dynamic pressure. For the sine-squared kinematics of the current study, acceleration and dynamic pressure, given by equations 4.4 and 4.5, are these same two general shapes (the sine-squared plunge maneuver tested here is equivalent to one-minus-cosine by $1 - \cos(2\theta) = 2\sin(\theta)^2$). The resulting simplified model for normal force production, F_N, is then a scaled contribution from dynamic pressure plus another scaled contribution from acceleration. Any possible higher order effects are combined in the residual. This model can be fit to each measured force history by finding values for the coefficients which minimize the residual using least-squares regression. This general model is expressed in equation 4.9, and the shape of each term is isolated in equation 4.10. The latter equation was the one used for the least-squares curve fit.

$$F_N(t^*) = -\mathbb{C}_1 V(t^*)^2 - \mathbb{C}_2 \dot{V}(t^*) + \mathbb{R} \tag{4.9}$$

$$F_N(t^*) = \mathbb{C}_1 \sin\left(\frac{\pi t^*}{w}\right)^4 + \mathbb{C}_2 \sin\left(\frac{\pi t^*}{w}\right) \cos\left(\frac{\pi t^*}{w}\right) + \mathbb{R} \tag{4.10}$$

This equation was fit to each of the measured force histories to characterize them by the two coefficients, $\mathbb{C}_1$ and $\mathbb{C}_2$, and to quantify the minimum residual, $\mathbb{R}$. To avoid confusion, it is worth stating that the regression process was applied to the non-normalized force data (in Newtons), although each normalization option is a linear operation and so would not affect the outcome. The coefficients were normalized by either method after the force history characterization.

Figures 4.8 and 4.9 show examples of this decomposition model fit to measured force histories. Although the two example cases are very different, the model fits closely to each set of measured forces. The plunge maneuver which produced the forces in figure 4.8 was $1c$ in both width and height — an aggressive plunge maneuver. The coefficients normalized by mean kinetic energy were $\mathbb{C}_1 = 4.9$ and $\mathbb{C}_2 = 6.2$. In this case, the acceleration was responsible for slightly more force production than was the variation in dynamic pressure. The root-mean-square (rms) of the residual was 0.9, which is acceptably small compared to the two characteristic terms. The other example, shown in figure 4.9, was a much more gentle plunge maneuver of width $6c$ and height $3c$. The coefficients normalized by mean kinetic energy were $\mathbb{C}_1 = 4.0$ and $\mathbb{C}_2 = 0.1$. In this case, the acceleration was responsible for far less force production amplitude than the dynamic pressure. The rms of the residual was 0.4, which is again acceptably small even though $\mathbb{C}_2$ is also quite small in this case.

This process was repeated for each of the 108 measured plunge kinematics for which $\alpha = 0°$. In that way, the force production variations with respect to both maneuver width and height were quantified in terms of $\mathbb{C}_1$, $\mathbb{C}_2$, and $rms(\mathbb{R})$. Figure 4.10 shows those results — the same data is plotted in each axis, but it is displayed differently in each. The top row shows C_L and the bottom row shows L_{norm}. The left column is linearly scaled and the right column is logarithmically scaled (x-axis only). The x-axis for this figure is plunge maneuver aspect ratio, $\frac{h}{w}$, because it appeared as an important term in the equations for both the peak acceleration and peak dynamic pressure during each maneuver. It is visible (and unsurprising) that this parameter only incompletely captures the variation in plunging wing force production across

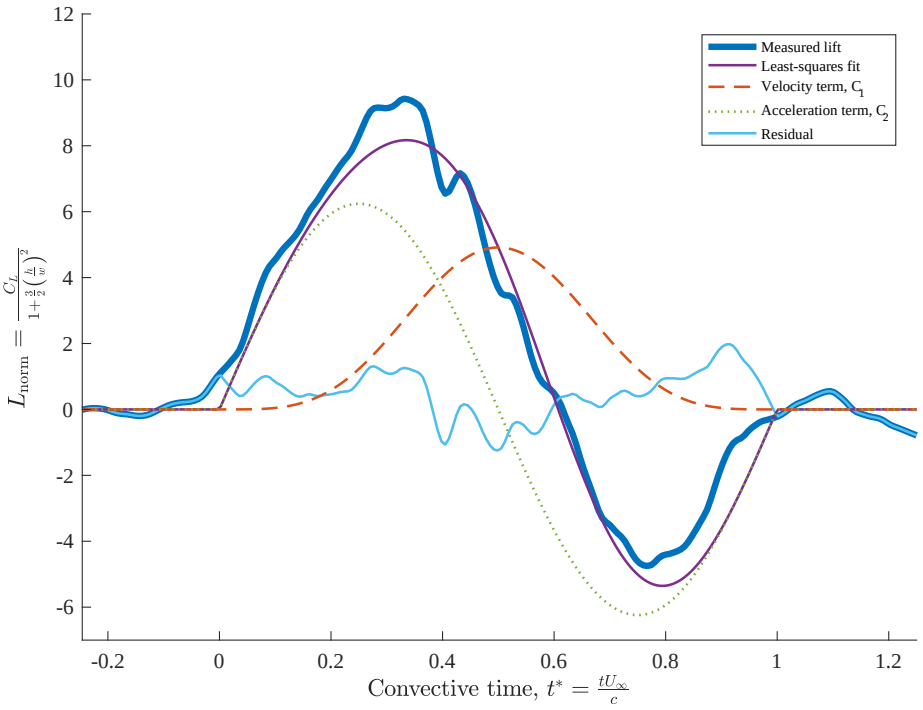

Figure 4.8: Best fit of the two-term lift decomposition for a high velocity ratio plunge maneuver: $w = 1c$, $h = 1c$.

the parameter space.

The linear axis of C_L (top left) shows that — at least for high aspect ratio, aggressive plunge maneuvers — both contributions to force production increase vaguely quadratically. This is corroborated by both the linear and logarithmic axes of L_{norm}, which shows that the mean-kinetic-energy-normalized force production is roughly constant for plunge maneuver aspect ratios above one. The roughly constant values of L_{norm} can be justified by the same proportionality to dynamic pressure that caused most of the data in figure 4.4 to converge for the mean-kinetic-energy normalization. The "banding" of smaller groups of data points within the overall trend — particularly visible in $\mathbb{C}_1$ on the logarithmic axis of L_{norm} (bottom right) — suggests that other parameter variations are also responsible for variations in plunge

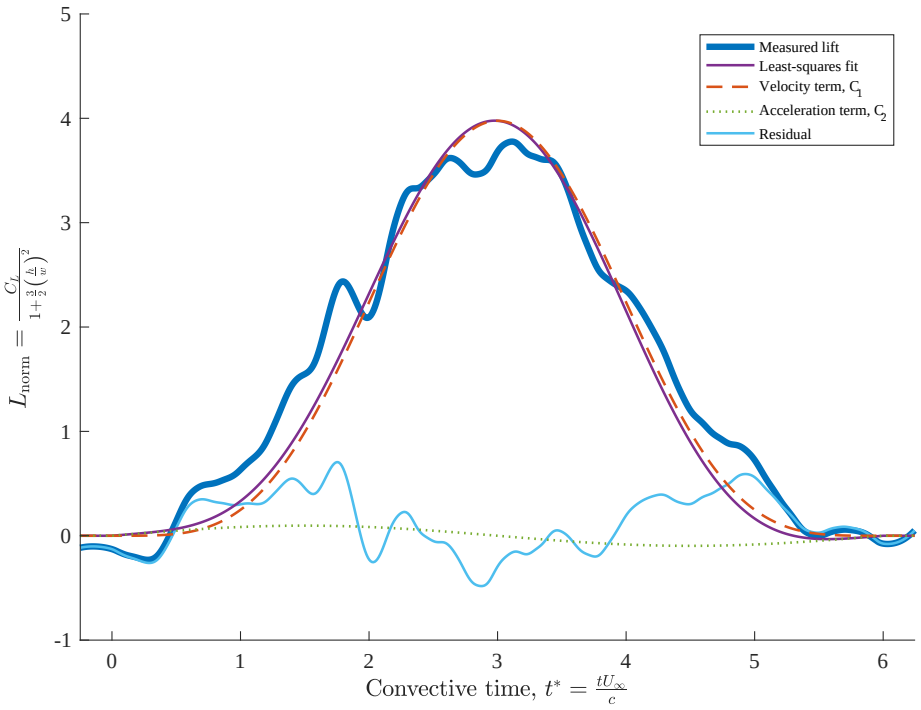

Figure 4.9: Best fit of the two-term lift decomposition for a low velocity ratio plunge maneuver: $w = 6c$, $h = 3c$.

force production. Additionally, it is clear that there are outliers in the $\mathbb{C}_2$ amplitudes using L_{norm} (at $\frac{h}{w} = 1$, there are $\mathbb{C}_2$ observations ranging from 2 to 13) which also indicates variations with respect to other plunge maneuver parameters. To identify more complete characterizations of these variations, the characteristic amplitudes can be compared to those predicted by various analytical models.

4.3.2 Comparison to analytical models

The small-perturbation solution for unsteady force production by a moving wing by von Kármán and Sears [18] divided total force production into three components: quasi-steady, inertial, and wake contributions (see section 1.2.4). The division of

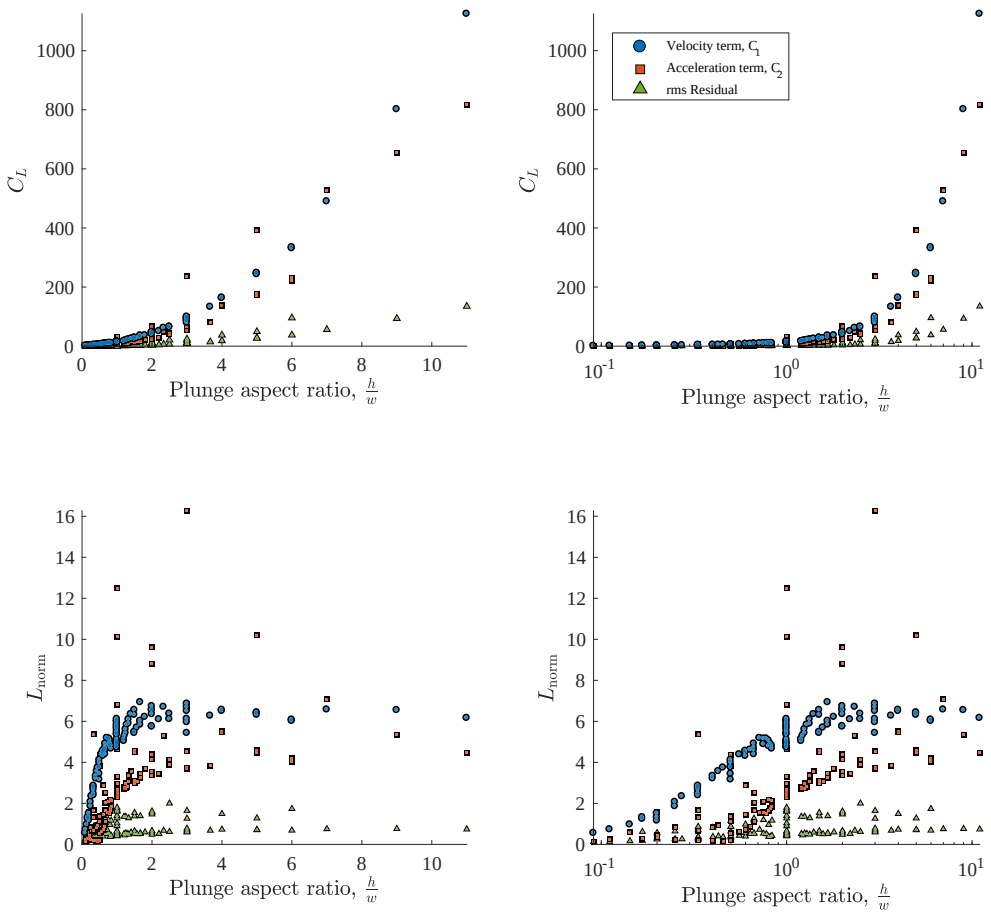

Figure 4.10: Magnitude of best-fit coefficients for each case. The top row shows C_L and the bottom row shows L_{norm}. The left column is linearly scaled and the right column is logarithmically scaled (x-axis only).

measured forces in the current study parallels the constituent parts of that analytical model.

The force production term for quasi-steady circulatory lift is associated with meeting the Kutta criteria under the instantaneous conditions. In the von Kármán and Sears model, this reduces to the simple thin-airfoil theory solution of $L = C_L \frac{1}{2}\rho U_\infty^2 S$ and $C_L = 2\pi \sin(\alpha)$. This contribution to force production varies

proportionally with dynamic pressure and with some expression of force coefficient and is therefore connected to the $\mathbb{C}_1$ component of the current decomposition. The small-angle approximations inherent in the analysis of von Kármán and Sears mean that $C_L \approx C_N$ and no distinction is made. For the larger perturbations of interest in the current work, these force orientations are distinct and the thin-airfoil theory solution may be more usefully posed as $C_N = 2\pi \sin(\alpha)$. Alternately, the equation for C_N may be altogether replaced by a look-up table based on empirical normal force coefficients measured under truly steady conditions, which would indirectly remove some of the flow assumptions (attached, inviscid flow for example) built into the thin-airfoil theory model.

The second term of von Kármán and Sears is the inertial force produced by "apparent mass," which is connected to the $\mathbb{C}_2$ component of the current decomposition. For small perturbations, this is represented by a potential flow solution of an accelerating flat plate, $C_N = \frac{\pi c \dot{V}_\perp}{2U_\infty^2}$. This solution has been used successfully in several studies of large, unsteady events despite the theoretical limitations of the inviscid flow model [26].

The third term of von Kármán and Sears is the lift deficiency due to wake vorticity. This term is not directly included in the current decomposition approach, although it is unreasonable — particularly for the aggressive plunge maneuvers — to assume that wake vorticity is insignificant. Some of this wake vorticity force production contribution will not match either of the decomposition's constituent shapes. This would be captured in the residual term, $\mathbb{R}$, which was relatively small for all cases measured in the current work. Alternately, some of this wake vorticity

force contribution will match the shape of the $\mathbb{C}_1$ or $\mathbb{C}_2$ terms. It is important to consider this wake vorticity force production term when comparing the observed and predicted amplitudes for each of the two directly included terms.

The coefficient $\mathbb{C}_1$ in the current model corresponds to the magnitude of forces produced by the relative fluid velocity and so can be compared to simple aerodynamic models such as thin-airfoil theory or a quasi-steady empirical method.

$$C_N(t) = \widetilde{C_N}(\alpha+\theta(t)) \left(1+\frac{V(t)^2}{U_\infty^2}\right) \tag{4.11}$$

where the tilde indicates quasi-steady quantities related to the total flow velocity rather than the pre-maneuver freestream velocity. The angle α is the geometric pitch of the wing relative to horizontal, while $\theta = \tan\left(\frac{V}{U_\infty}\right)^{-1}$ is the relative plunge velocity angle. Thin airfoil theory (with an aspect-ratio correction) predicts $\widetilde{C_N} = \frac{2\pi}{1+\frac{2}{AR}} \sin(\theta)$, while the empirical look-up method returns values from the static force data.

These equations represent the velocity-proportional force production, but do not share the exact form of $\mathbb{C}_1 V(t)^2$ which would be needed for a direct comparison to the decomposed measured forces. Both thin-airfoil theory and static data give values for $\widetilde{C_N}$ which vary as a function of $\theta(t)$. The predicted circulatory lift histories (for example, the orange line in figures 4.8 and 4.9) are not exactly sinusoidal, and so the peak value is not truly representative of $\mathbb{C}_1$. To facilitate the comparison between observed and predicted circulatory forces, the predicted force histories were also characterized by a least-squares fit of $\mathbb{C}_1 V(t)^2$ so that the $\mathbb{C}_1$ values from measurements and predictions could be directly compared in figure 4.11.

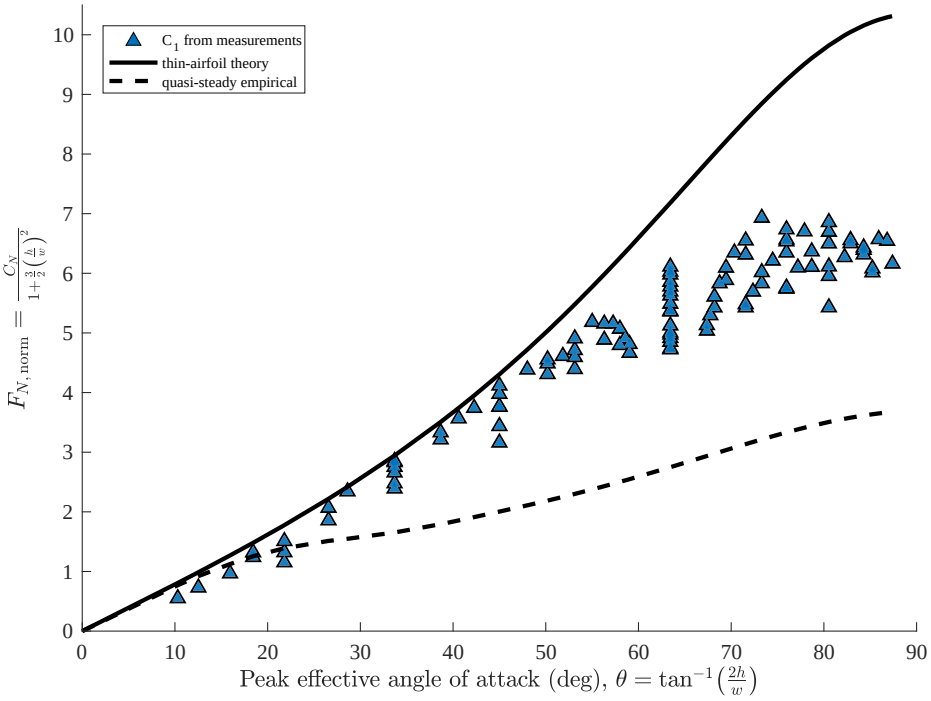

Figure 4.11: Comparison of measured and predicted lift for velocity-proportional $\mathbb{C}_1$ term

Figure 4.11 shows the $\mathbb{C}_1$ values from force measurements (blue triangles) normalized by mean kinetic energy and plotted as a function of peak effective angle of attack, $\theta = \tan\left(\frac{2h}{w}\right)^{-1}$. Variations in force production with respect to peak dynamic pressure are collapsed by the normalization, so the remaining variations are primarily a function of the plunge-velocity-induced flow incidence angle — or, in the case of the analytical models, exclusively so. Thin-airfoil theory, plotted as the solid line in figure 4.11, accurately predicts lift for gentle plunge maneuvers which reach peak effective angles of attack below 45°. The treatment of flow over the wing as inviscid and therefore attached leads to over-prediction of force production at excessively high peak incidence angles. Viscosity and flow separation can be indirectly incorporated into the aerodynamic model by using an empirical look-up table. The

results of this semi-empirical method are plotted as the dashed line in figure 4.11. In general, this model under-predicts the plunge maneuver lift production. The $\mathbb{C}_1$ values from measurements fall somewhere between these two predictions, suggesting that the wake vorticity effects — the here-unaccounted-for term from von Kármán and Sears — augment the transient lift but not as much as though the flow was entirely attached. As was the case in the model by Babinsky et al., the transient lift is more closely approximated by attached flow than by separated flow (equation 1.18). It is possible that the influence of a substantial leading edge vortex could justify use of the attached flow thin-airfoil theory results at angles well beyond stall [28].

The coefficient $\mathbb{C}_2$ represents the magnitude of forces produced by the fluid acceleration. The potential flow approximation of inertial forces in equation 1.6 applied to the sine-squared plunge maneuver at zero geometric angle of attack produces:

$$F_{\text{accel}} = \frac{\rho\pi^2 c^2 \text{Æ} h U_\infty^2}{w^2} \sin\left(\frac{\pi t^*}{w}\right) \cos\left(\frac{\pi t^*}{w}\right) \tag{4.12}$$

$$\therefore \quad \mathbb{C}_2 = \frac{2\pi^2 h}{w^2} \left(\frac{1}{2}\rho U_\infty^2 c^2 \text{Æ}\right) \tag{4.13}$$

This predicted amplitude can be easily compared to the $\mathbb{C}_2$ values from measurements. As before, figure 4.12 shows a scatter of the best-fit $\mathbb{C}_2$ from measurements plotted against an x-axis for which the available model collapses to a single line. In this case, that x-axis parameter is less intuitive; it is found by normalizing the prediction for added-mass force, equation 1.3, using the kinetic-energy method, equation 2.5. This step ensures that the model for predicting $\mathbb{C}_2$, equation 4.13, can be visualized

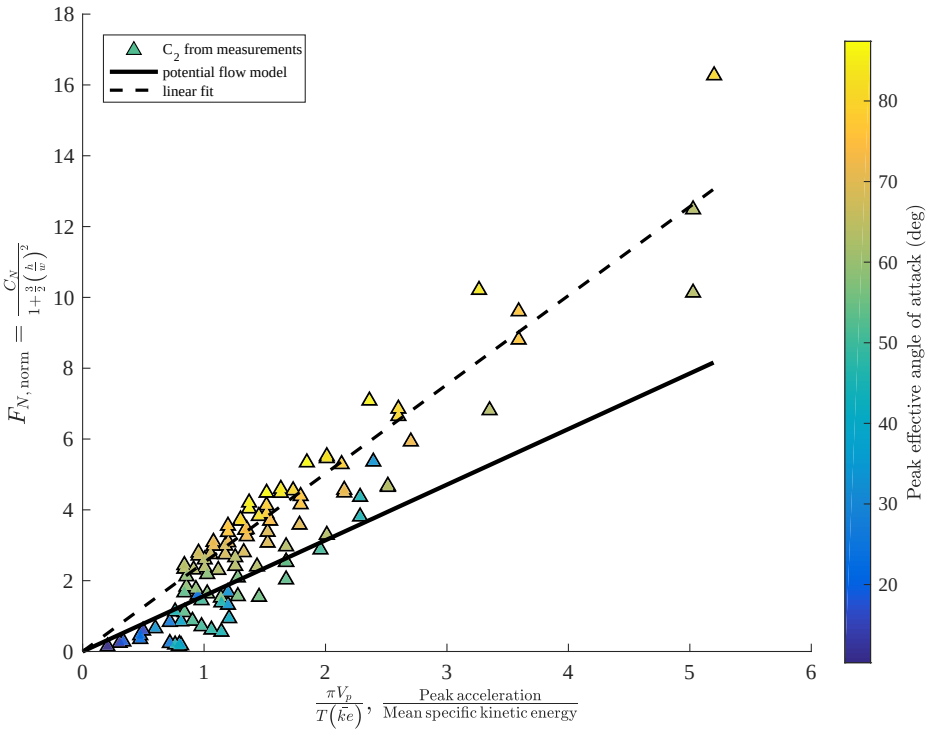

Figure 4.12: Comparison of measured and predicted lift for acceleration-proportional $\mathbb{C}_2$ term

as a single line in figure 4.12.

The potential flow model for added-mass, plotted as the solid line in figure 4.12, under-predicts the inertial force amplitudes, $\mathbb{C}_2$, that were extracted from the measurements in most cases. Interestingly, most cases were under-predicted by nearly the same factor, and so a semi-empirical model can be formulated which greatly improves the agreement between predictions and measurements:

$$\mathbb{C}_2' = 1.6\,\mathbb{C}_2 \tag{4.14}$$

This empirically tuned potential flow model is plotted as the dashed line in figure 4.12.

The color of each $\mathbb{C}_2$ point in figure 4.12 corresponds to the peak effective angle of attack reached during that maneuver. It is apparent that the points which agree with one or the other predicted line are grouped by this peak angle. Gentle plunge maneuvers which reached peak $\theta < 40^\circ$ are closer to the potential flow model while aggressive plunge maneuvers which reached peak $\theta > 50^\circ$ are closer to the linear fit. This trend indicates that some unsteady effect may be contributing to the $\mathbb{C}_2$ component of lift production. This increase in force production may also be attributed to wake vorticity, although the mechanism is less clear than in the interpretation of observed $\mathbb{C}_1$ magnitudes.

In combination, these terms form a model which accurately represents force production from somewhat low-amplitude sine-squared plunge maneuvers. The quasi-steady model based on thin-airfoil theory is:

$$C_N(t) = \frac{2\pi}{1+\frac{2}{AR}} \sin(\theta(t)) \left(1+\frac{V(t)^2}{U_\infty^2}\right) + \frac{\pi c \dot{V(t)}}{2U_\infty^2} \tag{4.15}$$

where again, $\theta(t) = \tan\left(\frac{V(t)}{U_\infty}\right)^{-1}$. Each term of this model matched the observed amplitudes for cases in which $\theta \leq 45^\circ$ (see figures 4.11 and 4.12). Cases in which $\theta > 45^\circ$ are over-predicted by the velocity-proportional term, $\mathbb{C}_1$, and under-predicted by the acceleration-proportional term, $\mathbb{C}_2$. The acceleration term can be seen to converge to a new value for those higher angles, and so in those cases it may be useful — if not physically insightful — to "tune" the model by scaling the $\mathbb{C}_2$ term by 1.6.

Additionally, the observations made in section 4.2.4 indicate that the wing

pitch angle has little effect on the unsteady force production for most cases tested in the current work. Although the effects of wing pitch angle on the unsteady force were observed to be negligible for most of the tested kinematics, those effects can still be incorporated into the model so that the steady-state predictions better match to measured forces and the inertial force term better matches to the potential flow model. The acceleration-proportional term of equation 4.15 can be made to match that of the potential flow added-mass model by scaling based on the plate-normal projection using a factor of $\cos(\alpha)$. The effects of the wing pitch angle on the velocity-proportional term of equation 4.15 only appeared to affect the steady-state forces, which can be represented by an additional term, $\widetilde{C_N}(\alpha)$. Each of these effects is small compared to the total unsteady force, but they are still included in the final model:

$$C_N(t) = \widetilde{C_N}(\alpha) + \frac{2\pi}{1+\frac{2}{AR}} \sin(\theta(t)) \left(1+\frac{V(t)^2}{U_\infty^2}\right) + \frac{\pi c \dot{V(t)}}{2U_\infty^2} \cos(\alpha) \tag{4.16}$$

This model presents the normal-force coefficient resulting from a sine-squared profile plunge maneuver as the sum of three parts: the empirical steady-state coefficient due to the wing pitch angle, the transient circulatory force linked to the leading edge vortex, and the non-circulatory inertial force. This is a semi-empirical quasi-steady model which was made to match unsteady force production by strictly limiting the plunge maneuver to sine-squared kinematics. Note that the inertial component of the force coefficient is a function of wing chord, c, which indicates that the relative contribution of inertial and circulatory forces do not scale equally. For geometrically-

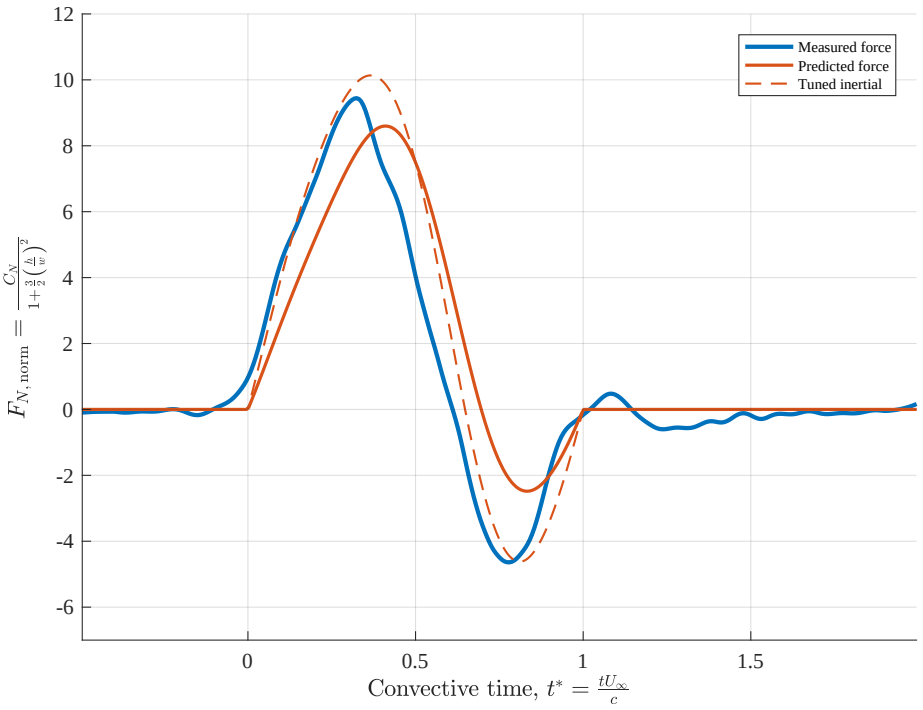

Figure 4.13: Comparison of measured and predicted force production for a high velocity ratio plunge maneuver: $w = 1c$, $h = 1c$, $\alpha = 0°$.

similar plunge maneuvers, wings of unequal size will produce the same normalized circulatory force (that is the purpose of the normalization), but different inertial forces.

Figures 4.13, 4.14, and 4.15 show examples of plunging wing force history predictions made by this model compared to the measured forces. As expected based on the discussion of $\mathbb{C}_1$ and $\mathbb{C}_2$ amplitudes, this model accurately represents forces produced by low-amplitude plunge maneuvers, but is increasingly incorrect as the velocity ratio increases. For the high-amplitude plunge maneuver in figure 4.13, the force production is mainly inertial, and the empirically tuned $\mathbb{C}_2$ term improves the model accuracy. Figure 4.14 shows results for a low-amplitude plunge maneuver. In this case (and all similar cases) the model matches the measured forces closely.

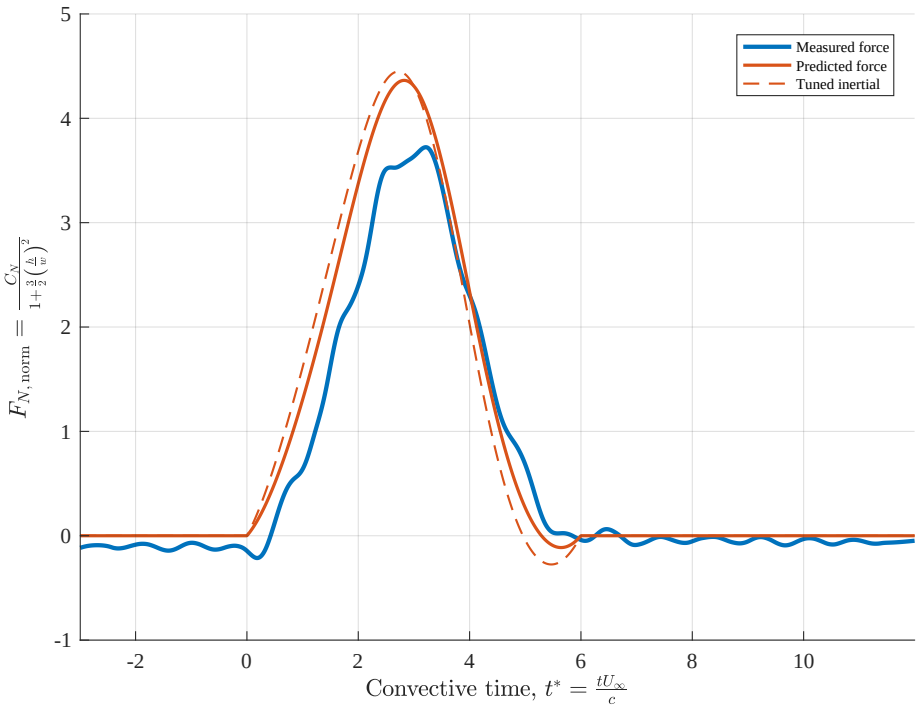

Figure 4.14: Comparison of measured and predicted force production for a low velocity ratio plunge maneuver: $w = 6c$, $h = 3c$, $\alpha = 0°$.

Both of these figures show results from cases for which $\alpha = 0°$. Figure 4.15 shows results from a high-amplitude plunge maneuver for which $\alpha = 20°$. The substantial unsteady force production dominates, so the steady-state influence of the wing pitch angle does not visibly affect the results. In this case, $\theta \approx 80°$ and so the model over-predicts the force production as expected based on figure 4.11.

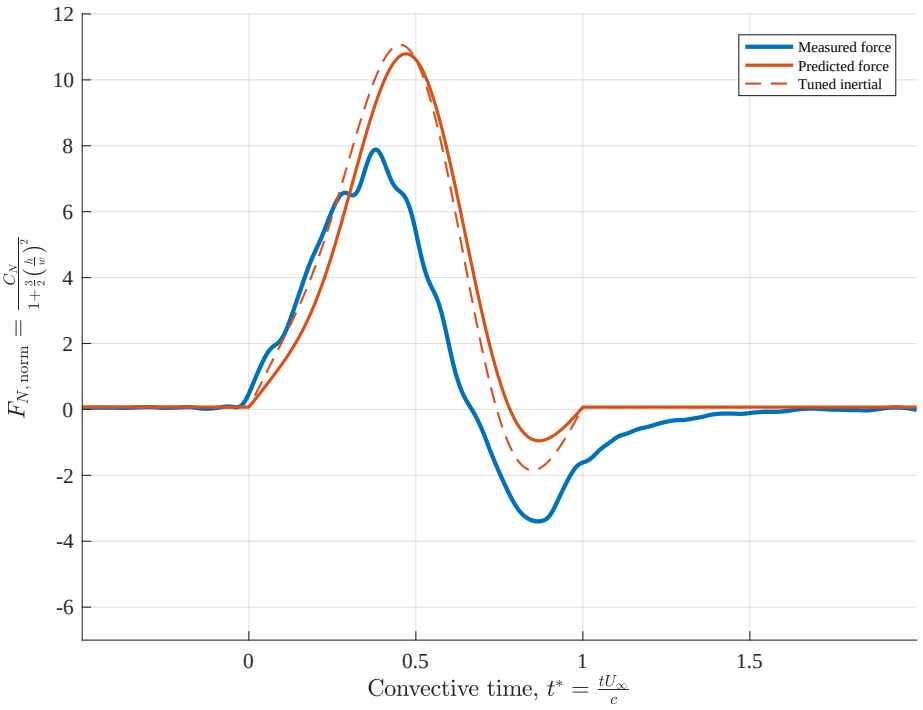

Figure 4.15: Comparison of measured and predicted force production for a high velocity ratio plunge maneuver with wing pitch angle: $w = 1c$, $h = 3c$, $\alpha = 20°$.

4.4 Comparison to gusts

It is also useful to compare the force production between the transverse gust encounters and the sine-squared plunge maneuvers, which are geometrically similar moving model and moving wing scenarios. In both cases, the steady flow is horizontal and the transient flow is vertical and has a sine-squared velocity profile.

The plunge maneuver kinematics are simpler to create and vary than is the generated fluid gust profile [46] (this is why even in the current work there are many more plunge cases than gust encounters — compare tables 2.1 and 2.2). Because of this, the investigation of gust encounter force production would be greatly simplified if

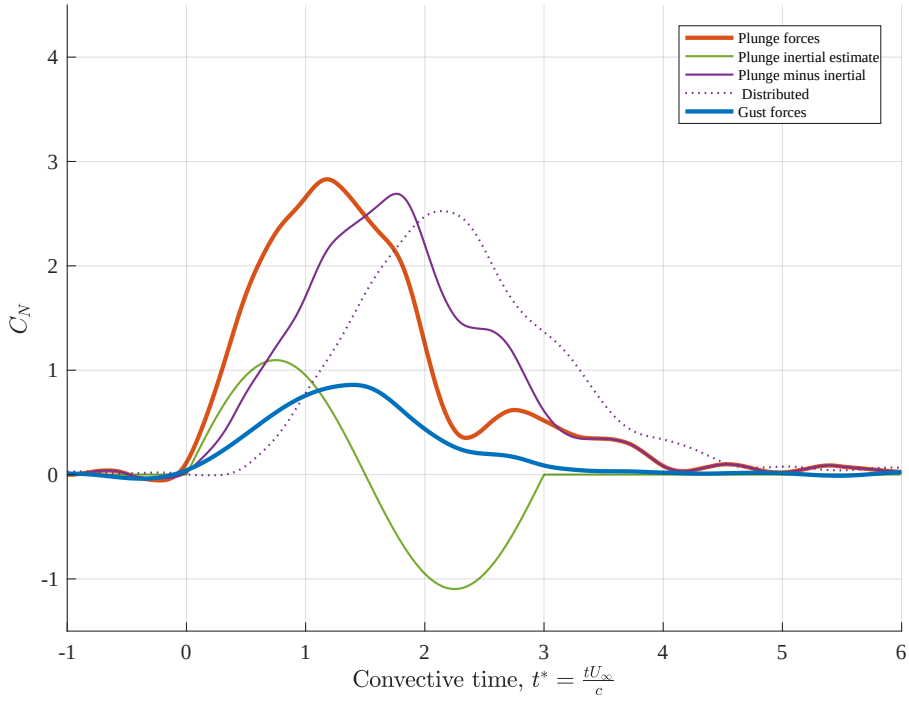

Figure 4.16: Comparison of normal force histories for a set of geometrically similar gust encounter and plunge maneuver at $\alpha = 0°$.

the results from plunging wings could be used to represent the gust encounter and so remove the need for a fluid gust generator. The current work includes measurements of both scenarios, and so is able to compare the force production in each and identify the inherent differences.

Figures 4.16 and 4.17 show force histories from gust encounters and plunge maneuvers as closely matched as was available in the data of the current work. The forces produced during the gust encounters are plotted in blue, and those from the plunge maneuvers are in red. The other lines are discussed in the following sections. In figure 4.16, the gust encounter and plunge maneuver both take place at $\alpha = 0°$, but the widths and velocity ratios are not exactly matched. The gust width is fixed at $w = 3.2c$, and in this case the velocity ratio was $G = \frac{V_g}{U_\infty} = 0.42$. The closest

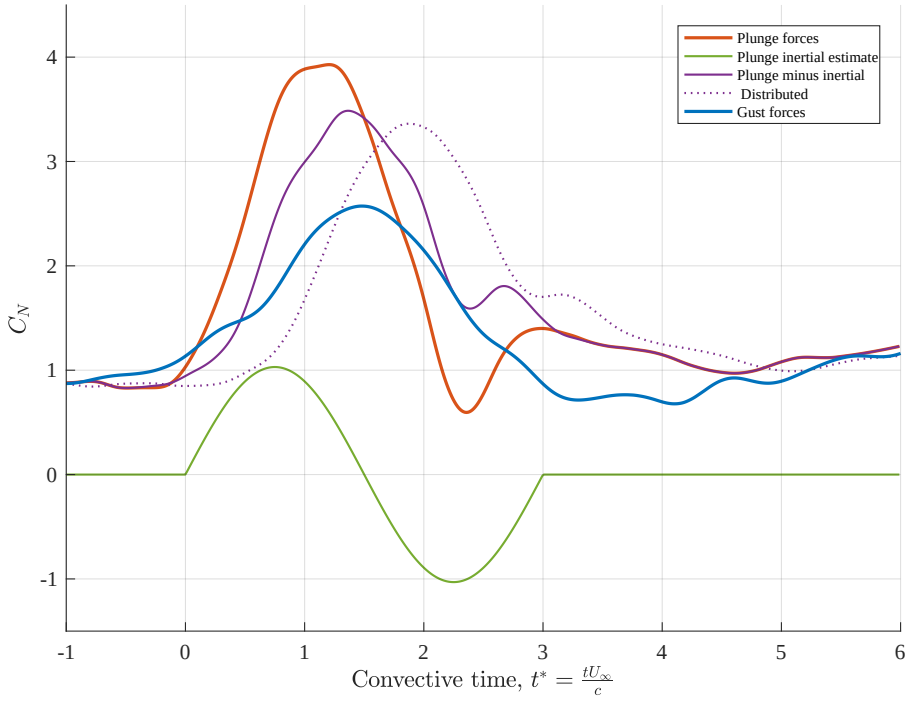

Figure 4.17: Comparison of normal force histories for a set of geometrically similar gust encounter and plunge maneuver at $\alpha = 20°$.

plunge maneuver had a width of $w = 3c$ and a velocity ratio of $\frac{V_p}{U_\infty} = 0.67$. In figure 4.17, the gust encounter and plunge maneuver both take place at $\alpha = 20°$, but the gust encounter was defined by $w = 3.2c$, $G = 0.84$, and the closest plunge maneuver was $w = 3c$, $\frac{V_p}{U_\infty} = 0.67$.

It is apparent and expected that the force production from similar-kinematics gust encounters and plunge maneuvers are not inherently the same. The differences between these cases must be quantified and counteracted in order to most closely match the force histories. In this work, no process is found which allows for the complete replacement of results from gust encounters by results from plunging wings, although the progress towards this goal is still worth discussing.

4.4.1 Inertial forces

The most obvious difference between moving model and moving fluid scenarios (for kinematics which include acceleration) is the presence or lack of inertial forces. In the gust encounters in the current work, the fluid is not accelerating — instead, the wing is passing through a region of varying fluid velocity. This does not induce any inertial force production. Alternately, the plunging wing experiences significant inertial forces during its acceleration. While the inertial response caused by the mass of the wing (and measurement hardware) was removed during post-processing, there is still an inertial force contribution from the surrounding fluid, the "added-mass" force.

Because this quantity is present in only the plunge maneuver cases, it can simply be subtracted from the plunge force histories. The magnitude of the added-mass force is given by equation 1.3, which reduces here to the right-most term of equation 4.16. This is plotted in figures 4.16 and 4.17 as the green line. The result of subtracting this from the total plunge force production is the "non-inertial" plunge force production, plotted in purple. This procedure has not caused the gust encounter and plunge maneuver forces to coincide, but it has caused the plunge maneuver force histories to be similar in shape to the gust encounter force histories, rising from steady state to peak over $t^* \approx 1.5$ and then descending to steady state without overshoot. As was also observed in the investigation of harmonic plunging by Wong et al. [46], the difference in forces produced by the moving model and moving fluid cases at the moment of zero acceleration indicates that inertial effects are not the

only difference between transverse gusts and plunge maneuvers.

4.4.2 Velocity distribution

The more complex difference between the gust encounters and the plunge maneuvers is the chord-wise distribution of the transient velocity. In the case of the plunge maneuvers, the kinematics vary in time, so the leading and trailing edges of the wing (and all points in between) experience simultaneous variations in transient velocity. This is not the same in the gust encounters. The gust profile is fixed in space, and the wing passes steadily through it. The leading edge of the wing reaches the gust first, and each point along the wing experiences different transient velocities than one another.

One effect of this is that the trailing edge of the wing does not exit the gust until $t^* = w + c\cos(\alpha)$, making the gust encounter last up to one chord-length longer than the width of the fluid gust. However, the forces observed for the gust encounters in the current work were most closely related to the conditions at the leading edge of the wing. Because of this, the gust encounters were compared to plunge maneuvers with widths of $w = 3c$ rather than $w = 4c$.

Additionally, there is no moment during the gust encounter during which the entire wing experiences the peak gust velocity. This means that the chord-averaged peak dynamic pressure is lower in the gust encounter than in a plunge maneuver with the same characteristic velocity. This can be compensated for by effectively distributing the plunge maneuver velocity profile in the same way that the gust

velocity is distributed. The velocity itself can not be physically distributed in the experiment; instead, the force production resulting from that velocity can be distributed in the analysis.

At any moment during the gust encounter, each chord-wise location on the wing experiences a different nominal gust velocity. During the plunge maneuver, however, each location experiences the same simultaneous plunge velocity. The effects of the plunge can be distributed over the velocity profile of the gust by treating each chord-wise location on the wing as producing the plunge forces from the moment during which the wing was plunging at the appropriate velocity. For example, at $t^* = 0.5$ the trailing half of the wing has not entered the gust, and so in the plunge case no force contribution is considered there, even though at $t^* = 0.5$ the entire wing was plunging. The force production on each chord-wise point of the plunging wing is taken from the plunge force history at the moment that matches the gust velocity at that time and chord-wise location.

The distributed force production at any point is the average over the preceding chord-length of the un-distributed force production (accounting for the horizontal projection of the chord, the average is taken over $t^* = \cos(\alpha)$). This procedure incorporates both the effective delay in the transient event for the trailing edge compared to the leading edge and the reduced peak chord-averaged transient velocity. The result of this is plotted as the dashed purple line in figures 4.16 and 4.17. In these cases, this distribution of the plunge maneuver force production does not make it conclusively closer or further from the gust encounter force production. The effects of the velocity distribution — and thus the ability to test this procedure — would

be increased for a narrower gust encounter (or larger wing), but that is not available to the current study.

4.5 Chapter summary

In this chapter, force measurements from sine-squared profile plunge maneuvers were displayed and analyzed. The force histories were shown to be dominated by plate-normal forces, to vary significantly in shape depending on the plunge kinematics, and to recover to steady state force production almost immediately after the plunge maneuver ended.

Variations in force production were then inspected with respect to one independent parameter at a time. The freestream velocity had little effect on the normalized force histories, which indicates that the force production is insensitive to Reynolds number within the tested range. The wing pitch angle also had little effect on the transient force production, which was unexpected and remains unexplained. The plunge maneuver width and height both changed the force histories, because they each changed the ratio of steady and transient velocities. The measured data was reduced to characteristic scalars by curve fitting based on the instantaneous acceleration and dynamic pressure of the maneuver. The reduced data helped to identify that forces predicted by thin-airfoil theory and potential flow added-mass matched the measured force production closely for roughly half of the tested cases. The other half of the tested cases, which had higher velocity ratios, were over-predicted by thin-airfoil theory and under-predicted by added-mass, which likely

indicates that unmodeled unsteady force production becomes more significant in those cases. The resulting force production model was presented (equation 4.16) and the predicted and measured force histories were compared for several example kinematics.

Force production was then compared between the plunge maneuvers and the gust encounters. Two important differences, inertial forces and spatial velocity distribution, were discussed and methods of counteracting those differences were tested. For the available data, the described treatment of force histories was not adequate to collapse results between moving model and moving fluid force production.

Chapter 5: Summary and conclusions

An experimental investigation of unsteady force production by stream-normal phenomena was conducted in order to extend present unsteady force models to these two-dimensional, large-perturbation conditions. Consideration was given to small-perturbation analyses of two-dimensional events including Wagner [10], Küssner [12], and von Kármán and Sears [18], and to large-perturbation analysis of quasi-one-dimensional events such as Granlund et al. [33] and Babinsky et al. [26]. The current work adapted the existing small-perturbation models to large-velocity-ratio transverse gust encounters and plunge maneuvers by the physical interpretation of correlations between the defined kinematic parameters and the observed force production.

Unsteady force production was measured for a flat plate wing during many variations of transverse gust encounters and plunge maneuvers in the University of Maryland automated motion-controlled towing tank. The velocity profile in each case was limited to the sine-squared shape, but parameters such as the wing pitch angle, wing towing velocity, gust velocity ratio, plunge maneuver height, and plunge maneuver width were varied. Flow velocities around the wing were measured for several gust encounters to aid in identifying the sources of unsteady force fluctuations.

Force histories which were measured during gust encounters were characterized by peak normal force in each case. The magnitudes of these peaks within the current parameter space were found to be reasonably approximated by quasi-steady analysis, but the variations in peak force with respect to wing pitch angle suggested non-negligible unsteady effects (as did the duration of the gust recovery process). The flow velocity measurements made by PIV identified large leading and trailing edge vortices as a likely mechanism for the unsteady influence on force production.

Force histories which were measured during the plunge maneuvers were compared by decomposing the force production into two sinusoidal terms which corresponded to the quasi-steady terms of the model by von Kármán and Sears. The residual of this model was found to be low in all cases, which indicated that unsteady force production during the tested plunge maneuvers was accurately represented by quasi-steady analysis. The unsteady influence on force histories instead augmented each of the quasi-steady terms, which were found to be under-predicted by typical analytical models.

5.1 Key gust encounter conclusions

The transverse gust encounters in the current work were shown to produce one primary peak in force production during the gust encounter and diminishing oscillations in force production after the gust encounter. The gradual return of forces to the steady-state levels occurred over roughly $30c$ — an order of magnitude greater than the duration of the gust encounter.

The initial minimum in these oscillations, which occurs just as the trailing edge of the wing exits the gust, causes the force production to temporarily dip below the steady-state force production of the towed wing. The force oscillations during gust recovery were connected to the presence of large vortices in the wake of the wing. Concentrations of negative vorticity from the leading edge vortices caused force augmentation, while concentrations of positive vorticity from trailing edge vortices caused force reduction.

The magnitude of the peak force production in most of the studied gust encounters was found to match in magnitude to predictions made by quasi-steady empirical analysis. The trend in peak force production with respect to wing pitch angle was more accurately recreated by indicial convolution of Küssner's function and non-linear thin airfoil theory, but that model poorly recreated the trend in peak force production with respect to gust velocity ratio. This close agreement suggests that Küssner's function and non-linear thin airfoil theory adequately represent the transient force production during these transverse gust encounters but that the current implementation misses a variation in magnitude which scales with gust ratio — perhaps unidentified in the current work due to the lack of tested variations in gust width.

5.2 Key plunge maneuver conclusions

Force production by the sine-squared profile plunge maneuvers in the current work was shown to vary with respect to the plunge maneuver width and height, but

not with respect to freestream Reynolds number and only slightly with respect to wing pitch angle. Wing pitch angle does significantly affect the steady-state force production, but the unsteady force production dominates in most of the tested cases. The observed invariance in transient force production with respect to wing pitch angle goes against available analytical models and remains unexplained. Although the unsteady force production was significant during the maneuver, the forces returned to steady-state levels nearly immediately after the maneuver ended.

A physically-based, quasi-steady model was formulated which matched to the measured force histories for many of the conditions tested in the current work. The model combined a semi-empirical steady-state term, the potential flow solution for added-mass, and quasi-steady thin-airfoil theory. The model did not match as closely to force histories from plunge maneuvers with very high velocity ratios. Some of those cases were able to be corrected by an empirical tuning of the inertial force production estimate.

Fundamental differences between transverse gust encounters and plunge maneuvers were unable to be counteracted in a way which could allow the translation of results from one case to the other. Force production by the gust encounters was significantly lower than that of geometrically-similar plunge maneuvers. This difference was not adequately accounted for by inertial force production or spatial velocity distributions.

5.3 Highlighted original contributions

In the current work, it was demonstrated that a large-perturbation adaptation to indicial theory using non-linear thin-airfoil theory and Küssner's function was able to closely match the trends in peak force production by transverse gust encounters for variations in wing pitch angle. This improved on the predicted trends of both quasi-steady analysis and the typical application of indicial theory using linearized thin airfoil theory, although those two models each captured the trends with respect to gust velocity ratio better than the proposed model. This model extends the preceding work in small-perturbation transverse gusts and large-perturbation longitudinal gusts to the current subject of large-amplitude transverse gusts.

It was also demonstrated that the quasi-steady components of the model by von Kármán and Sears can account for most of the force production during sine-squared profile plunge maneuvers. The missing term, which accounts for wake vorticity, may explain the under-prediction of semi-empirical methods. This agrees with the gust encounter results of the current work and with preceding work in surge maneuvers, in which the effect of the leading edge vortex was to augment the force production so that it approached that of attached flow even at high incidence angles [26].

5.4 Suggestions for future work

The experimental data in the current work and the models developed based on that data have several limitations which can be addressed in future research.

Hardware limitations meant that the fluid gust velocity was not variable during these tests; the gust velocity ratio was changed by varying the towing velocity of the wing. It was expected based on previous work that the tested variations in freestream Reynolds number did not have significant independent effects on the force coefficient histories, but verification of that assumption is only possible using a gust generator which has variable speed control.

Additionally, the chord-normalized gust width was not varied in the current work. This could be varied in future work by a controllable-width gust generator or, perhaps more easily, by repeating tests in a fixed-width gust using a smaller or larger wing. This would be particularly helpful in the further development of indicial models, which integrate the force production over the flow history and so are significantly changed by the duration (in convective time) of the transient gust velocity. The investigation of this effect could help to reconcile the otherwise-successful predictions of the proposed adaptation to indicial theory with the observed trends in peak force production with respect to gust ratio.

The lack of variation in plunge maneuver force production with respect to wing pitch angle remains unexplained. The wing pitch angle affects the steady-state force production and alters the orientation of the plate-normal force, but it had little effect on the magnitude of the transient plate-normal force. For most of the cases tested in the current work, the transient forces were far greater than the steady-state forces, so the wing pitch angle appeared to have little overall effect on the force production during the plunge maneuvers. Neither thin-airfoil theory nor the empirical look-up method agree with the observed result that the variation in normal force production

with respect to the plunge-velocity-induced flow incidence angle, $\frac{dC_N}{d\theta}$, is unaffected by the initial pitch angle, α. Further investigation of the effect of wing pitch angle on plunge maneuver force production is needed to identify the mechanisms behind the observations of the current work.

During the decomposition of plunge maneuver force production, the model fit residual was low for all cases despite the conflicting nature of applying a quasi-steady model to highly unsteady force production. The effects of the unsteady wake vorticity term of the model by von Kármán and Sears were thought to be contained in the quasi-steady model terms, rather than being truly absent as the low residual might suggest. This was helpful in the development of a physically-based quasi-steady model for plunging wing force production, but limits that result to sine-squared profile plunge maneuvers. Further analysis of von Kármán and Sears for large-perturbation plunge maneuvers could separate the unsteady and quasi-steady effects by testing maneuvers with non-sinusoidal velocity profiles, for which the quasi-steady and unsteady force production components would have more notably different shapes. This would significantly increase the parameter space and complicate the decomposition method of analysis but could eventually allow for a more generalized model for unsteady force production during plunge maneuvers with separated flow.

The vortex dynamics of a surging flat plate were simplified by Babinsky et al. so that their unsteady effects could be expressed in a quasi-steady model [24–26]. The constant longitudinal acceleration of that maneuver greatly simplified the vortex trajectories compared to what could be expected for the plunging wing maneuvers of the current work. The two-dimensional relative motion of the wing and the

shed vortices in the plunging case would require a more elaborate characterization than the one-dimensional motion of the surging wing. Despite this difficulty, PIV measurements of vortex growth and trajectories during plunging maneuvers could provide an alternate formulation for a quasi-steady model of plunging wing force production. A similar approach could be applied to transverse gusts, although the vortex trajectories may be even further complicated due to the leading edge vortices being temporarily "shielded" from the gust by the wing. Even if vortex tracking does not lead to quasi-steady models for force production in these cases, increased knowledge of the vortex behavior for various transverse gusts and plunging maneuvers may help to justify the observed forces in the current work.

Bibliography

[1] Hoblit, F. M. *Gust Loads on Aircraft: concepts and applications*. AIAA, 1988.

[2] Leishman, J. G. *Principles of Helicopter Aerodynamics*. Cambridge University Press, 2 edition, 2006.

[3] Shyy, W., Aono, H., Chimakurthi, S., Trizila, P., Kang, C.-K., Cesnik, C., and Liu, H. Recent progress in flapping wing aerodynamics and aeroelasticity. *Progress in Aerospace Sciences*, 46:284–327, 2010.

[4] Ansari, S. A., Zbikowski, R., and Knowles, K. Aerodynamic modelling of insect-like flapping flight for micro air vehicles. *Progress in Aerospace Sciences*, 42:129–172, 2006.

[5] Platzer, M. F., Jones, K. D., Young, J., and Lai, J. C. S. Flapping-wing aerodynamics: Progress and challenges. *AIAA Journal*, 46:2136–2149, 2008.

[6] AVT-149. Unsteady aerodynamics for micro air vehicles. Technical report, NATO Research and Technology Organization, 2010.

[7] Anderson, J. D. *Fundamentals of Aerodynamics*. McGraw-Hill, fifth edition, 2011. pp. 430-444.

[8] Blisplinghoff, R. L., Ashley, H., and Halfman, R. L. *Aeroelasticity*. Dover Publications, 1996.

[9] Brennen, C. E. A review of added mass and fluid inertial forces. Technical report, Naval Civil Engineering Laboratory, 1982.

[10] Wagner, H. A. *Über die Entstehung des dynamischen Auftriebes von Tragflügeln (On the origin of the dynamic lift of wings)*. PhD thesis, Zeitschrift für angewandte Mathematik und Mechanik, 1925.

[11] Jones, R. T. The unsteady lift of a finite wing. Technical report, National Advisory Committee for Aeronautics, 1939.

[12] Küssner, H. Zusammenfassender bericht über den instationären auftrieb von flügeln (summary report on the instationary lift of wings). *Luftfahrtforschung*, 13:410–424, 1936.

[13] Miles, J. W. The aerodynamic force on an airfoil in a moving gust. *Journal of the Aeronautical Sciences*, 23:1044–1050, 1955.

[14] Theodorsen, T. General theory of aerodynamic instability and the mechansim of flutter. Technical report, NACA Report 496, 1935.

[15] Garrick, I. E. Propulsion of a flapping and oscillating airfoil. Technical report, National Advisory Committee for Aeronautics, 1936.

[16] Isaacs, R. Airfoil theory for flows of variable velocity. *Journal of the Aeronautical Sciences*, 1944.

[17] Greenberg, J. M. Airfoil in sinusoidal motion in a pulsating stream. Technical report, National Advisory Committee for Aeronautics, 1947.

[18] von Kármán, T. and Sears, W. R. Airfoil theory for non-uniform motion. *Journal of the Aeronautical Sciences*, 5:379–390, 1938.

[19] Ansari, S. A., Zbikowski, R., and Knowles, K. Non-linear unsteady aerodynamic model for insect-like flapping wings in the hover. part 1: methodology and analysis. *Proceedings of the Institution of Mechanical Engineers, Part G: Journal of Aerospace Engineering*, 2006.

[20] Ansari, S. A., Zbikowski, R., and Knowles, K. Non-linear unsteady aerodynamic model for insect-like flapping wings in the hover. part 2: implementation and validation. *Proceedings of the Institution of Mechanical Engineers, Part G: Journal of Aerospace Engineering*, 2006.

[21] Eldredge, J. D. and Darakananda, D. Reduced-order two- and three-dimensional vortex modeling of unsteady separated flows. *53rd AIAA Aerospace Sciences Meeting*, 2015.

[22] Darakananda, D., Eldredge, J. D., Colonius, T., and Williams, D. R. A vortex sheet/point vortex dynamical model for unsteady separated flows. *54th AIAA Aerospace Sciences Meeting*, 2016.

[23] Leishman, J. G. Subsonic unsteady aerodynamics caused by gusts using the indicial method. *Journal of Aircraft*, 1996.

[24] AVT-202. Extensions of fundamental flow physics to practical MAV aerodynamics. Technical report, NATO Research and Technology Organization, 2016.

[25] Stevens, P. R. R. J., Babinsky, H., Manar, F., Mancini, P., Jones, A. R., Granlund, K. O., Ol, M. V., Nakata, T., Phillips, N., Bomphrey, R. J., and Gozukara, A. C. Low Reynolds number acceleration of flat plate wings at high incidence. *54th AIAA Aerospace Sciences Meeting*, 2016.

[26] Babinsky, H., Stevens, P. R. R., Jones, A. R., Bernal, L. P., and Ol, M. V. Low order modelling of lift forces for unsteady pitching and surging wings. *54th AIAA Aerospace Sciences Meeting*, 2016.

[27] Ol, M. V. and Babinsky, H. Unsteady flat plates: a cursory review of AVT-202 research. *54th AIAA Aerospace Sciences Meeting*, 2016.

[28] Pitt Ford, C. W. and Babinsky, H. Lift and the leading-edge vortex. *Journal of Fluid Mechanics*, 720:280–313, 2013.

[29] Dickinson, M. H. and Götz, K. G. Unsteady aerodynamic performance of model wings at low Reynolds numbers. *Journal of Experimental Biology*, 1993.

[30] Mancini, P., Manar, F., Granlund, K., Ol, M. V., and Jones, A. R. Unsteady aerodynamic characteristics of a translating rigid wing at low Reynolds number. *Physics of Fluids*, 2015.

[31] Gursul, I. and Ho, C.-M. High aerodynamic loads on an airfoil submerged in an unsteady stream. *AIAA Journal*, 1992.

[32] Greenblatt, D. Unsteady low-speed wind tunnels. *AIAA Journal*, 54:1817–1830, 2016.

[33] Granlund, K., Monnier, B., Ol, M., and Williams, D. Airfoil longitudinal gust response in separated vs. attached flows. *Physics of Fluids*, 2014.

[34] Rival, D. and Tropea, C. Characteristics of pitching and plunging airfoils under dynamic-stall conditions. *Journal of Aircraft*, 2010.

[35] Sunada, S., Kawachi, K., Matsumoto, A., and Sakaguchi, A. Unsteady forces on a two-dimensional wing in plunging and pitching motions. *AIAA Journal*, 2001.

[36] Ol, M. V., Bernal, L., Kang, C.-K., and Shyy, W. Shallow and deep dynamic stall for flapping low Reynolds number airfoils. *Experiments in Fluids*, 2009.

[37] McGowan, G. Z., Granlund, K., Ol, M. V., Gopalarathnam, A., and Edwards, J. R. Investigations of lift-based pitch-plunge equivalence for airfoils at low Reynolds numbers. *AIAA Journal*, 2011.

[38] Baik, Y. S., Bernal, L. P., Granlund, K., and Ol, M. V. Unsteady force generation and vortex dynamics of pitching and plunging aerofoils. *Journal of Fluid Mechanics*, 2012.

[39] Baik, Y. S. and Bernal, L. P. Experimental study of pitching and plunging airfoils at low Reynolds numbers. *Experiments in Fluids*, 2012.

[40] Panah, A. E., Akkala, J. M., and Buchholz, J. H. J. Vorticity transport and the leading-edge vortex of a plunging airfoil. *Experiments in Fluids*, 2015.

[41] Choi, J., Colonius, T., and Williams, D. R. Surging and plunging oscillations of an airfoil at low Reynolds number. *Journal of Fluid Mechanics*, 2015.

[42] Kriegseis, J., Kinzel, M., and Rival, D. E. On the persistence of memory: do initial conditions impact vortex formation? *Journal of Fluid Mechanics*, 2013.

[43] Kuethe, A. M. Circulation measurements about the tip of an airfoil during flight through a gust. Technical report, National Advisory Committee for Aeronautics, 1939.

[44] Sears, W. R. and Kuethe, A. M. The growth of the circulation of an airfoil flying through a gust. *Journal of the Aeronautical Sciences*, 6:376–378, 1939.

[45] Holmes, D. W. Lift measurements in an aerofoil in unsteady flow. In *The American Society of Mechanical Engineers' Gas Turbine Conference and Products Show*, 1973.

[46] Wong, J. G., Mohebbian, A., Kriegseis, J., and Rival, D. E. Rapid flow separation for transient inflow conditions versus accelerating bodies: An investigation into their equivalency. *Journal of Fluids and Structures*, 2013.

[47] Ortiz, X., Rival, D., and Wood, D. Forces and moments on flat plates of small aspect ratio with application to PV wind loads and small wind turbine blades. *Energies*, 2015.

[48] Burgers, P. and Alexander, D. E. Normalized lift: An energy interpretation of the lift coefficient simplifies comparisons of the lifting ability of rotating and flapping surfaces. *PLoS One*, 7, 2012.